Developing Tools to Study Carbohydrate Processing Enzymes in AmpC β-Lactamase Antibiotic Resistance and OGA-Based Neurodegenerative Research

by

Viktor Holicek

B.B.A, Simon Fraser University, 2016

Thesis Submitted in Partial Fulfillment of the
Requirements for the Degree of
Master of Science

in the
Department of Chemistry
Faculty of Science

SIMON FRASER UNIVERSITY
Fall 2020

Declaration of Committee

Name:	**Viktor Holicek**
Degree:	**Master of Science**
Title:	**Developing Tools to Study Carbohydrate Processing Enzymes in AmpC β-Lactamase Antibiotic Resistance and OGA Based Neurodegenerative Research**
Committee:	**Chair: Corina Andreoiu** Associate Professor, Chemistry
	David Vocadlo Supervisor Professor, Chemistry
	Robert Young Committee Member Professor, Chemistry
	Neil Branda Committee Member Professor, Chemistry
	Andrew Bennet Examiner Professor, Chemistry

Abstract

Carbohydrates are one of the four main classes of biological macromolecules in nature, alongside lipids, proteins, and nucleic acids. They serve in a wide range of cellular functions fundamental to the existence of biological organisms. These functions include but are not limited to cellular metabolism, energy production and storage, structural support, signaling, and recognition. The ubiquitous presence of carbohydrates in organisms has led to the study of their role in various maladies, such as neurodegenerative and infectious diseases. Deciphering the role of carbohydrates in these diseases allows for the possibility of developing treatments for associated diseases. In this manner, it is necessary to develop tools to exploit and test our understanding of these mechanisms. Existing methodologies may need to be adapted for application to larger scale experimental designs, such as those used in chronic dosing studies using preclinical animal models or high-throughput automated screening assays. This thesis describes improvements to previously published methods in the synthesis of one such chemical tool, Thiamet-G, a small molecule inhibitor used to study the carbohydrate processing enzyme O-GlcNAcase, which has been linked to neurodegenerative diseases including Alzheimer's and Parkinson's Disease. This thesis also seeks to apply the concepts developed during creation of a live cell assay towards creation of a new experimental approach suitable for large scale high through-put screening of compound libraries. Such an application would allow for the efficient pursuit of inhibitors of the bacterial protein AmpG - a transporter that is essential for inducible AmpC β-lactamase-driven antibiotic resistance.

Keywords: Gram-negative bacteria; β-lactam antibiotics resistance; disaccharide substrate; membrane permease; transporter enzyme ampG; live-cell assay; caged fluorescence; coupled assay; high-throughput scale; Thiamet-G; O-GlcNAcase.

Scientific progress is driven as much by the questions posed as by the tools available to answer them" - Gary Taubes

Table of Contents

List of Tables

List of Figures

List of Schemes

List of Acronyms

$(Bu_3Sn)_2O$	Bis[tri-n-butyltin(IV)]oxide
[X]	concentration of substance X
°C	degrees Celsius
Å	angstrom
ABP	activity-based probe
Ac_2O	acetic anhydride
AF350	Alexa Fluor 350
AgOTf	silver triflate
AMC	Aminomethylcoumarin
AmpC	an inducible β-lactamase found in clinically relevant Gram-negative bacteria
AmpG	a bacterial inner membrane permease responsible for transporting GlcNAc-anhMurNAc from the periplasm to the cytoplasm for recycling
ATP	adenosine triphosphate
BnBr	benzyl bromide
Boc_2O	di-tert-butyl dicarbonate
BODIPY	boron dipyrromethene
CAZy	carbohydrate active enzyme
CD3OD	deuterated methanol
$CDCl_3$	deuterated chloroform
CH_3COOH	acetic acid
DCM	dichloromethane
dd	doublet of doublets
ddd	doublet of doublets of doublets
ddt	doublet of doublets of triplets
DIPEA	diisopropylethylamine
DMF	dimethylformamide
DMSO	dimethyl sulfoxide
DMSO-d6	deuterated dimethyl sulfoxide
DNA	deoxyribonucleic acid
dt	doublet of triplets
E. coli	Escherichia coli

EcBW	wild-type E. coli strain BW25113
EcMG	wild-type E. coli strain MG1655
EDTA	ethylenediaminetetraacetic acid
ER	endoplasmic reticulum
ES	enzyme-substrate complex
Et_2O	diethyl ether
EtOAc	ethyl acetate
EtOH	ethanol
FRET	Förster resonance energy transfer
g	grams
GH	glycoside hydrolase
Glc	glucose
GlcNAc	N-acetylglucosamine
GlcNAc-anhMurNAc	a peptidoglycan fragment that is a precursor to inducers of AmpC β-lactamase
H_2	hydrogen
H_2O	water
H_2SO_4	sulfuric acid
HBr	hydrogen bromide
HBTU	N,N,N′,N′-tetramethyl-O-(1H-benzotriazol-1-yl)uronium hexafluorophosphate
HCl	hydrogen chloride
HPLC	high performance liquid chromatography
hr	hours
HRMS	high resolution mass spectrometry
HTS	high-throughput screening
I_2	iodine
K_2CO_3	potassium carbonate
$KMnO_4$	potassium permanganate
LiOH	lithium hydroxide
LRMS	low resolution mass spectrometry
M	molar
m	multiplet
MeCN	acetonitrile
MeOH	methanol

mg	milligram
MG1655	a wild-type E. coli strain
$MgCl_2$	magnesium chloride
min	minutes
mL	millilitre
mm	millimeter
mM	millimolar
mmol	millimol
MS	mass spectrometry OR molecular sieves
MurNAc	N-acetylmuramic acid
N_2H_4	hydrazine
Na_2SO_4	sodium sulfate
NaH	sodium hydride
$NaHCO_3$	sodium bicarbonate
NaN_3	sodium azide
NaOH	sodium hydroxide
NaOMe	sodium methoxide
NBD-Glc	2-(*N*-(7-nitrobenz-2-oxa-1,3-diazol-4-yl)amino)-2-deoxyglucose
NFT	Neurofibrillary tangles
nm	nanometer
NMR	nuclear magnetic resonance
O2	oxygen
OD600	optical density at 600nm
OGA	*O*-GlcNAcase
OGT	*O*-GlcNAc transferase
P	product
P. aeruginosa	*Pseudomonas aeruginosa*
pBAD	a promotor
PBS	phosphate buffered saline
PBP	Penicillin binding proteins
Pd/C	activated palladium on charcoal
PG	peptidoglycan
pH	negative logarithm of the proton concentration

pKa	negative logarithm of the acid dissociation constant
q	quartet
rcf	relative centrifugal force
Rf	retention factor
RFU	relative fluorescence units
RT	room temperature
s	singlet
t	triplet
TEA	trimethylamine
TFA	trifluoroacetic acid
THF	tetrahydrofuran
TLC	thin layer chromatography
UV	ultraviolet
UV-vis	ultraviolet-visible

Chapter 1.

A Select Overview of Carbohydrates, Carbohydrate Processing Enzymes, and Tools Used to Increase our Understanding of These Topics

1.1. Carbohydrates and their Biological Role as a Class of Macromolecules

1.1.1. A Selective Overview of Carbohydrates (1.1.1)

Carbohydrates are one of the four main biological macromolecules found alongside proteins, nucleic acids, and lipids within nature. Etymologically, carbohydrates were named based on their elemental constituents, carbon, hydrogen, and oxygen. These constituents often exist in a hydrogen-oxygen atom ratio of 2:1, thus yielding the general formula for most carbohydrates of $C_m(H_2O)_n$, and accordingly leading to these compounds being sometimes referred to as the hydrate of carbon.

Accepted definitions for carbohydrates have varied over time and between industries – formaldehyde (CH_2O) for example, while meeting the $C_m(H_2O)_n$ formula is nonetheless not typically recognized as a carbohydrate. Acetic acid, which also meets the $C_m(H_2O)_n$ formula, also is generally not recognized as a carbohydrate outside of the USDA National Nutrient Database. In the realm of chemical biology and for the purposes of this thesis, carbohydrates are recognized and limited to those molecules having a minimum of three carbon atoms, each of which is covalently bound to oxygen functional groups existing as a polyhydroxyl aldehyde or ketone or polymer thereof. In addition to this basic core structure, carbohydrates can exist with a multitude of modifications. This includes the addition of acetyl bearing nitrogen groups as seen in amino sugars such as those relevant to this thesis - chiefly *N*-acetyl-*D*-glucosamine and or alkylated analogues such as *N*-acetyl-*D*-muramic acid (Figure 1.1).

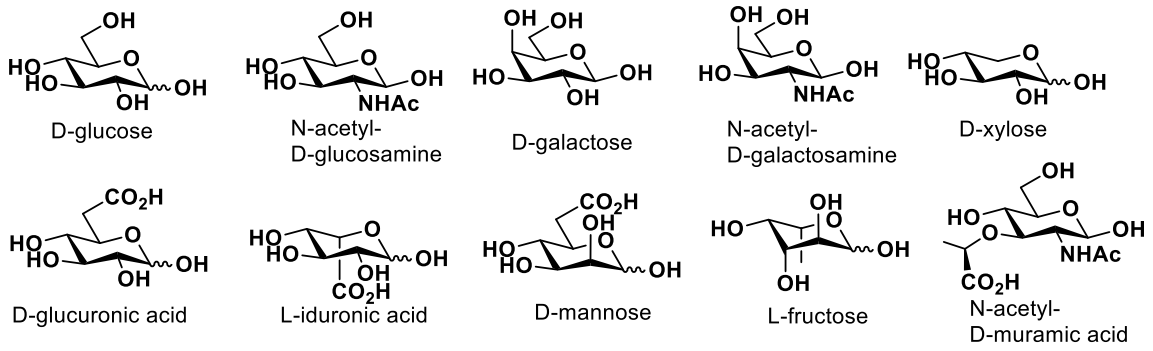

Figure 1.1. A Selected Assortment of Chair Conformation Carbohydrate Structures
Variation in the substituents and conformation of carbohydrates is readily illustrated using three dimensional representations of these molecules.

Carbohydrates first gained attention in the nineteenth century, with the discovery of their role in the human metabolic process for deriving energy from the oxidation of food by German scientist Justus von Liebig. Further probing into the nature of carbohydrates yielded the discovery of glycogen as a starchy substance in mammalian livers by French chemist Claude Bernard in 1856[1]. This observation not only shed insight into the energy storage capabilities of carbohydrates, but also into the nature of their structure as polymers of glucose and the ability for them to break down into individual monosaccharide units. Further elucidation of the variations and specific stereochemical structure of carbohydrates was carried out by the great German chemist Emil Fischer, who with his team in in 1891 deduced the 16 stereoisomeric structures of glucose[2] as well as providing Fischer Projection diagrams as a way of visually representing differences in these aldohexose isomers - a representation that still is used to this day (Figure 1.2).

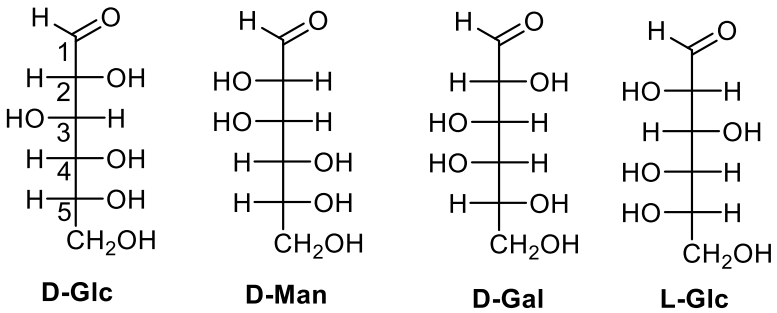

Figure 1.2. Carbohydrates as Depicted by Fischer Projections
Fischer Projections were devised by German chemist Emil Fischer following his discovery of their various stereochemical conformations. They allow enantiomers to be easily distinguished from one another by observing the configuration of the chiral carbon furthest away from the carbonyl group (position 5 in D-Glc depicted

above). D or (+) denoted carbohydrates will have a hydroxyl substituent positioned on the right side of the carbon backbone, whereas L or (-) will have a hydroxyl position on the left side of the carbon backbone.

In their polymer form, carbohydrates are composed of individual saccharide monomers, called monosaccharides, that is analogous to the linkages between amino acids or nucleic acids that together comprise proteins and DNA, respectively. Given the multitude of positions and stereochemical orientations in which carbohydrates can be configured and be linked to one another, many more degrees of freedom and structural complexity are available to carbohydrate polymers as compared to protein and DNA.

As a source of molecular fuel, the carbohydrate glucose plays a critical role in cellular respiration and the production of ATP necessary for cellular function and survival[3-4]. At the monomeric level inside cells, glucose exists primarily in the monophosphorylated form as glucose 6-phosphate, from which it may enter several metabolic pathways including the glycolysis and pentose phosphate pathways[5,6]. These same glucose monosaccharides in their β1-4 glycosidic linked polymeric form, known as cellulose, also provide the structural support in plant cell walls[7,8]. In addition to energy production and structural integrity, carbohydrates serve a multitude of signaling and recognition functions. One specific area with far reaching implications in healthcare stems from the glycan system underlying blood type antigens. Each antigen corresponds to a specific glycan expressed at the cell surface, which dictates immune system response to foreign blood and tissues that may be transplanted[9,10]. The enzymatic and covalent addition of carbohydrates to proteins inside the cell, known as glycosylation, a form of post-translational modification (PTM), can significantly influence proteins in terms of their folding, their available conformations, overall stability, and regulatory functions[11,12]. Glycosylation is found as one of four major categories: N-linked glycosylation, O-linked glycosylation, C-linked mannosylation, and glypiation[13,14]. Of these four modifications, N-linked and O-linked (denoting the amino acid residue to which the carbohydrate is covalently bound) are the most prevalent[14,15].

1.1.2. Carbohydrate processing enzymes

Post-translational glycosylation of proteins inside cells is carried out by carbohydrate processing enzymes. These enzymes are responsible for catalyzing the addition, removal, or modification of carbohydrates – resulting in the wide range of

glycans and glycoconjugates found within cells – together comprising the entire glycome[16]. The Carbohydrate Active Enzymes database (CAZy) provides a means of classifying carbohydrate processing enzymes based on their amino acid sequence. The majority of these carbohydrate processing enzymes exist either to add (glycosyl transferases) or remove (glycosyl hydrolase) carbohydrates from their corresponding protein substrate.

Within the CAZy system, glycoside hydrolases (GHs) are the most common and well characterized carbohydrate processing enzymes. This class of enzymes catalyzes the breakdown of the large polysaccharide biomasses of starch during the consumption of food by large organisms including humans. At the cellular level, other GHs cleave the beta-1,4 linkages of the peptidoglycan of both Gram-negative and Gram-positive bacteria to recycle and maintain the bacterial cell wall[17,18]. In contrast to the hydrolase and transferase category of carbohydrate processing enzymes there also exist carbohydrate transporters – enzymes responsible for the transport of sugars through membranes. The bacterial protein AmpG is one such enzyme, which as a transporter also plays a fundamental role in the recycling and maintenance of the Gram-negative bacterial cell well. Its exclusive capacity for cytoplasmic uptake of GlcNAc-anhMurNAc-peptides will be a fundamental point of importance in the development of this thesis in subsequent chapters[19–21].

1.1.3. Glycoside Hydrolase Mechanisms

Exo- and *endo*-glycoside hydrolases refer to the region of a polysaccharide where the enzyme is capable of cleaving. Enzymes specific to glycosidic linkages at the terminal end of a polymer (*exo*-acting) will typically share an enzymatic structure distinct from that of the hydrolases capable of cleaving glycosidic linkages centrally located within a polymer. The ability to envelope and target the linkage seems to approximately dictate the active site structure. A pocket shaped enzymatic active site is more accommodating of terminal carbohydrate residues, whereas a cleft shaped active site allows for binding of the polymeric substrate across the active site of the enzyme, thereby allowing access to internal carbohydrate linkages[22].

1.1.4. Retaining & Inverting Mechanism

The manner in which linkages between carbohydrates (termed “glycosidic linkages”) are cleaved dictates the stereochemical configuration of the resulting product. In this regard, glycoside hydrolases (GH) exist as either inverting enzymes or retaining enzymes (Figure 1.3).

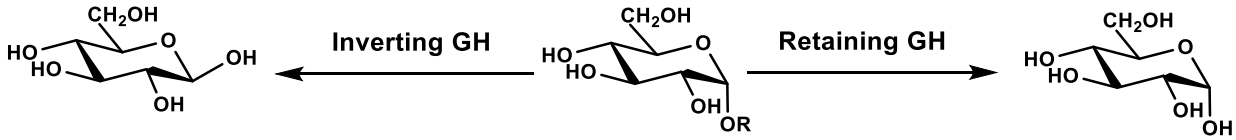

Figure 1.3. Inverted versus retained glycoside hydrolysis product
Both products result in a newly liberated hemiacetal at the anomeric position. An inverting catalytic mechanism acting on an α-glycosidic linkage as depicted above will yield β-D-glucose (left) whereas the retaining glycoside hydrolase produces the α-D-glucose isomer (right).

This inversion or retention of stereochemistry relates to the anomeric carbon found in saccharides, which is the carbon found in the hemiacetal/acetal position in a cyclically depicted carbohydrate (Figure 1.4).

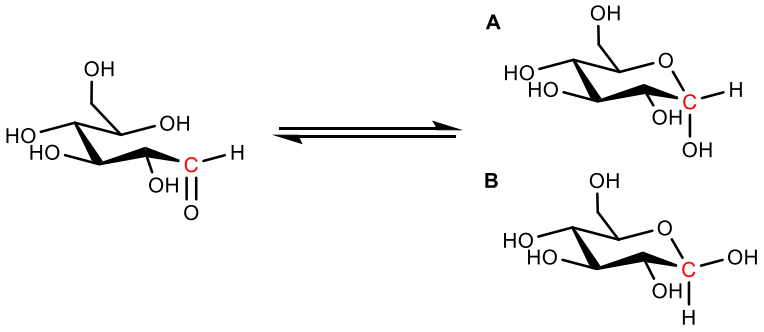

Figure 1.4. Formation of α (A) and β (B) anomers from the open chain carbohydrate glucose

One such carbohydrate PTM relevant to the aims of this thesis is the post translational addition and removal of *O*-linked β-*N*-acetylglucosamine (O-GlcNAc) to proteins inside the nucleus and cytoplasm of metazoan cells. Discovered by Torres & Hart in 1984[23], this form of glycosylation (Figure 1.5) is installed by the enzyme known as *O*-GlcNAc Transferase (OGT). *O*-GlcNAc is typically not further elongated by additional carbohydrate residues and the PTM can be hydrolytically removed by the counterpart GH enzyme *O*-GlcNAcase (OGA).

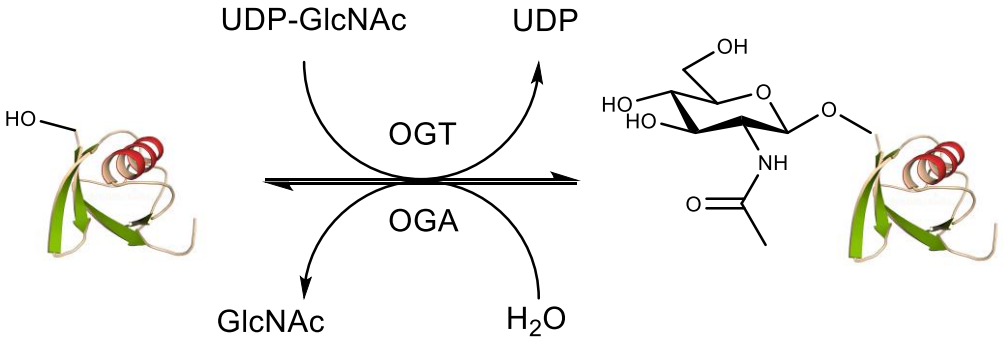

Figure 1.5. Modification of proteins with O-linked N-acetyl glucosamine
UDP-GlcNAc serves as the substrate for OGT mediated glycosylation to hydroxyl functional groups of select serine and threonine residues. The glycosidic linkage formed between GlcNAc and the aglycone protein may be cleaved by the enzymatic hydrolysis activity of OGA.

O-Linked β-N-acetylglucosamine, as the prefix in the name suggests, is covalently linked via oxygen to the serine or threonine residues on the protein targets to which GlcNAc is being installed. The hydroxyl functional groups of serine and threonine are coupled to the anomeric carbon to form a stable acetal (Figure 1.5). The stereochemical configuration of this glycoside is assigned most simply and generally – though not precisely - as either alpha or beta, depending on whether the resulting linkage is either cis (β) or trans (α) relative to the 6-position carbon atom extending from the plane of the ring.

Figure 1.6. Glycosidic Linkage Conformation
The glycosidic linkage when trans relative to the 6-position carbon atom is denoted α (A) and in this illustration appears below the plane of the ring. The inverse anomic configuration (B) whereby the 6-position carbon atom is cis relative to the glycosidic linkage is correspondingly denoted β. Drawn in this chair confirmation the β anomer glycoside appears above the plane of the ring.

Previous research has implicated the O-GlcNAc modification as playing important roles in various processes including, but not limited to, cellular signaling[24], DNA transcription[25], membrane transport[26], stress response[27], and autophagy[28]. Many of the same proteins targeted for modification by GlcNAc are also substrates for O-linked phosphorylation by a category of enzymes known as kinases. Unlike OGT, multiple distinct enzymes exist capable of phosphorylating their target substrate, while OGT is exclusively capable of installing O-GlcNAc. Taken together, OGT is sometimes considered as acting in a competitive equilibrium with various kinases (Figure 1.7), such as glycogen synthase kinase-3 (GSK-3), which shares at least 10 distinct protein substrates with OGT[29,30]. This potential interactive relationship between O-GlcNAc and phosphorylation of enzymes has been implicated in a number of disorders including diabetes[31–34], cardiovascular[33–38], cancer[31,40–42], and of particular focus in this text, neurodegenerative diseases[43].

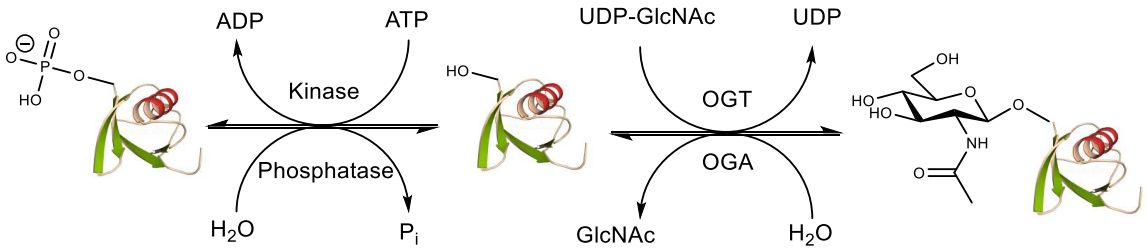

Figure 1.7. Reciprocal relationship between N-acetyl glycosylation and phosphorylation

1.2. Implication of O-GlcNAc in Alzheimer Disease (AD)

Dementia characterizes a set of symptoms affecting the brain, including memory loss, mental instability, difficulty problem solving, abnormal motor behavior, and overall cognitive decline. According to the Alzheimer's Association 2020 Disease Facts and Figures publication, AD accounts for 60-80% of all dementia cases, with approximately 1 in 10 affected individuals affected over the age of 65. The exact causes of AD are not entirely understood, but its progression correlates strongly with the aggregation of an abnormally phosphorylated protein within neurons that normally play a role in microtubule assembly and stability within cells[44,45,46]. Microtubule-associated protein Tau (Tau) protein, originally identified in 1975[47], form toxic oligomers and downstream aggregates known as neurofibrillary tangles (NFT) that are one of the pathological hallmarks of AD seen during post mortem analysis of AD affected brain tissues[48]. This

aberrant hyperphosphorylation is carried is out by many different kinases and the subsequent aggregation of toxic oligomers into NFT correlates closely with cell death and brain atrophy over time[49].

1.2.1. OGA in Tauopathies

Tau is also an example of the previously mentioned protein group that is subject to competing modification between phosphorylation and glycosylation by OGT[50,51]. Based on this understanding, previous research has made efforts to prevent NFT formation by driving this equilibrium away from hyperphosphorylation towards glycosylation. By using OGA inhibitors to reduce its glycoside hydrolase activity towards glycosylated tau, hyperphosphorylation would also be attenuated as a result of substrate reduction given that the serine and threonine residues would be covalently bound to GlcNAc residues. This reduction in hyperphosphorylation would in turn reduce tau toxicity by preventing aggregation of Tau and leading to a reduction in cell death[43,52–54]. Other proteins including β-amyloid also correlate with and are strongly implicated in the early stages of development of AD. While the function of β-amyloid is not well understood, it is the main component of amyloid plaques – another key pathological hallmark of AD. It remains unclear which of these two, if either, is definitively causative of the disease, nor whether preventing these processes can attenuate disease progression – although a large number of preclinical studies suggest this should be the case. Increased O-GlcNAcylation has been shown to be effective in preventing β-amyloid toxicity[55] via reduction of the corresponding OGA glycoside hydrolase activity[56]. An alternative and independent effort is focused on selectively inhibiting GSK-3, a kinase implicated in tau hyperphosphorylation and increased β-amyloid production[57]. Phase II clinical trials for this inhibitor (Tudeglusib) are underway as of 2017, however, the drug is yet to be shown to be effective (Identifier: NCT03692312).

In addition to Alzheimer's Disease, Parkinson's Disease (PD) is another dementia that manifests itself in the nervous system. This impairment of the body's relaxed or fine motor control may lead to almost complete loss of voluntary muscle function, hallucination, unintelligible speech, and additional comorbidities. The pathophysiology of PD is characterized by death of the brain's dopaminergic neurons, which is though to stem from the oligomerization and downstream aggregation of the protein α-synuclein to form the pathological hallmark of PD referred to as Lewy bodies[58].

Similarly to the phenomenon observed with tau and β-amyloid in the case of Alzheimer's Disease, increased O-GlcNAcylation has shown to reduce aggregation and toxicity of α-synuclein toward neuronal cells[59]. As such, targeting the hydrolytic activity of OGA responsible for the removal of O-linked GlcNAcylation from the nice serine and threonine residues found on α-synuclein is a potential therapeutic strategy of some interest.

1.3. Small Molecule Inhibitors as Tools to Probe Glycan Processing Enzymes

Small molecules are conventionally associated with their application as drugs as medical therapeutics to treat a disease or pathology. In this context, they are meant to physiologically alter an organism in some specific and medically relevant manner. While some small molecules may serve to enhance the function of their targets, small molecules more commonly serve as inhibitors intended to attenuate selective enzyme function. Beyond this role however, small molecules can themselves be used as tools to probe and elucidate the function of proteins within their biologically relevant environment. The structure of small molecule inhibitors that bind to the active sites of enzymes often mimic that of the natural substrate – though not always. Unsurprisingly perhaps, such inhibitors exploit certain functionalities to allow binding to the target enzyme in the same manner as the natural substrate.

1.3.1. Inhibition of OGA

The structure of the active site of an enzyme target to which the natural substrate binds may provide clues into the catalytic mechanism and associated transition states used by the enzyme. Such information can be applied towards the rational design of an analogous molecular probe - targeting the same active site and closely mimicking the high-energy transition state. Iterative changes to the analogous probe may significantly improve the overall binding affinity and produce a molecule capable of readily outcompeting the natural substrate for the enzyme active site, leading to inhibition of the enzyme.

Such an approach was applied towards the development of inhibitors for OGA. Previously published work in the lab had uncovered the 2-acetamido of the natural substrate acts in what is termed a substrate-assisted catalytic mechanism in which an

oxazoline intermediate figures prominently[17,60]. Based on these findings, the selection of a compound structurally similar to the high energy oxazoline intermediate or a closely derived transition state (Figure 1.8) yielded NAG-thiazoline as a potent inhibitor of OGA. Iterative variations of the oxazoline ring substituents allowed for further improvement in selectivity for OGA (NBut-GT) over other functionally related enzymes. Kinetic and structural studies implicated aspartate 242 in the enzyme as a key carboxylate group that acts in its deprotonated form at physiological pH as a general catalytic base. It was postulated that increasing the pK_a of the inhibitor NBut-GT may serve to boost binding between the interacting aspartate 242 residue (pK_a 5.2) and the inhibitor. To this end, an additional exocyclic nitrogen was used a bioisosteric substitution to NBut-GT to increase the basicity of the thiazoline ring at the site of interaction with aspartate 242. The pK_a of the thiazolinium ion was experimentally found to be 8.0 and it is accordingly mostly in its protonated form at physiological pH (7.4) which is believed to allow for significantly improved binding between the inhibitor and aspartate residue by harnessing a close range ionic interaction. The rational design of this new inhibitor (K_i = 2.1 nM) was a significant 37 fold improvement upon the original work (NAG-thiazoline K_i = 78 nM)[61].

Following the design of Thiamet-G, in vivo experiments were able to demonstrate its ability to effectively reduce phosphorylation of tau protein in animal cells and suggesting a possible novel strategy to attenuate the formation of pathologic tau oligomers[61]. MK-8719, a fluorinated derivative of Thiamet-G, has since been developed as a potential therapeutic candidate in a partnership between the biotechnology company Alectos Therapeutics and the multinational pharmaceutical giant Merck. Focus on improved pharmacokinetic properties yielded a compound with excellent blood brain barrier permeability, confirmed target engagement using PET imaging with an ^{18}F-labelled PET agent, and attenuation of NFT and brain atrophy in mouse models[62]. MK-8719 has successfully completed Phase I clinical trials in humans as of 2017 and was granted orphan drug status by the Food and Drug Administration (FDA). Further research remains to be carried out regarding the applicability of OGA inhibiting compounds like MK-8719 towards α-synuclein toxicity and Parkinson's Disease.

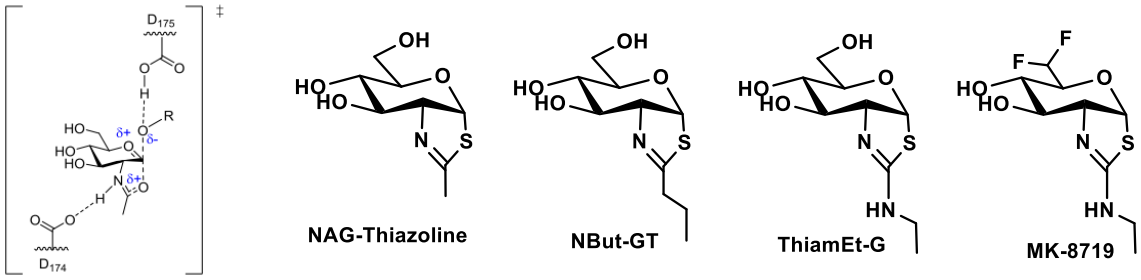

Figure 1.8. Transition state inspired inhibitors of OGA

1.4. Transporters

In addition to glycoside transferases and hydrolases, there exists another class of enzymes known as transporters (or permeases). These proteins serve to transport molecules without covalently modifying them in the process. Transporters facilitate the influx and efflux of ions, nutrients, neurotransmitters, and even drugs between the cell and the extracellular matrix. They are broadly divided into two groups - channels or carriers. The former is categorized by the exclusive use of passive diffusion to transport substrates in the direction of their electrochemical or concentration gradient, allowing for upwards of millions of molecules to pass through simultaneously. By contrast, carriers may transport their substrate passively through diffusion or via active transport - as would be required in the movement of particles from an area of low concentration to an area of high concentration. Both forms typically exist exclusively as transmembrane proteins where they are embedded within cellular membranes. Active transport may function in a coupled manner whereby the target substrate is exchanged for an ion such has H^+ or Na^+ or use energy in the form of nucleoside triphosphates.

1.4.1. Carbohydrate Transport

While molecules exist that can freely permeate the cell membrane, these are generally limited to small and relatively nonpolar compounds not typical of branched and polar carbohydrates. The relative impermeability of the lipid bilayer membrane to carbohydrates means that their uptake is often facilitated by transporters. Some carbohydrates, such as D-glucose, may be taken up by cells via facilitated diffusion, whereby D-glucose is transported across the cell membrane through glucose-specific

(GLUT) transporters. Other carbohydrates such as β-(1,4) linked disaccharide composed of *N*-acetylglucosamine and *N*-acetylmuramic acid (GlcNAc-anhydro-MurNAc) rely on an active transporter that depends on coupled exchange of a proton to facilitate transport.

The directional flow of this coupled exchange determines whether the transporter is denoted as a uniporter, symporter, or antiporter. Transport of a single molecule or ion in a single direction constitutes a uniporter, while the addition of a second ion or molecule in this exchange – travelling in the same or opposite direction – identifies the transporter as a symporter or antiporter, respectively.

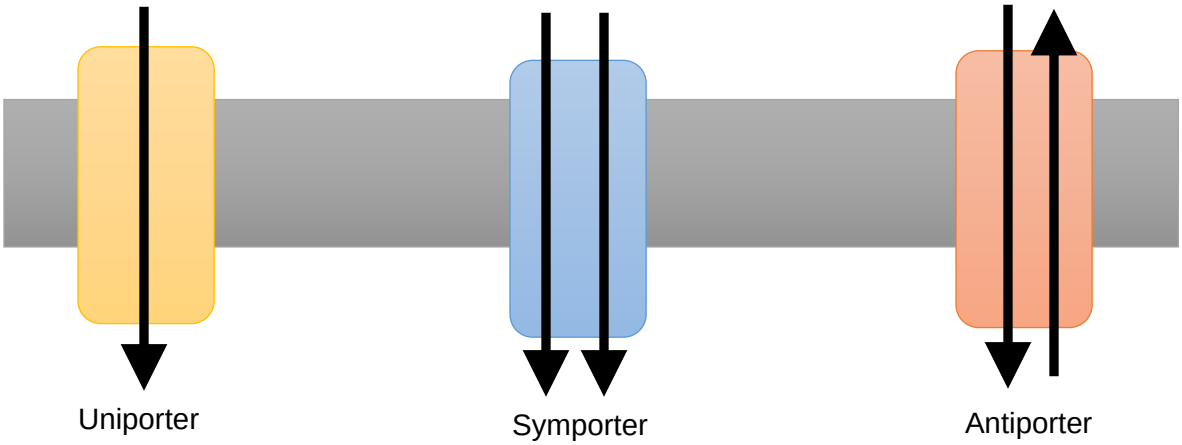

Figure 1.9. Categories of trans membrane enzyme transport

1.4.2. Gram-Negative Bacteria and AmpG Transport

One of the many pathways in which transporters play a central role in the cell is in the peptidoglycan recycling system of Gram-negative bacteria. The peptidoglycan network exists between the inner and outer membrane of Gram-negative bacteria. It is composed of disaccharide units of β-(1,4) linked *N*-acetylglucosamine and *N*-acetylmuramic acid (GlcNAc-anhydro-MurNAc) cross-linked with one another via short peptide chains pendent to the lactyl group of the MurNAc residue. This mesh-like framework constitutes the cell wall in Gram-negative bacteria, serving to provide structural support in addition to counteracting the osmotic pressure between the cytoplasm and external medium.

These disaccharide constituents are fragmented by enzymatic cleavage within the cell, recycled, and recirculated back into the peptidoglycan during the life of the

bacterium. Gram-negative bacteria contain a secondary cell membrane enclosing the cytoplasm. Between this inner cytoplasmic membrane and the outer cell membrane exists the periplasmic layer where free floating peptidoglycan fragments exist. To be further processed, a symporter embedded in the inner membrane of Gram-negative bacteria internalizes the periplasmic monomers of GlcNAc-anhydro-MurNAc. This transporter, known as AmpG, is believed to be dependent upon the proton motive force to simultaneously internalize both a proton as well peptidoglycan metabolite[63]. In this manner, AmpG exploits the electrochemical concentration gradient across the cell membrane to initiate conformational changes in its domain structure. These changes are believed to facilitate an alternating access mechanism which constitutes the binding, internalization, and release of its carrier molecule and ion. Beginning with the recruitment of a proton, the enzyme remains in an "outward-facing" conformation. The subsequent binding of the disaccharide substrate induces a conformation change in the enzyme such the substrate and proton are now exposed to the intracellular cytoplasm and are internalized past the inner membrane. With the release of the substrate and proton, the enzyme is free to revert back to its outward facing conformation and catalyze the uptake of another substrate.

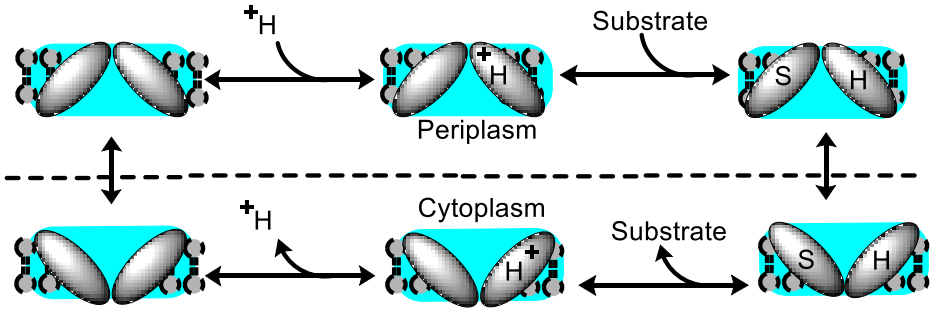

Figure 1.10. Alternating access mechanism
Binding of a proton prior to the substrate is depicted. This is followed by conformational change of the membrane bound enzyme to allow for cytoplasmic internalization of the proton and substrate.

1.4.3. The Peptidoglycan & Antibiotics

One of the most commonly prescribed classes of antibiotics, known collectively as β-lactams, rely on a mechanism that targets the structural integrity of the peptidoglycan layer. These compounds act by inhibiting formation of the cross links formed by Penicillin Binding Proteins (PBP). These PBP are covalently inactivated by β-

lactams, rendering them unable to catalyze cross linking of the short chain peptides[64]. In the absence of these cross-links, the cell becomes unstable and is not able to sufficiently replenish the peptidoglycan and GlcNAc-anhydro-MurNAc begins to accumulate within the cell. In the course of reproduction, Gram-negative bacteria such as *Escherichia coli* will break down more than 60% of their cell wall in order to divide and prepare new cell wall for their progeny. Without this capacity, the cell rigidity is structurally compromised and the cell is no longer viable to reproduce[65].

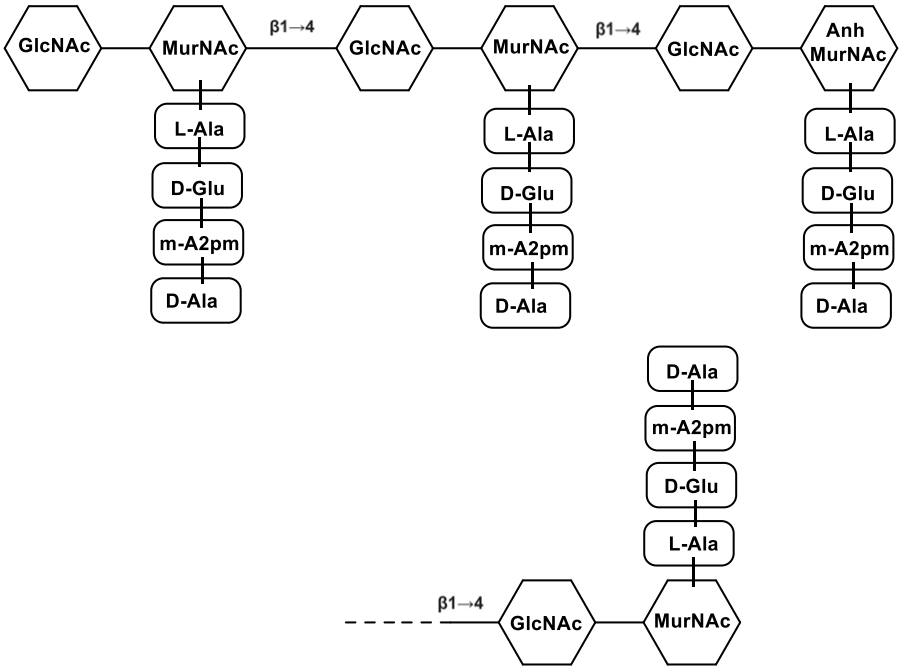

Figure 1.11. Peptidogylcan network of β-1,4 linked glycosides and pendant peptide residues

The success of β-lactams as antibiotics is evident in their wide-spread use and their development into drugs such as amoxicillin, ampicillin, and penicillin. Since the discovery of penicillin in 1928 and its subsequent widespread application in humans during the second world war, numerous derivatives of the core β-lactam structure have been developed in an effort to escape the emergence of antibiotic resistance[66].

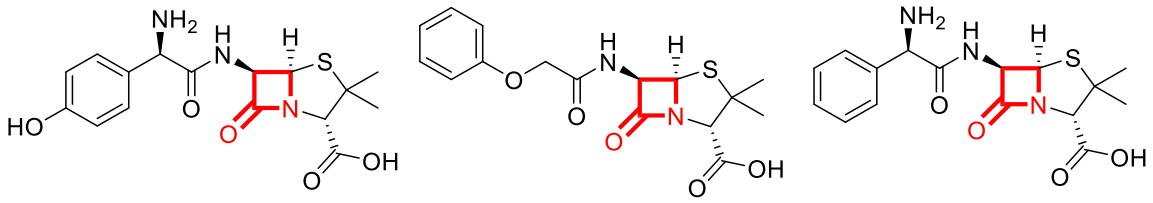

Amoxicilin Penicillin-V Ampicillin

Figure 1.12, Well known β-lactam antibiotics

One form of resistance mechanism harbored by Gram-negative bacteria is the production of β-lactamases. These enzymes are responsible for hydrolyzing and thereby inactivating the antibiotic β-lactam core, leaving them unable to covalently inactivate PBPs. For exactly this reason, physicians often prescribe β-lactamase inhibitors, such as clavulanic acid, in conjunction with β-lactam antibiotics.

1.4.4. GlcNAc-anhydro-MurNAc & Antibiotic Resistance

The accumulation of GlcNAc-anhydro-MurNAc inside the cytoplasm of Gram-negative bacteria is thought to drive transcriptional activation of the AmpC β-lactamases system. Cell exposure to β-lactam antibiotics inhibits PBPs and drives the peptidoglycan recycling pathway towards an excess of disaccharide substituents in the periplasm of the cell. Active transport of these fragments by AmpG into the cytoplasm facilitates transcriptional activation AmpC β-lactamases which proceed to hydrolyze the β-lactam antibiotics. This negative feedback loop serves to produce antibiotic resistance-conferring enzymes only in the presence of the downstream effects of β-lactam exposure. Inactivation of AmpG, preventing cytoplasmic internalization of the disaccharides that act as AmpC transcriptional activators, has been shown to restore susceptibility to antibiotics in antibiotic resistance strains of Gram-negative bacteria[67]. Inhibiting transport of these cell wall fragments to prevent activation of the AmpC antibiotic resistance mechanism will be, in part, the focus of discussion below.

1.4.5. A Transport Assay for AmpG Permease

Previous live cell assays carried out in the Vocadlo laboratory have successfully demonstrated the ability of the AmpG transporter to internalize a variant of the natural disaccharide substrate. That proof of concept study showed how appending a

fluorophore to the GlcNAc-anhydro-MurNAc disaccharide in place of the short chain peptides was tolerated and that fluorescence was internalized[68]. As a control, it was shown that genetic inactivation of the AmpG transporter prevented the retention of any fluorescence signal following successive washes of cells, indicating no internalization had taken place. The fluorescent probe allowed a way of monitoring transporter activity, whereby potential inhibitors of transporter could be screened and evaluated.

In order for the assay to function it was still necessary to process the cells by removal of the outer peptidoglycan cell wall and outer membrane. This procedure exposed the inner membrane of the Gram-negative bacterium to the extracellular media in which the fluorescent probe is present. Even with careful manual handling throughout the several hours of washing, centrifugation, and resuspension, the cells are sensitive and tend to rupture. Removal of the cell wall and outer membrane also renders the cells unable to replicate, and vulnerable to lysis from osmotic pressure. These factors together made it impossible for the assay as originally designed to be applied to high throughput screening (HTS) without significant measures being taken to increase the robustness, consistency, and efficiency of the assay.

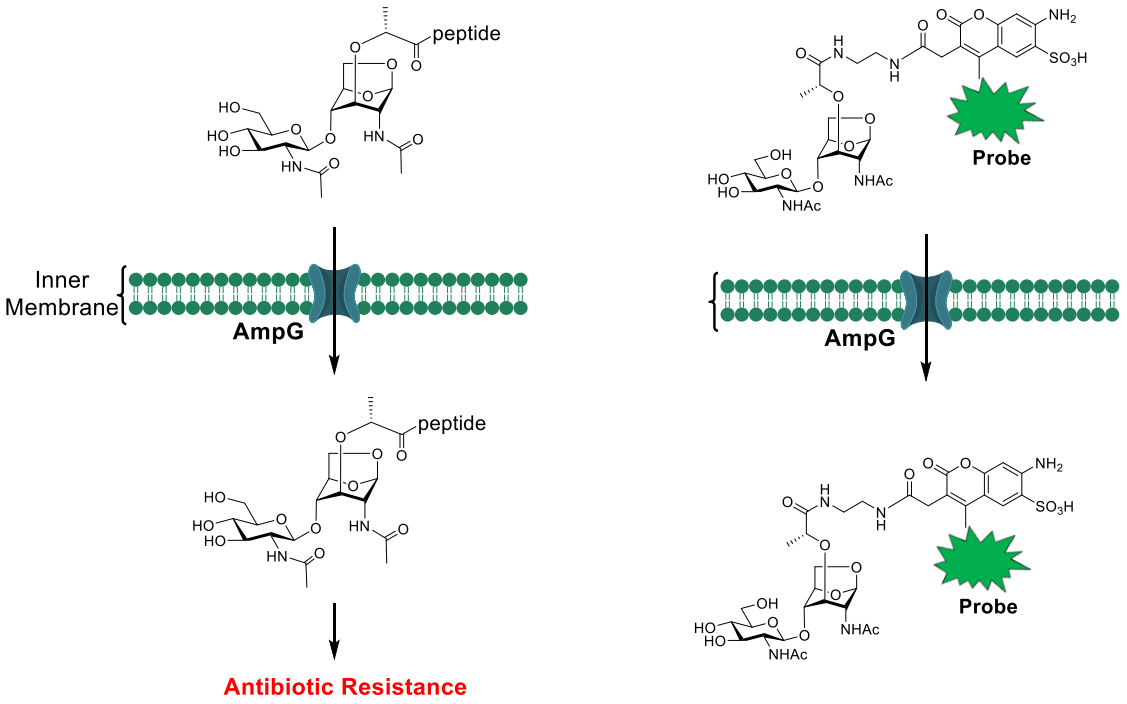

Figure 1.13. Fluorescent based exploitation to monitor AmpG transport
Substitution of the natural substrate pendant peptides with a fluorophore allowed for monitoring of AmpG activity in a live cell fluorescence uptake assay.

1.5. Aims of the Thesis

The research outlined in this thesis aims to improve upon two existing tools available to the research community in the study of carbohydrate processing enzymes and their relevant systems.

The first tool and primary focus of this thesis is to improve on a previously established sugar transport assay to make it amenable to high through-put screening. I used information uncovered in the original assay regarding AmpG substrate tolerance and applied this to the rational design of novel probes intended to improve the efficiency, consistency, and signal quality of the assay. In particular, the strategies and syntheses used to generate these probes, and their suitability in monitoring transport activity in live cells, will be discussed. Such improvements would enable an assay compatible with automated high-throughput screening (HTS) against libraries comprising of many thousands of compounds to facilitate the identification of leads that could become potential therapeutics to combat AmpC antibiotic resistance.

The secondary topic of my thesis concerns the synthesis of the OGA inhibitor Thiamet-G. The existing synthetic protocol is evaluated and revisions are made to facilitate dramatically increasing the scales of reactions used in its chemical synthesis while maintaining both high product purity and yield. Continuing research using this widely applied tool compound and its derivative forms, such as the clinically relevant OGA inhibitor MK-8719, highlight a need for a more facile, clean, and economical synthesis. This topic is particularly relevant given the quantities of Thiamet-G necessary to carry out large scale animal studies as is currently being done in our laboratory as well as those of collaborators. The research described below reduce the use of toxic reagents, eliminate the need for chromatographic purification steps, and have the potential to save several hundreds of thousands of dollars in commercial manufacturing costs. The final product, performed at a scale approaching production of one kilogram of Thiamet-G, has been used directly for neurodegenerative studies of OGA transgenic mice in Parkinson Disease (PD) research.

Chapter 2. Developing High Throughput Amenable ampG Transporter Assay

2.1. Contributions

This work is based on the AmpG transporter assay originally developed in a multidisciplinary collaboration involving synthetic chemistry performed by Dr. Anuj Yadav, genetic manipulation by Judith Winogrodzki, and assay development by Evan Perley-Robertson. My role has been an extension of this work drawing from previously established information in all three areas of synthesis, cell preparation, and assay execution. My primary efforts were in the synthesis, design, and application of novel probes.

2.2. Abstract

Many Gram-negative bacteria pose a serious societal health concern in the form of hospital acquired (nosocomial) infections. These infections often manifest themselves in the form of illnesses including pneumonia, sepsis, urinary tract infection, and surgical site infection. Conventional treatments for these illnesses are the use of antibiotics, which have become so widely used and improperly administered that β-lactamase antibiotic resistance has arisen as a formidable long-term concern in fighting infections. β-Lactamase inhibitors such as clavulanic acid are often co-prescribed with β-lactam antibiotics but these are ineffective against AmpC β-lactamases. Previous work has demonstrated the dependence of Gram-negative bacteria on an inner membrane muropeptide transporter to enable high level induction of AmpC in the presence of β-lactams. The ability to monitor activity of this transporter would allow screening to identify inhibitors capable of preventing AmpC β-lactamase induction. Recently, novel fluorescent probes and cell processing techniques to expose the inner membrane transporter have been used in tandem to visualize transporter activity. Stripping the outer membrane of these bacterial cells during the required processing and visualization techniques causes considerable lysis along with consequent reductions in signal. Moreover, the AmpG transporter substrates are constitutively fluorescent, complicating their use in HTS. Described herein is an attempt to devise a novel substrate probe that

becomes fluorescent only upon internalization by cells thereby allowing for the direct screening of AmpG inhibitors on a high throughput platform.

2.3. Introduction

2.3.1. Nosocomial Infection

Nosocomial infections are not exclusively a concern of the impoverished world, nor are they exclusively the result of bacterial infections. Despite this, bacteria are the most common cause of nosocomial infections, far exceeding (80%+) that of fungal and viral cases. The World Health Organization (WHO) reported that of every 100 hospitalized patients, 7 in developed countries and 10 in developing nations would become infected[69]. The duration of hospitalization is also very closely linked to likelihood of infection. The Extended Prevalence of Infection in Intensive Care (EPIC II) study found that upwards of 51% of patients admitted to the hospital ICU acquired some kind of nosocomial infection in various ways – ranging from direct human contact and moist instrumentation to ventilation based airborne transmission[69]. The majority of these infections stemmed from Gram-negative bacteria (62%) and were caused by Staphylococcus, Acinetobacter, and Pseudomonas genera. These nosocomial infections translated into a mortality rate of more than double that of non-infected patients (25% vs. 11%)[69].

2.3.2. Gram-Negative Bacterial Infection Treatment

β-lactam antibiotics have been used as a staple in the treatment of bacterial infections, serving to inhibit essential penicillin binding proteins (PBP) that are responsible for the integrity of the bacterial cell wall. These PBP transpeptidases interlink the murein cell wall are inactivated upon covalent modification by β-lactam antibiotics. The inability of the cell to sufficiently replenish its peptidoglycan cell wall compromises bacterial cell division and increases susceptibility to lysis from osmotic pressure[65].

The resistance mechanism that has evolved that enable the survival of Gram-negative bacteria in response to this class of antibiotics is to produce β-lactamases that are capable of hydrolyzing the core β-lactam structure (Figure 2.1) .

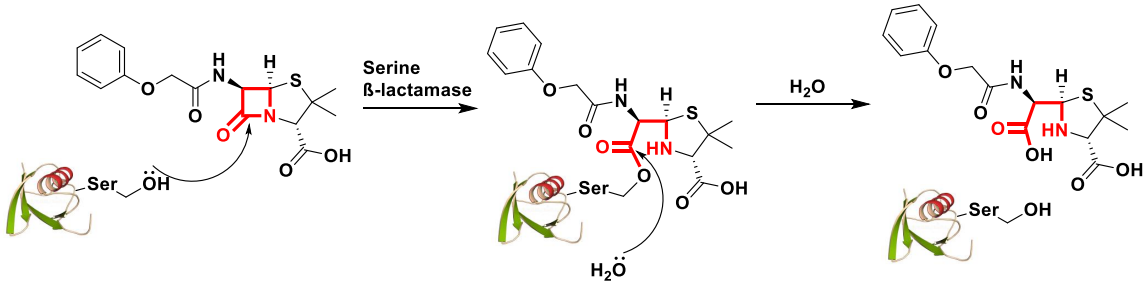

Figure 2.1. Enzymatic cleavage of β-lactam antibiotics.
The chemical mechanism outlining hydrolysis of the core β-lactam structure is shown. Lone pair electrons from a serine residue hydroxyl group in the enzyme active site bind covalently to the β-lactam carbonyl carbon. This opens the β-lactam ring as the cyclic amide is converted into a secondary amine. Attack by a water molecule subsequently liberates the enzyme for additional catalysis

2.3.3. β-lactamase Enzymes

The classification of β-lactamases is based on functional characteristics and differences in amino acid sequences and protein structures of the four generally recognized classes A, B, C, and D. Classes A, C, and D inactivate β-lactams using a nucleophilic serine residue involving a mechanism in which an acyl intermediate is formed prior to hydrolysis (Figure 2.1)[70]. Class B β-lactamases are metalloenzymes and rely on the use of a zinc ion for hydrolysis. Conventional treatment in response to β-lactamase mediated β-lactam resistance has been to co-prescribe β-lactamase inhibitors such as clavulanic acid in addition to the primary antibiotic. Clavulanic acid and analogous compounds are not effective against all forms β-lactamase enzymes – particularly against a subgroup of Class C enzymes known as AmpC.

The SENTRY antimicrobial surveillance program carried out in 2004 collected *Escherichia coli* isolates from 30 medical centers in North America and found 5% of the samples to contain AmpC[71]. In the proceeding years reports of the prevalence of extended spectrum β-lactamases such as AmpC has continued to rise. The Study for Monitoring Antimicrobial Resistance Trends (SMART) was an ongoing surveillance program to monitor trends in Gram-negative bacteria isolated from patient abdominal infections in 37 participating nations. Their reports showed year over year increases in extended spectrum β-lactamase (ESBL) prevalence, with of 18% of *E. coli* and 26% *K. pneumoniae* possessing such a resistance mechanism[72] . The horizontally acquired

resistance mechanism seems to be of particular concern in less developed nations, where hospitals how reported upwards of 47% of clinical isolates harbor AmpC[73].

AmpC is the only class of β-lactamase for which expression is induced, in response to exposure to β-lactams, by the transcriptional activator AmpR[74]. AmpC β-Lactamase expression is usually repressed in the absence of β-lactams. Upon exposure to these antibiotics, anhMurNAc-peptide fragments derived during recycling of the peptidoglycan accumulate inside the cytoplasm where they displace the repressor molecule normally bound to AmpR (Figure 2.2). This displacement of the cell wall anabolic metabolite, UDP-MurNAc-pentapeptide, in turn drives transcription of the AmpC gene by AmpR and its downstream translation to produce clavulanic resistant AmpC β-lactamases that proceed to hydrolyze the administered β-lactam antibiotics . Upon return of the anhMurNAc-peptide fragments to basal levels, the AmpR is once again by bound UDP-MurNAc-pentapeptide and inducible expression of AmpC ceases[74].

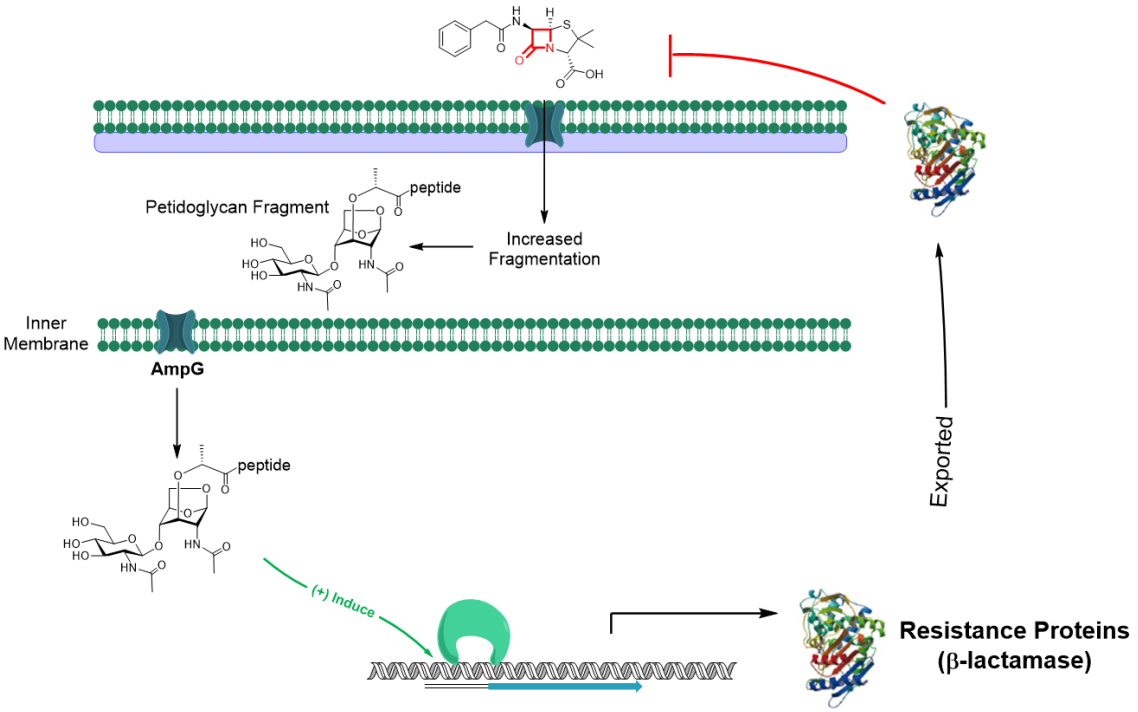

Figure 2.2. Peptidoglycan recycling pathway
The steps following exposure of a Gram-negative AmpC bacterium to antibiotics is depicted. The peptidoglycan wall is illustrated as the purple layer below the outer membrane. Increased peptidoglycan fragmentation in light of PBP inhibition and missing peptide crosslinks leads to a cytosolic accumulation of the disaccharide through the AmpG transporter. These fragments are further metabolized to yield transcriptional activators subsequently activating AmpC

transcription and producing β-lactamases in a negative feedback form to destroy the invading penicillin. Adapted, with permission, from Perley-Robertson 2016.[75]

2.3.4. Peptidoglycan Fragments

In order to activate the AmpR transcriptional regulator that is normally bound by UDP-MurNAc-pentapeptide to repress β-lactamase expression, anhMurNAc-peptides must accumulate in appreciable quantities inside the cytoplasm of the bacterium[20]. AnhMurNAc-peptides have peptides of between three and five residues pendent to the lactyl group of the MurNAc residue, and the are the product of cleavage by the glycoside hydrolase NagZ, which acts on a GlcNAc-anhydro-MurNAc-peptide substrate[17,20]. GlcNAc-anhydro-MurNAc-peptides can only move from the periplasmic space between the cell wall and inner membrane into the cytoplasm via the active proton driven antiporter AmpG. Targeting the internalization of GlcNAc-anhydro-MurNAc-peptides by inhibiting AmpG thus remains a potential therapeutic approach to decommission the activation of AmpC β-lactamase expression.

2.3.5. Established Proof of Concept

Previous research done in a collaboration between the Vocadlo and Mark laboratories have explored this strategy by modifying the natural substrate of AmpG, GlcNAc-anhydro-MurNAc-peptide, by replacing the short peptide chain with a fluorophore[68]. The choice in making this substitution was based on earlier work demonstrating uptake of radiolabeled PG fragments, suggesting that the 3-5 amino acid peptide was not necessary for uptake of the disaccharide[76]. In addition to synthesis of a fluorescent substrate, previous freeze-thaw strategies used to expose the inner membrane transporter were used in combination with chemical reagents to remove the cell wall and outer membrane. This method of generating what are known as spheroplasts included the use of lysozyme to cleave the PG cross links, as well as EDTA as a divalent cation chelator to disrupt calcium function in the outer membrane[68]. By using a genetic knockout of the AmpG transporter in bacterial cell lines as a negative control, the team also provided a means of ensuring observed activity and downstream AmpC induction could be directly attributed to loss of AmpG transporter function. Taken together, this approach was used to successfully show uptake of the fluorescent probe and demonstrate its selectivity for AmpG in a consistent and kinetically quantifiable

manner[68]. This work represented the first fluorescent-based transport assay for a periplasmic transporter and laid the groundwork for an approach towards screening for potential inhibitors of the transporter enzyme.

A number of obstacles, however, arose in envisioning translating this proof-of-concept approach to an assay compatible with high-throughput screening (HTS). Following incubation of cells in spheroplasting solution, the freshly prepared spheroplasts, chemically stripped of their cell wall and outer membrane, are subjected to successive cycles of centrifugation, resuspension, and washing. These cycles serve to remove extracellular probe from the media and isolate only the signal emanating from the AmpG substrate that has been taken up inside the spheroplasts. The process itself not only likely ruptures numerous spheroplasts, but also requires hours of manual handling and pipetting before any results can be obtained. Such a protocol would not be feasible when tested against chemical libraries containing thousands of compounds. Even with the availability of centrifuge and plate washer devices built into the automated screening platform, efforts to replicate the results of the manual protocol failed. In particular, pellets of the spheroplast obtained by centrifugation were unable to be resuspended in an automated manner and washing proved inefficient when the retentate following centrifugation of 384-well plates could not be drained. Developing a new assay that allowed for imaging directly following incubation would enable a simple and HTS compatible approach to screening for AmpG inhibitors on a large scale.

2.4. Results and Discussion

2.4.1. Design of Substrate

Two strategies were initially considered in addressing the previously mentioned hurdles towards development of a high through-put screening assay for AmpG activity. As with the original live cell transporter assay, both approaches relied on detectable fluorescence activation from within spheroplasts.

2.4.2. Fluorescence Quenched Approach

The first strategy was to exploit the quenching effects in the Förster Resonance Energy Transfer (FRET) phenomenon. Here energy is transferred in a non-radiative

manner between a donor (fluorophore) in an excited electron state and an acceptor (quencher) dye. The spectral overlap between the emission band of the donor and the excitation band of the acceptor, along with their physical proximity (up to approximately 100Å) dictate, in a distance-dependent manner the extent to which FRET occurs. In the design I contemplated here the donor and acceptor are two separate molecules. In order for such an approach to be feasible for a live cell assay, it is necessary to use a highly polar quencher compound that cannot diffuse into or be transported into the cells. Furthermore, a quencher having the appropriate excitation wavelengths must be selected such that there is ample overlap between the emission band of the FRET donor with the absorption band of the FRET acceptor. By incubating spheroplasts in a medium containing a high concentration (>50 mM) of a quencher compound, I reasoned that any fluorescence originating from outside of the cell should be quenched. Since the quencher compound is incapable of being internalized, a fluorescent substrate transported by AmpG into the spheroplast would no longer be within effective range for FRET quenching to occur. In this manner the only detectable signal would be emitted from fluorophores internalized by the spheroplasts. Toward this goal, several fluorophore-quencher pairs were evaluated for their suitability based on brightness, size, stability, availability, and wavelength. Ultimately, BODIPY-Fl was selected for its high quantum yield (0.81), extinction coefficient (80,000 $cm^{-1}M^{-1}$), and red shifted excitation wavelength as compared to the originally used AlexaFluor350 fluorophore (503nm vs. 350nm). Shorter wavelengths such as that of the probe used in the proof-of-concept assay results in some interference from autofluorescence arising from cells and spheroplasts that can complicate the sensitivity of the assay.

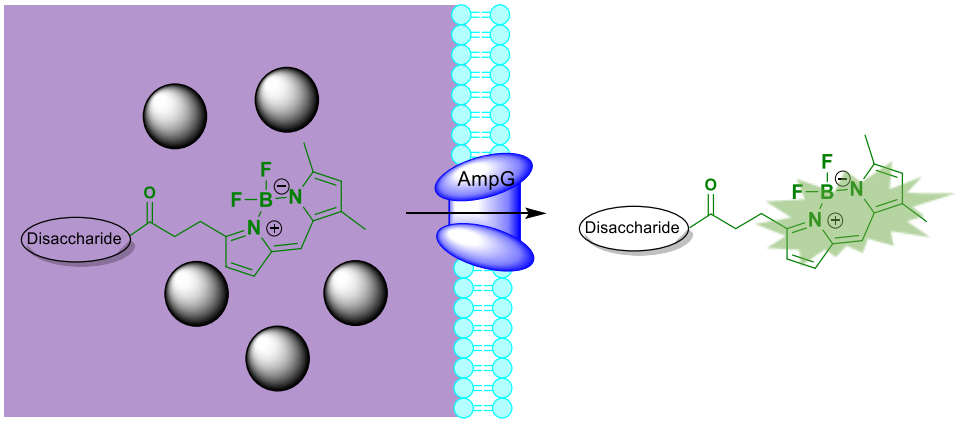

Figure 2.3. Extracellular fluorescence using membrane impermeable FRET
Cell membrane impermeable FRET acceptor molecules, depicted as black spheres in the figure above, are shown to quench all donor molecule signal emitted from outside of the cell. Once the probe (BODIPY-Fl appended to the disaccharide natural substrate) is internalized into the cytosol via AmpG, the donor molecule is no longer in the proximity of FRET acceptor molecules for effective FRET quenching to occur.

2.4.3. Uncaging Enzymatic Approach

The second approach to designing an assay that would allow for directly detecting AmpG transport activity using spheroplasts without extensive sample handling involved further exploitation of the substrate tolerance of AmpG. I reasoned that chemical caging of the fluorophore with a functional group that could only be cleaved once inside spheroplasts could bypass the need for an external quencher. It is known that certain phenolic fluorophores, such as resorufin or umbelliferone, will only fluorescence significantly as the anionic phenolate. Acylation of the phenolic hydroxyl group with a moiety that can be cleaved by cytoplasmic esterases within the cell would lead to fluorescence only emerging within the spheroplasts from uncaged fluorescent AmpG substrates that have been transported into the spheroplasts (Figure 2.4).

Coumarins such as the difluorinated coumarin Pacific Blue (3-carboxy-6,8-difluoro-7-hydroxycoumarin) appeared to be a suitable choice for several reasons. Sterically, their small size makes them less likely to interfere with tolerance of the disaccharide substrate by AmpG. The phenolic hydroxyl group must be deprotonated to enable bright fluorescence and therefore provides a logical site for caging the fluorophore. Situated on the opposite end of the molecule, the carboxylic acid can serve as a site for coupling to the disaccharide natural substrate. Furthermore, the Vocadlo lab

already possessed gram quantities of Pacific Blue, which also alleviated the financial burden of acquiring such a precious compound for an experimental synthesis.

The known susceptibility of phenolic acetates to spontaneous hydrolysis led to the search for more stable acyl caging groups – chemical modifiers that supressed fluorescence activity normally present in the anionic and unmodified form of the fluorophore. The stability of various esters and acyloxymethylethers of umbelliferone in aqueous solution have been examined in the literature for their rate of spontaneous hydrolysis. These findings suggested that a pivaloxymethyl ether (POM) exhibited robust stability[77] and I therefore selected this as the lead caging group for this enzymatic approach towards the AmpG transporter assay.

Uncaging of fluorescence involving fluorophores caged using acyloxymethylethers proceeds in a two-step mechanism, whereby enzyme hydrolysis of the ester bond first exposes a hydroxymethyl ether on the substrate. The inherent instability of this newly formed hemiacetal leads to its spontaneous break down to form formaldehyde and the liberated fluorophore, which can now be deprotonated and fluorescence[77].

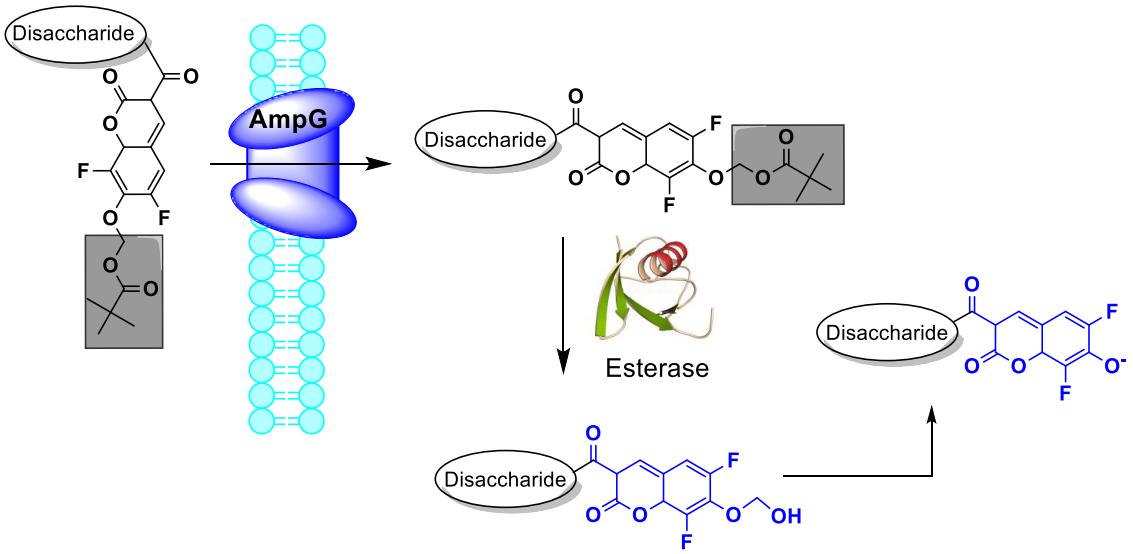

Figure 2.4. Fluorescence release following cytoplasmic internalization and enzymatic uncaging.
The natural disaccharide substrate is appended to a pivaloxy methyl ether caged coumarin. Following internalization of this intact probe via AmpG, cytoplasmic esterases within the cell presumably cleave the pival ester moiety to yield a hemiacetal which in turn rapidly decomposes into formaldehyde and the freely fluorescent anionic coumarin.

2.4.4. Synthesis of a Common Disaccharide Intermediate

Testing of both the enzymatic and quencher-based approaches required synthesis the GlcNAc-anhMurNAc disaccharide from which the fluorescent probes are derived. This work was largely based on a previous protocol published in 1986 by the German chemists Paulson, Himpkamp, and Peters[78]. The route is a convergent synthesis of the individual monosaccharides *N*-acetylglucosamine (GlcNAc) and 1,6-anhydro-*N*-acetylmuramic acid (Scheme 2.1). Commercially available tri-O-acetyl-d-glucal (**1**) was de-O-acetylated using catalytic quantities of sodium methoxide in methanol to give quantitative yields of d-glucal (**2**). The 1,6-anhydrosugar was subsequently formed using bis(tributyltin) oxide using the methods of Malik et al.[79] followed by installation of iodine at the 2 position carbon to give anhydrosugar **3**. Formation of the C2-C3 epoxide was carried out using excess sodium hydride leading to displacement of iodine via the C-3 alkoxide, allowing for selective benzylation of the remaining C-4 hydroxyl to form epoxide **4**. Ring opening of the epoxide was done using NaN_3 , leading to installation of the azide at the C-2 position to generate azide **5**. Alkylation of the now liberated C-3 hydroxyl using ethyl (S)-2-trifluoro methylsulfonyloxy propionate produces ester **6**. Reduction and *N*-acetylation of the azide using palladium on carbon under a hydrogen atmosphere followed by treatment with acetic anhydride in pyridine furnished MurNAc **7**. Deprotection of the C-4 hydroxyl using pressurized hydrogenation fostered glycoside acceptor **7** that was needed to build the target AmpG substrates.

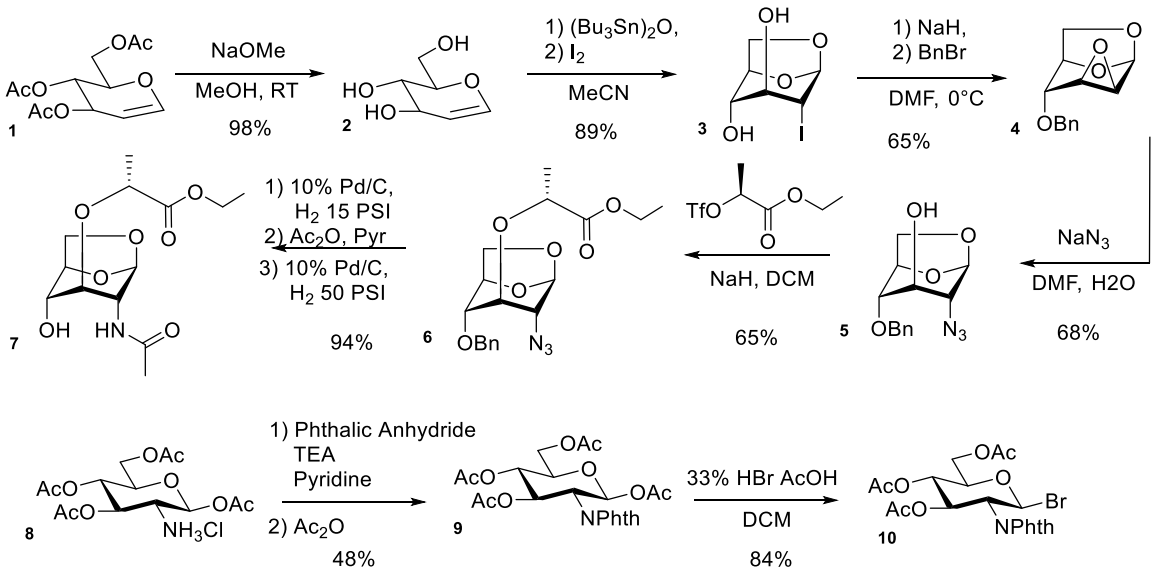

Scheme 2.1. Synthesis of GlcNAc-AnhydroMurNAc fragments

Synthesis of the glycoside donor (Scheme 2.1) began using 1,3,4,6-tetra-O-acetyl-2-amino-2-deoxy-β-D-glucopyranose hydrochloride (**8**) as the starting material, which I generated using well established methods from D-(+)-glucosamine[80,81]. Steric hinderance from installation of the phthalamide protecting group on the amine (**9**) ensured the correct β-bromo stereochemistry of the glycosyl bromide using hydrobromic acid in glacial acetic acid to yield the desired glycosyl donor (**10**).

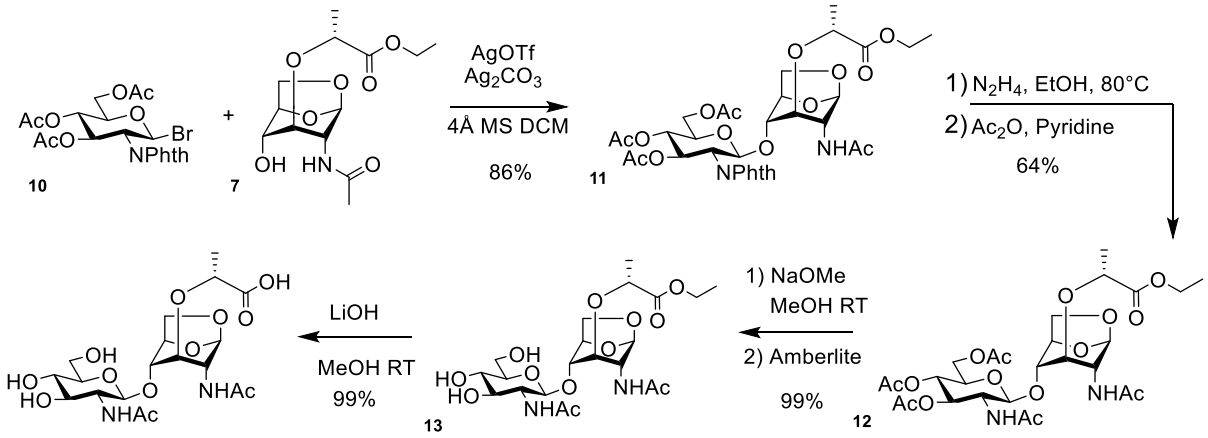

Scheme 2.2. Glycoside formation and deprotection of β-1,4-GlcNAc-anhydroMurNAc

Glycosylation of donor **10** via the Koenigs-Knorr reaction used a method that was adapted from Paulson et al.[78] in which I used silver triflate and silver carbonate in anhydrous methylene chloride to produce disaccharide **11** (Scheme 2.2). Hydrazine in

refluxing ethanol was used to remove the N-phthalimide protecting group and the resulting amine was directly acetylated using excess acetic anhydride in pyridine to furnish acetamide **12**. De-O-acetylation, followed by a final saponification step using lithium hydroxide in methanol yielded the target disaccharide (**14**) to which fluorophores may be appended.

Functionalization of BODIPY-Fl, previously prepared in the lab by Matthew Deen, with ethylenediamine allowed for direct amide coupling to disaccharide **14** (Scheme 2.3) using as a coupling reagent hexafluorophosphate benzotriazole tetramethyl uronium (HBTU) to yield candidate probe **15**.

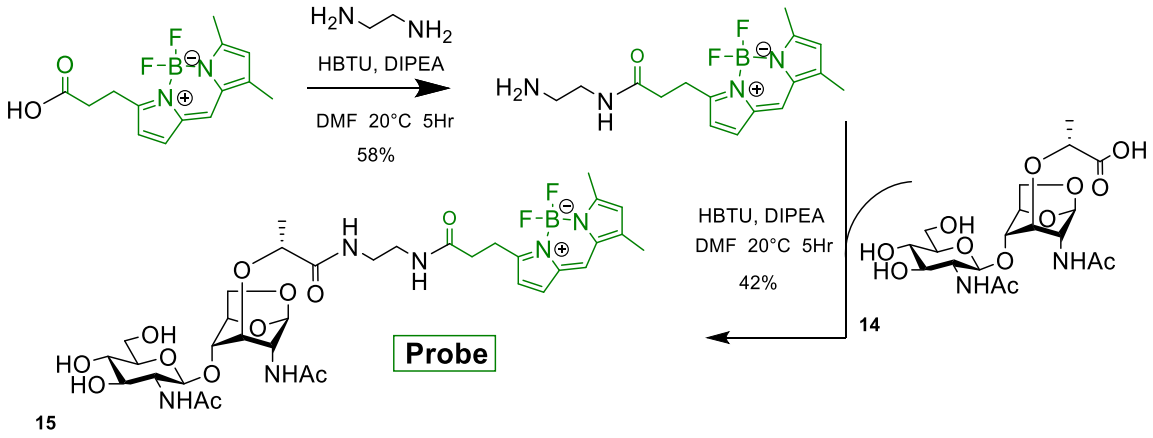

Scheme 2.3. Synthesis of β-1,4-GlcNAc-anhydroMurNAc-BODIPY-Fl

In parallel I worked to generate a caged coumarin using, as noted above, Pacifiic Blue. Initial attempts to cage Pacific Blue failed, presumably due to poor nucleophilicity of the acidic phenolic hydroxyl group. I suspected that the combined electron withdrawing effects of the adjacent fluorine atoms diminishes the nucleophilic potential of the phenolate. Techniques to drive the S_N2 reaction, such as preparation of the more reactive iodomethyl pivalate analogue (Scheme 2.4) and addition of 15-Crown-5 ether to enhance nucleophilicity of the phenolate failed to yield any product. Ultimately the Pacific Blue fluorophore was abandoned and the non-fluorinated commercially available version 7-hydroxycoumarin-3-carboxylic acid.

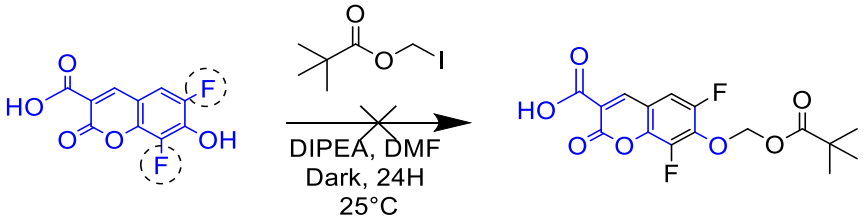

Scheme 2.4. Unsuccessful caging of Pacific Blue using iodomethyl pivalate

Initial attempts to selectively cage the 7-position hydroxyl group instead yielded preferential alkylation at the acid moiety or di-alkylation at both the acid and phenol positions (Scheme 2.5). It was hypothesized that dianion formation of the coumarin in the presence diisopropylethylamine (DIPEA) was electrostatically unfavorable. The propensity of the acid to be deprotonated before the phenol may well be the reason for its preferential alkylation. Administration of a stronger base , such as sodium hydride, was also ineffective in driving exclusive alkylation of the phenol.

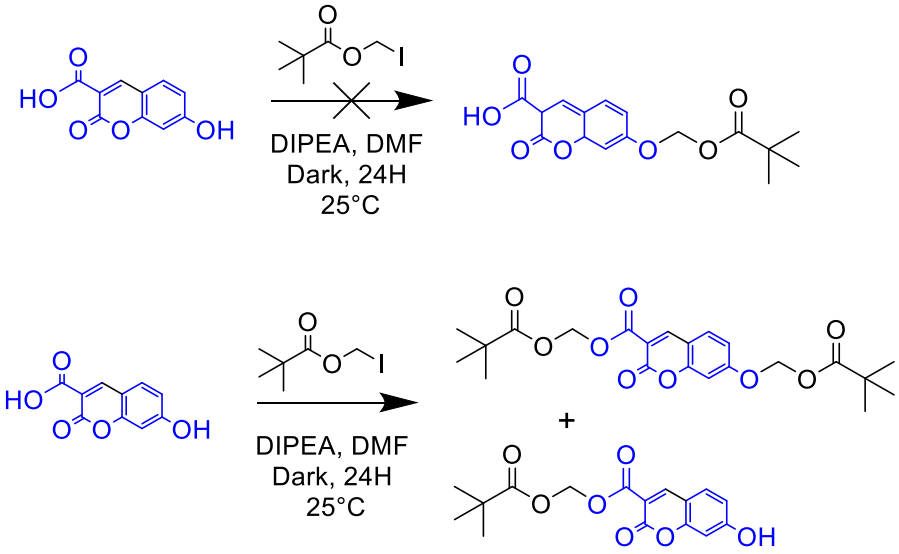

Scheme 2.5. Unsuccessful caging reactions of the non-fluorinated 7-Hydroxycoumarin-3-carboxylic acid

The synthesis was therefore reconfigured to neutralize the reactivity of the carboxy functional group by protection of the carboxyl group using benzyl 2-aminoethylcarbamate (Scheme 2.6). In addition to vastly improving solubility of the compound (previously only soluble in DMSO and DMF), subsequent installation of the methyloxypivalate caging group to generate acetal **16** was facile. Excitation and

emission of protected fluorophore **16** were monitored (Ex. 410 nm, Em. 450 nm) following uncaging in a solution of sodium hydroxide (pH 12).

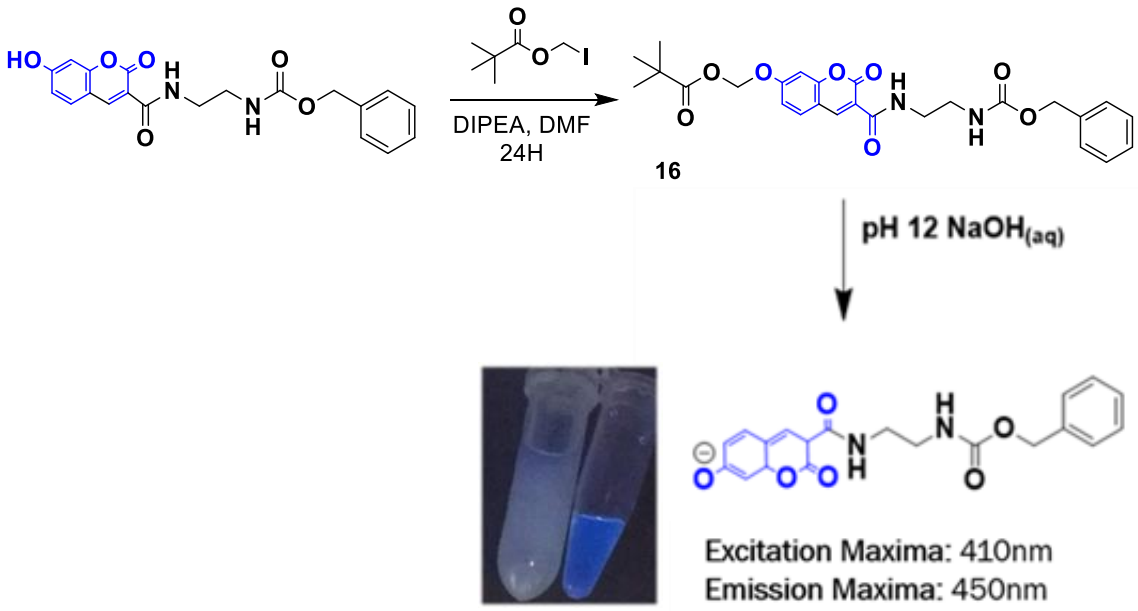

Figure 2.5. Methyl pivalate installation and experimental uncaging of acid protected 7-hydroxycoumarin-3-carboxylic acid
Incubation of the caged coumarin (**16**) in a basic solution of 0.1 M sodium hydroxide quickly liberates the fluorescent form of the molecule which glows bright blue under ultraviolent light compared to the intact starting material.

Incubation of compound **16** with cell lysates in spheroplast buffer (98% 0.8 M sucrose, 1% 1 M MgCl2, 1% 1 M Tris at pH 7.2 (v/v)) demonstrated a linear increase in fluorescence relative to whole cell spheroplasts as the negative control group. These data indicate successful uncaging of **16**, presumably as a result of cytosolic esterase activity.

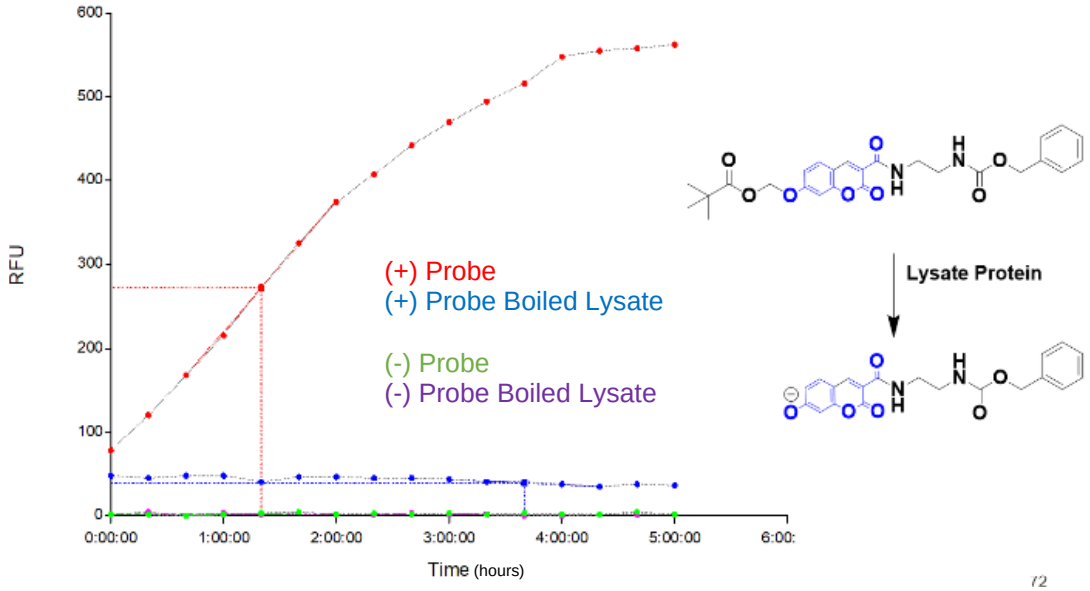

Figure 2.6. Successful cell lysate enzymatic cleavage of compound 16
Cell lysate boiled to induce protein denaturation prior to incubation with the probe (blue) shows no increase in fluorescence signal over time as compared to non-boiled lysate (red). Excitation and emission wavelengths used were 410nm and 450nm, respectively.

Having shown the successful fluorescence uncaging of model compound **16** using spheroplast lysates, I removed the carbamate protecting group to liberate the primary free amine for coupling to the disaccharide substrate (Scheme 2.7). Reduction conditions using standard palladium on charcoal caused saturation of the benzene ring, which I confirmed by mass spectrometry analysis. Experimentation with poisoned and moisten forms of palladium on charcoal using a hydrogen atmosphere failed to produce the desired compound. Ultimately 1,4-cyclohexadine was successfully applied as an alternative source of hydrogen, and this was done in refluxing ethanol in the presence of catalytic quantities of 10% by weight Pd-C, which furnished the target amine **17** (Scheme 2.7).

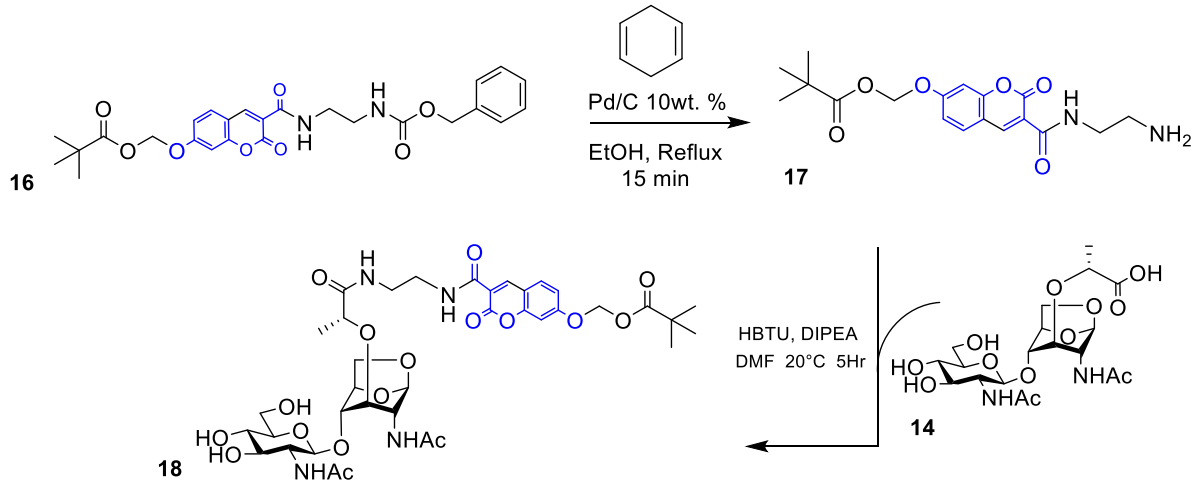

Scheme 2.7. Cyclohexadiene facilitated cage installation
1,4-cyclohexadiene allowed for the successful selective reduction of the carboxybenzyl group in **16** to liberate the free amine for subsequent amide coupling to furnish **18**.

Following HBTU amide coupling to disaccharide **14** caged candidate AmgG substrate **18** was obtained. The HPLC purified caged coumarin substrate, however, was observed to be unstable in solution – spontaneously uncaging to release fluorescent signal. Spontaneous colour change in the compound from a white solid, initially transparent in a solution of methanol, to a yellow solid consistent with uncaging, corresponded to an increase in fluorescence signal as observed by plate reader fluorescence detection. This decomposition occurred despite repeated HPLC purification and isolation in a number of buffered and unbuffered solutions in an effort to seek out the best conditions to minimize this problem (Figure 2.7). This observation was not entirely surprising given the low but detectable levels of hydrolysis reported even in the pivaloxymethyl ether coumarin substrate in similar aqueous conditions[77]. In the literature, incubation of similar acyloxymethylethers probes with enzymes produced significant increases in signal that are likely sufficient to render the spontaneous rates of hydrolysis a low-level background rate that can be ignored in those cases. As such, it was thought that the observed decomposition would not be a significant source of fluorescent signal.

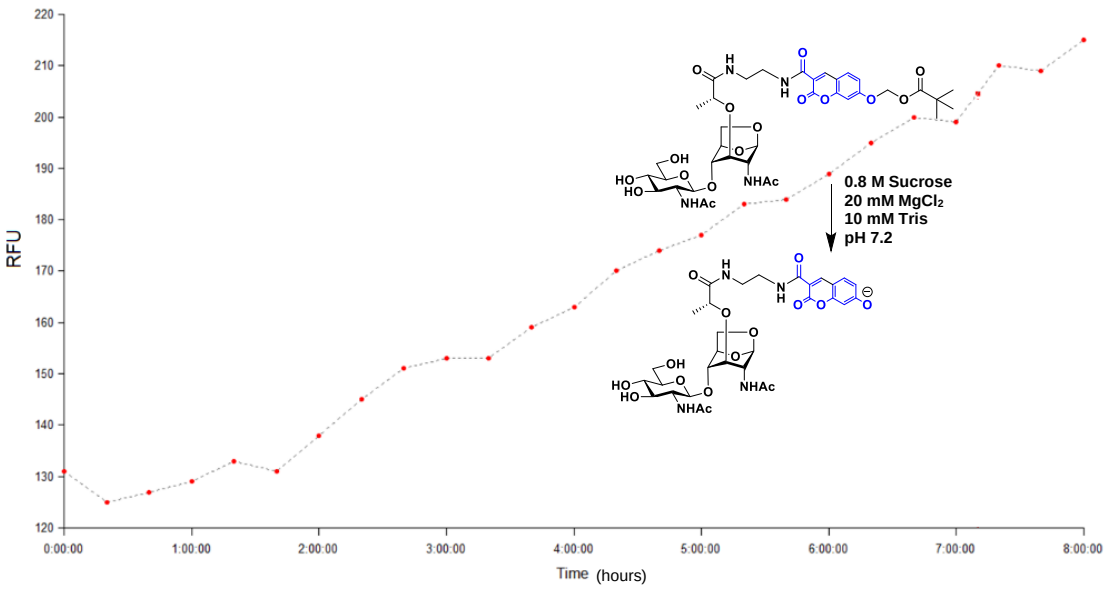

Figure 2.7. Spontaneous hydrolysis of compound 18 in aqueous buffer
Fluorescence activity was monitored via plate reader with 410nm and 450nm excitation and emission wavelengths, respectively.

To reproduce the existing results of the proof of concept assay by Perley-Robertson & Yadav[68] it was necessary to synthesize the same fluorogenic substrate. In this manner I could ensure that the spheroplasting procedure and execution of the assay protocol was not a source of error behind the results I was observing with new probes. As in the original synthesis, benzyl 2-aminoethylcarbamate was coupled to the acid moiety of disaccharide **14** to both introduce a spacer group in the substrate and provide a protected primary amine that could be obtained by reductive deprotection of compound **19**[68]. The resulting primary amine allowed for amide coupling to 10 mg of the commercially available N-hydroxy succinimidyl AlexaFluor-350 to generate probe **20** with 53 % yield following HPLC purification.

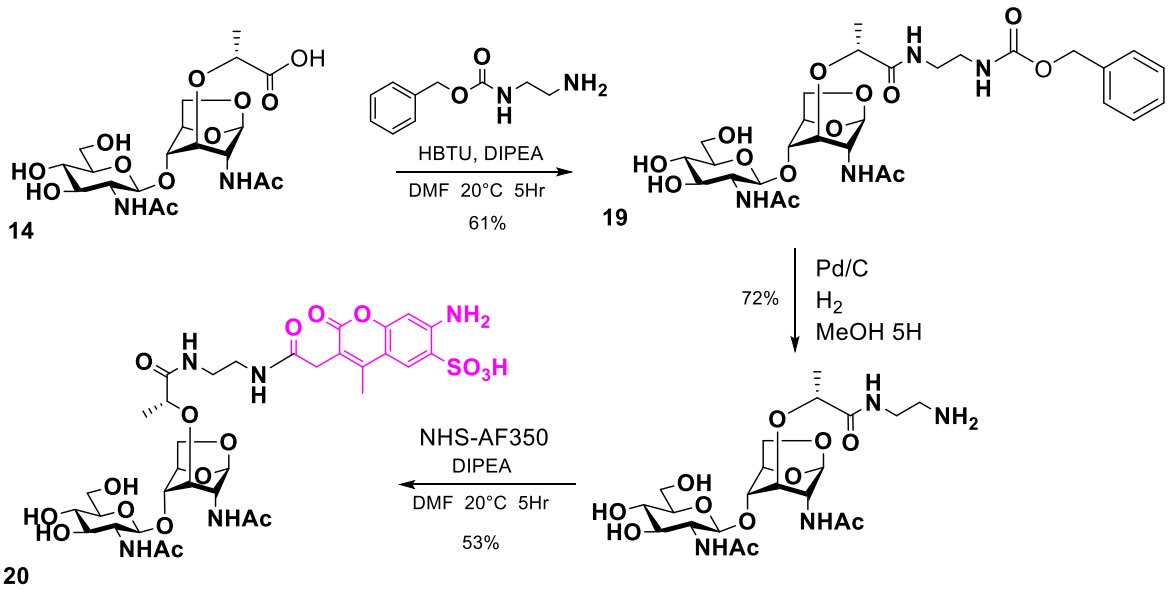

Scheme 2.8. Synthesis of β-1,4-GlcNAc-anhydroMurNAc-AF350

Preparation of spheroplasts using E. *coli* BW25113 and E. *coli* MG1655 was carried out according to previously published methods[82] that were optimized in the proof of concept transporter uptake assay[68]. DIC microscopy images taken before and after the spheroplasting process of E. *coli* show changes in the structure and mobility of bacteria (Figure 2.8) as they transition from motile rod-like cells to spheres that simply float in solution. Variability in the production of spheroplasts as judged by DIC microscopy was observed between experiments, with less than complete conversion of cells to spheroplasts. Apart from visual confirmation, spheroplast production could be confirmed by successful uptake of AmpG fluorescent probe as compared to unprocessed whole cells in the AmpG transport assay.

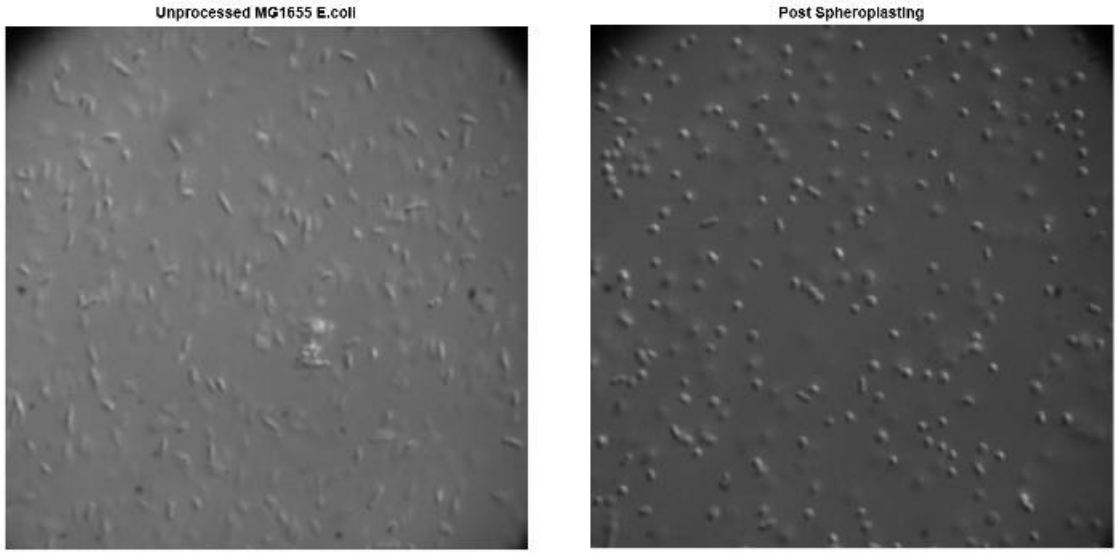

Figure 2.8. DIC images of *E. coli* MG1655 cells before and after spheroplasting
Prior to the addition of spheroplasting reagents, the bacteria are rod-like in shape and extremely mobile. Following transformation, they adopt a spherical form owing to the shedding of their rigid cell wall and become relatively fixed in place without the full use of their flagella.

2.4.5. Reproducing AmpG Transport Assay Proof of Concept

Having prepared several probes and having learned to produce spheroplasted cells, a fluorescent uptake assay using a fluorescent plate reader was performed according to the previously established protocol[68]. Incubation of cells with probe **20**, followed by washing of the spheroplasts to remove extracellular signal furnished significantly higher fluorescence in cells containing the AmpG transporter as compared with the ΔAmpG genetic knock-out strain (Figure 2.9). This result was indicative of the successful internalization and retention of fluorescent substrate **20**, suggesting that the core disaccharide substrate (**14**) had been correctly synthesized and that the spheroplasting process and transporter assay were being accurately performed. Similar results were observed in using the new BODIPY-Fl probe (**15**), signaling that the alternative fluorophore was well tolerated by the AmpG transporter and similarly taken up by spheroplasted cells.

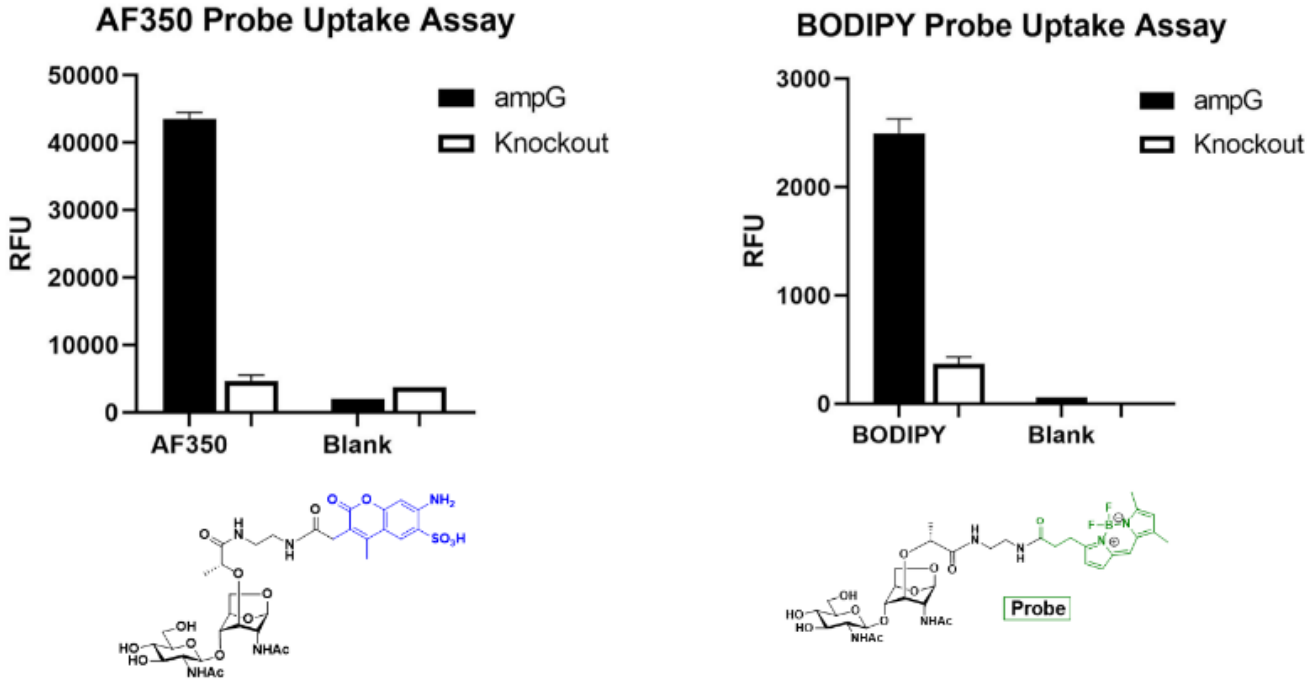

Figure 2.9. Successful uptake of fluorescent probes 15 (BODIPY-FL) and 20 (AF350) following incubation and washes
Experiments were carried out in duplicate (N=2). All probes were incubated at 50 μM concentration levels in 0.12 g / mL E. coli for 2 hours before 4 cycles of centrifugation, pellet washing, and resuspension preceding fluorescent plate reader analysis.

Access to a Zeiss AxioObserver spinning disc confocal microscope with a 491nm excitation laser allowed for suitable imaging of the comparatively red-shifted BODIPY-Fl probe (**15**). Concentrated fluorescent signal was observed to be emitted directly from spheroplasts with zero observable signal in the ΔAmpG genetic knockdown strain (Figure 2.10). These data supported the notion that signal observed in the microplate reader was from the AmpG mediated internalization of the probe.

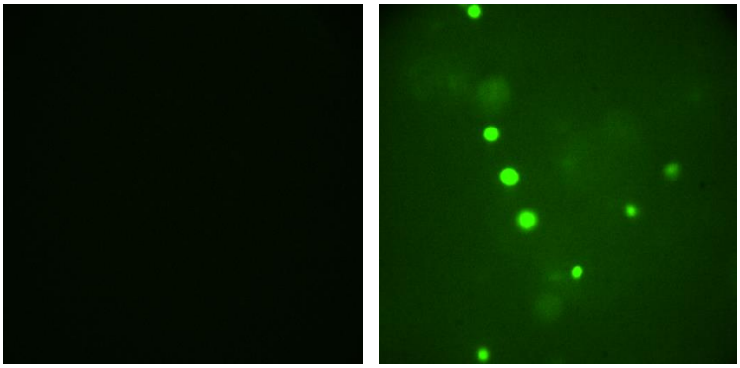

Figure 2.10. Fluorescence microscopy confirming uptake of BODIPY-Fl transport substrate 15 (right) in ampG cells and absence of signal in AmpG knockout cells (left)
Excitation and emission wavelengths 491nm and 503nm, respectively.

Pursuing the approach of using an impermeable fluorophore, I performed initial experiments attempting to entirely quench the constitutive fluorescence of BODIPY-Fl. To this end, a two-fold dilution series of Ponceau S (10 mM–156 μM) was dissolved in 50 μM of BODIPY-Fl probe **15** in spheroplast buffer conditions. Concentrations achieving greater than 90% quenching efficiency however proved to overwhelm any signal potentially released during incubation of BODIPY-Fl based **15** in spheroplasts. This observed inner filtering effect stemming for the high concentration of FRET donor molecules required to suppress the intense brightness of BODIPY-Fl (quantum yield Φ = 0.9, EC > 80,000 $cm^{-1} M^{-1}$) made this strategy untenable. Substitution with Pacific Blue as a dimmer fluorophore was more promising but this required exceedingly high concentrations of a polyanionic FRET acceptor such as Ponceau S (Figure 2.11) to extinguish fluorescence from Pacific Blue led to a maximum quenching of approximately 90% as compared to the fluorescence seen in the absence of the quencher. The inability to effectively quench fluorescence by essentially saturating the solution using FRET acceptor molecules detracted from this as potential assay strategy.

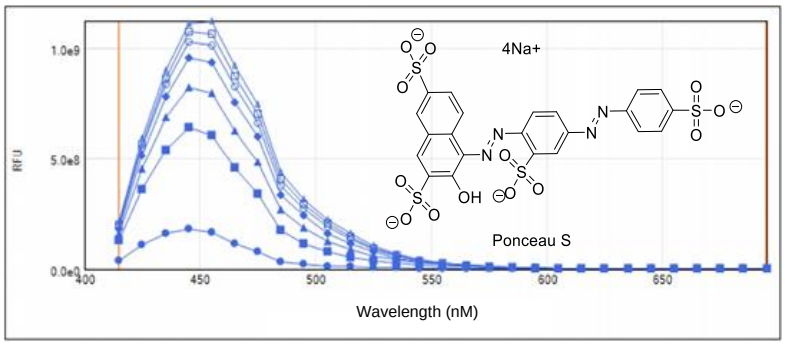

Figure 2.11. Quenching of fluorophore Pacific Blue using Ponceau S as a FRET acceptor
Excitation and emission wavelengths 410nm and 455nm, respectively. Ponceau S FRET acceptor concentration ranged from 10 mM to 156 µM.

2.4.6. Caged Coumarin Transport Assay

Having successfully replicated the results of previously established work[68] to ensure the functionality of the assay and structural integrity of the carbohydrate recognition features of the substrate, the caged coumarin probe (**18**) was tested for uptake by AmpG using *E. coli* MG1655 spheroplasts using the previously established protocol[68]. Fluorescence data obtained using a microplate reader (Figure 2.11) appears to show a 4 to 5-fold increase in fluorescence of the AmpG transporter containing cells as compared to the ΔAmpG genetic knockdown strain, indicative of a weaker internalization or retention ability for probe **18** or the hydrolyzed form as compared to the AF-350 (**15**) and BODIPY-Fl (**20**) counterparts (Figure 2.12). It also remained unknown whether the caged probe was being transported by AmpG rather than the uncaged fluorescent species. Indeed, retention of signal in AmpG cells following washing could be attributed to extracellular uncaging followed by internalization of the anionic fluorescent compound, rather than internalization of the intact caged compound. Difference in polarity between the alkylated and free anion form of the compound may dictate substrate tolerability. The sulfonic acid group present in the AF-350 compound **20** lends credit to this notion that polar functional groups may assist with internalization via AmpG, whereas the pivaloxymethyl ether may be less favoured for transport.

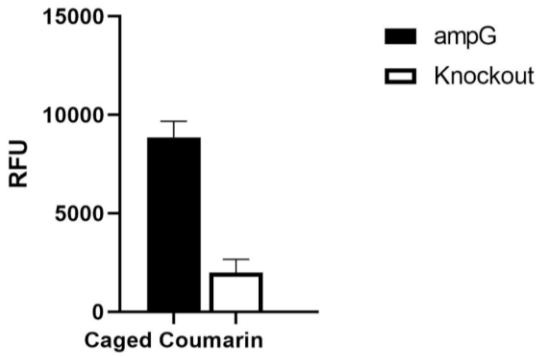

Figure 2.12 Caged Coumarin (18) spheroplast uptake assay following washing

Microscopic images obtained by the Zeiss AxioObserver using the DAPI-based fluorescent channel allowed for visualization of fluorescence of compound **20** within spheroplasts after washing (Figure 2.13). Comparison of these images with DIC images of the same field of view seem to suggestion a failure of the probe to be internalized by the spheroplasts.

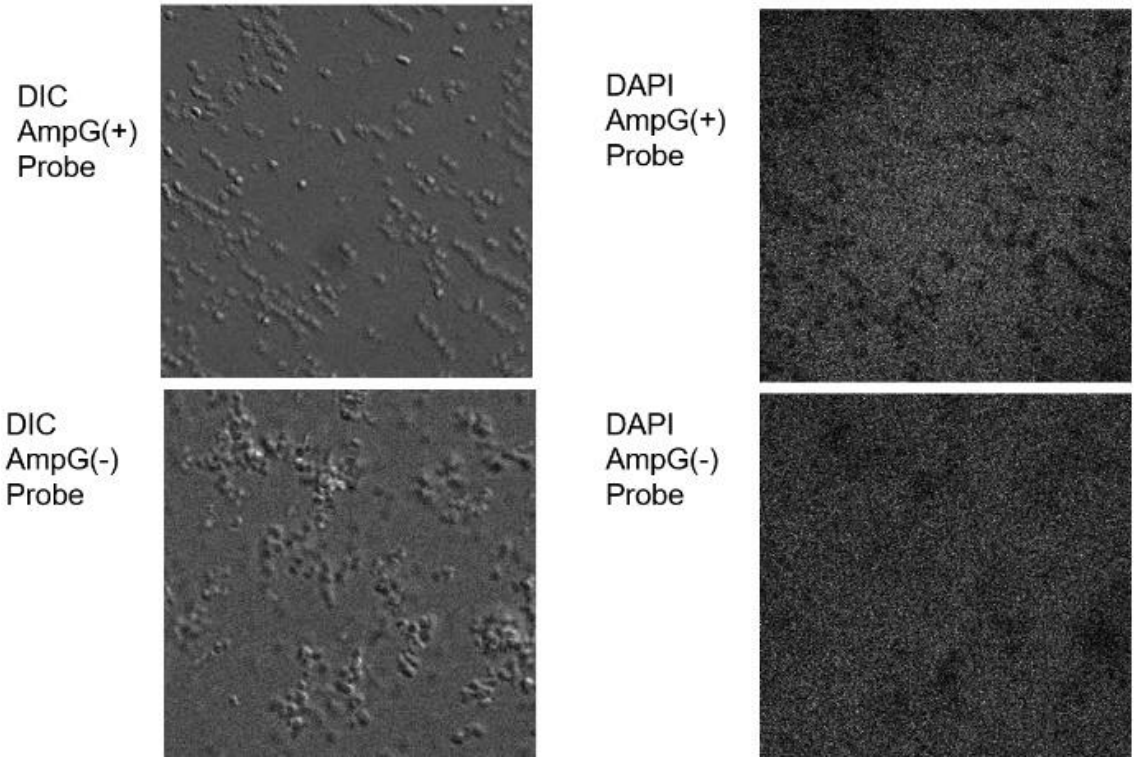

Figure 2.13. Fluorescence microscopy images of caged coumarin (18) compared to DIC

Initial attempts to monitor fluorescence uncaging in spheroplasts highlighted the need to carry out the assay immediately following purification of compound **18**. Despite using identical probe concentrations across all wells, the solutions emitting the strongest signal were found in the negative control buffers lacking spheroplasts. This presumably was due to the interference of spheroplasts themselves, causing light scattering, in conjunction with existing uncaged fluorescence due to spontaneous uncaging of the probe during the handling and storage of compound **20**. Subsequent experiments were carried out immediately following HPLC purification to mitigate these possible problems.

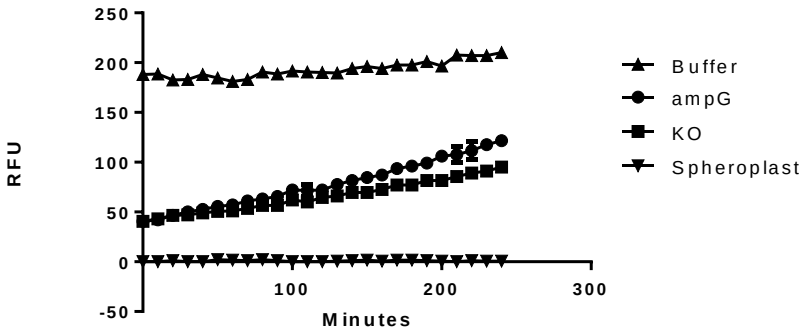

Figure 2.14. Probe 18 in buffer unhindered by scattering effects of spheroplasts shows greater signal than spheroplast incubated probe

Monitoring by plate reader the fluorescence over time directly following incubation in spheroplasts using freshly HPLC purified probe (**18**) did seem to yield a greater difference in signal increase between the experimental and control spheroplasts. Efficient internalization and cytosolic turnover of **18** was expected to yield results similar to those observed in the cell lysate assay when using precursor compound **16**. In contrast, there was only an approximately 2-fold difference in rates between AmpG containing spheroplasts and the ΔAmpG genetic knockdown strain (Figure 2.15). Large background signal from spontaneous uncaging of compound **20** in buffer therefore likely accounts for a significant portion of signal release.

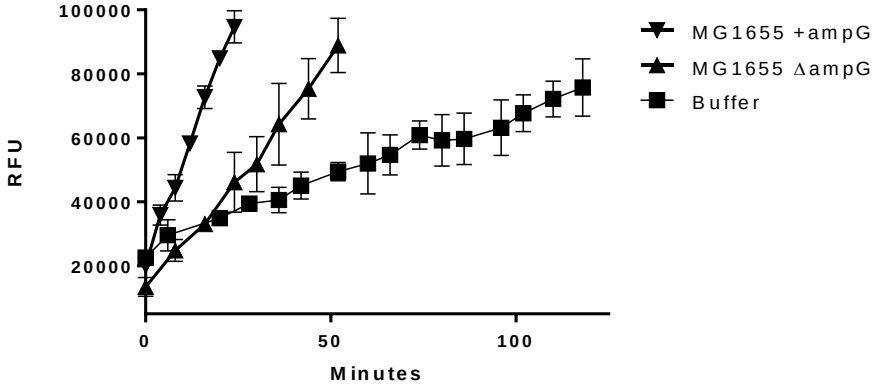

Figure 2.15. Spheroplast uptake assay using compound 18 immediately following HPLC purification showing increased fluorescence uncaging in ampG cells as measured by fluorescence using a plate reader

Given the greater than 10-fold increase in signal arising from uncaging of compound **16** in cell lysate experiments relative to the buffered negative control, it seemed plausible that only low levels of **18** were being turned over inside spheroplasts. It was uncertain whether this could be attributed to poor internalization of the uncaged probe or poor cytosolic turnover inside of cells. Lack of confidence in uptake of **20** by AmpG in spheroplasts and overall instability in aqueous conditions inspired the search for an alternative caging strategy.

2.4.7. Design of AMC Amidase Approach

As opposed to the ester caging strategy described above that I pursued, amides are much more stable and, if attached as an amino acid, also more closely resemble the natural substate peptide chain of AmpG substrates. Although fluorescence is not entirely quenched upon caging of aminocoumarins as amides, it is sufficiently altered such that liberation of the free aryl amine would be easily observable by fluorescence spectroscopy[83].

Previously published work demonstrated the use of 7-amino-4-methylcoumarin (AMC) substrates for the detection *E. coli* methionine amino peptidase (MAP) activity[84]. It is thought that *E. coli* possess only one methionine amino peptidase[85]. This enzyme is localized to the cytosol[86], rather than periplasm, and presumably would remain inside the cell following spheroplasting. The scientific literature reports on the selectivity of *E. coli*

MAP for terminal methionine residues, with a preference for small side chain residues immediately adjacent to the terminal methionine[87]. This limited preference in adjacent residues was consistent with crystal structure data of the enzyme-substrate complex depicting outward branching of the remaining residues away from the active site. As a result, it was hypothesized that that a GlcNAc-anhydro-MurNAc disaccharide appended to a methionine caged coumarin may be distal enough to not interfere with cleavage of the methionine from the probe by the MAP. The two predominant methionine uptake systems in *E. coli*[88,89] posed potential problems since, if they facilitated transport of the disaccharide substrate, this could interfere with the assay of AmpG transport activity. This concern was mitigated by the fact that no uptake was observed of the methionine AMC probe[84] in whole cell *E. coli*[84]. Furthermore, uptake of the probe via the methionine transport system, if problematic, could be inhibited by incubation of the spheroplasts in buffers containing concentrated methionine.

Existing experiments employing this methionine AMC approach used EDTA among other chelators of divalent cations to inhibit peptidase activity[84]. The fragile state of spheroplasts precludes the use of these inhibitors due to their propensity for lysis.

2.4.8. Synthesis of Methionine Caged Substrate

Commercially available fluorenyl methyloxy carbonyl (Fmoc) protected L-methionine was converted to the corresponding acyl chloride using thionyl chloride in refluxing DMF. Displacement of the chloride with 7-amino-4-methyl-3-coumarinylacetic acid was carried out using diisopropylethylamine as a base in DMF . Amide coupling to the disaccharide (**14**) followed by deprotection of the Fmoc group in a 20% solution of piperidine in DMF furnished the final target compound **21**.

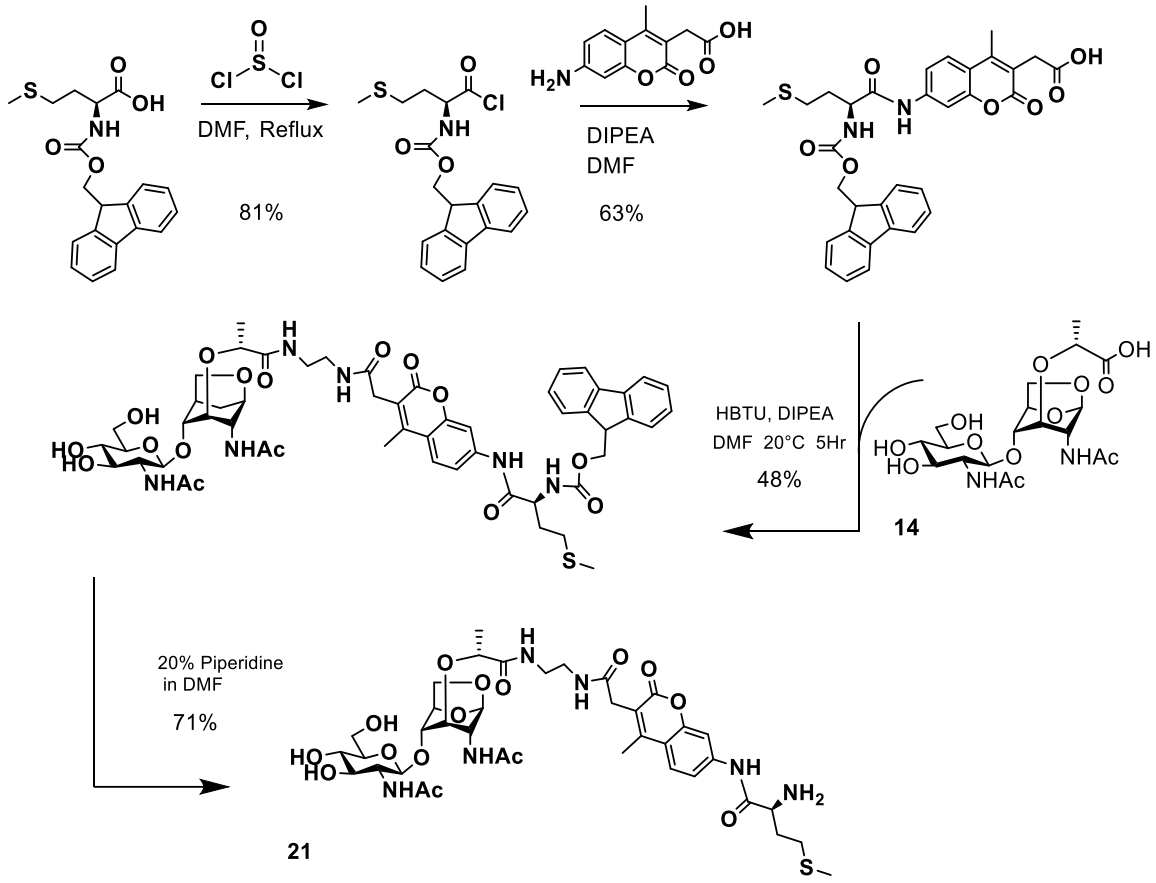

Scheme 2.6. Synthesis of methionine amide caged analogue β-1,4-GlcNAc-anhydroMurNAc-methionine-aminomethylcoumarin (21)

2.4.9. Methionine Caged Coumarin Transport Assay

Initial testing was carried out using cell lysates to ensure cytoplasmic methionine aminopeptidase (MAP) activity was capable of turning over the novel substrate. An approximate tenfold increase in signal was observed relative to the negative control after thirty minutes of incubation. These results indicated that cytoplasmic MAP activity was capable of cleaving the substrate target amide bond, but that there was no extracellular enzyme that was appreciably turning over the substrate.

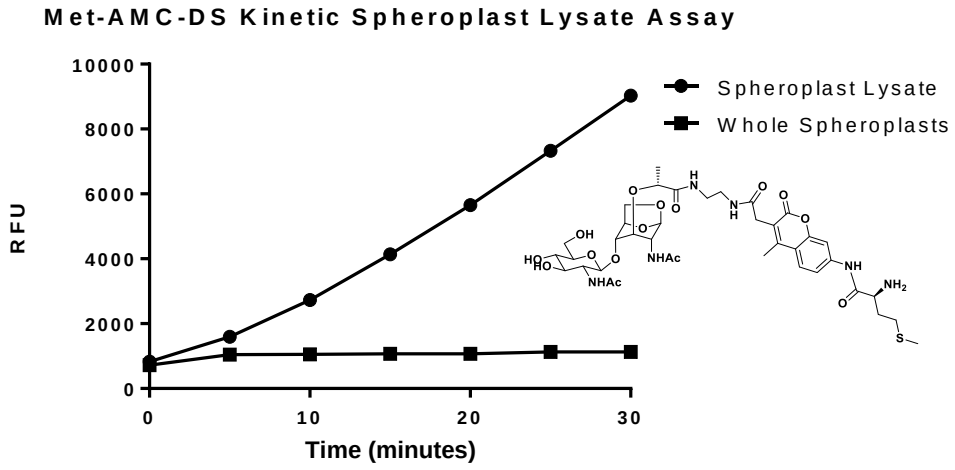

Figure 2.16. Spheroplast lysate assay shows uncaging of compound 21

Despite promising cell lysate experiment data, endpoint scans following the wash protocol suggest a complete inability of the probe to be taken up by cells (Figure 2.17). The stability against spontaneous hydrolysis of **21** combined with the signal retention observed for the ester caged analogue (**18**) would suggest that only the uncaged MAP-processed probe is capable of being internalized. Kinetic monitoring of compound **21** incubated with spheroplasts yielded no significant difference in signal between AmpG containing spheroplasts as compared to ΔAmpG spheroplasts.

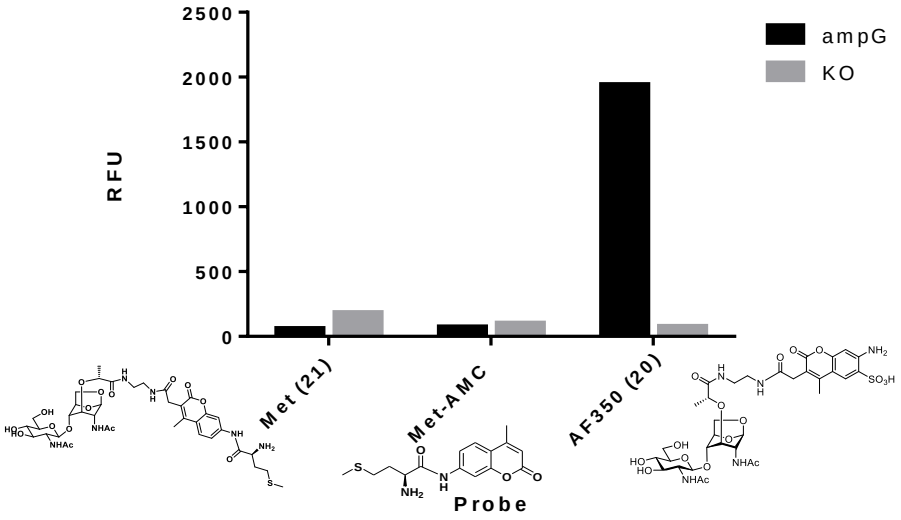

Figure 2.17. Methionine caged probe (21) shows no uptake in AmpG spheroplasts following uptake assay incubation and washing

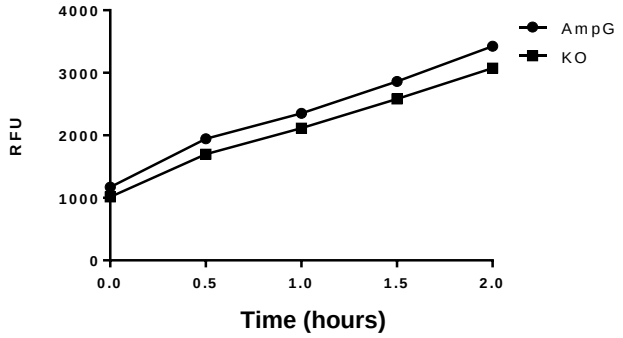

Figure 2.18, Methionine caged probe (21) shows no difference in fluorescence signal between AmpG spheroplasts and knockout strain during uptake assay

The automatic gain function of the microplate reader used to obtain the fluorescence data serves to amplify the signal readout and adjust the y-axis correspondingly. The 4-fold increase in signal observed over 2 hours would indicate an extremely low baseline signal. To confirm this notion, a positive control consisting of equimolar concentrations of the methionine-caged coumarin free of the disaccharide was tested alongside probe **21** in spheroplasts. Signal produced from turnover of this coumarin rapidly dwarfed any signal produced from compound **21** in either cell line.

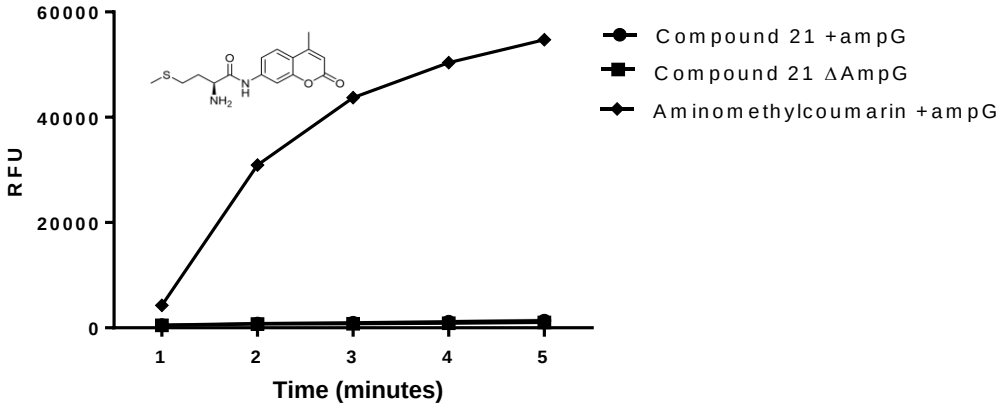

Figure 2.19. Methionine aminomethylcoumarin incubate with spheroplasts shows dramatic signal release relative to methionine amide caged coumarin (21)

2.4.10. Alternative Amide Caging Residue Strategy

These results suggested a failure of compound **21** to be appreciably internalized by cells. Mass spectrometry results confirmed the expected mass of **21** following

completion of the synthesis, as with all preceding probes used in the uptake assay. A secondary mass spectrometry analysis of stock compound **21** dissolved in DMSO used in the assay revealed a primary peak with an additional 16 atomic mass units. This value corresponded exactly to the atomic mass of oxygen and is believed to arise by oxidation of the sulfur atom of methionine. While it seemed unlikely that this modification would be responsible for the inability of **21** to be internalized by AmpG transport, two additional analogous probes were synthesized using L-alanine and L-leucine as caging moieties in place of methionine (Figure 2.20). The synthetic route was exactly as in the production **21** with the exception of using N-Fmoc-L-alanine and N-Fmoc-L-leucine as starting materials.

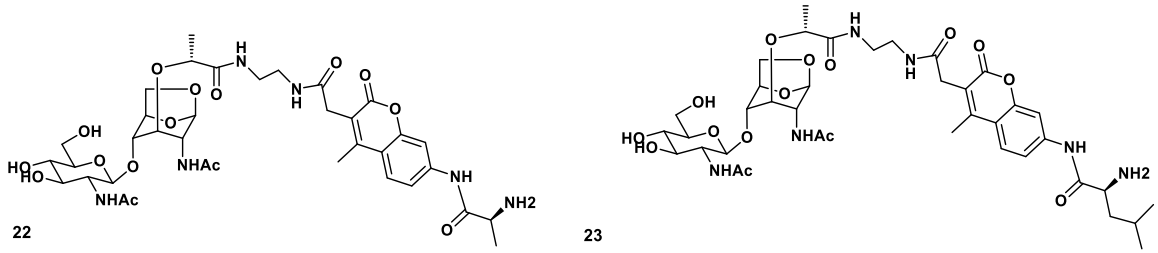

Figure 2.20. L-Alanine amide caged coumarin (22) and L-leucine amide caged coumarin (23)

Spheroplast lysate experiments were able to confirm ability of cytosolic contents to cleave off the alanine and leucine caging moieties. Uncaging was extremely rapid, reaching detector saturation within minutes of incubation.

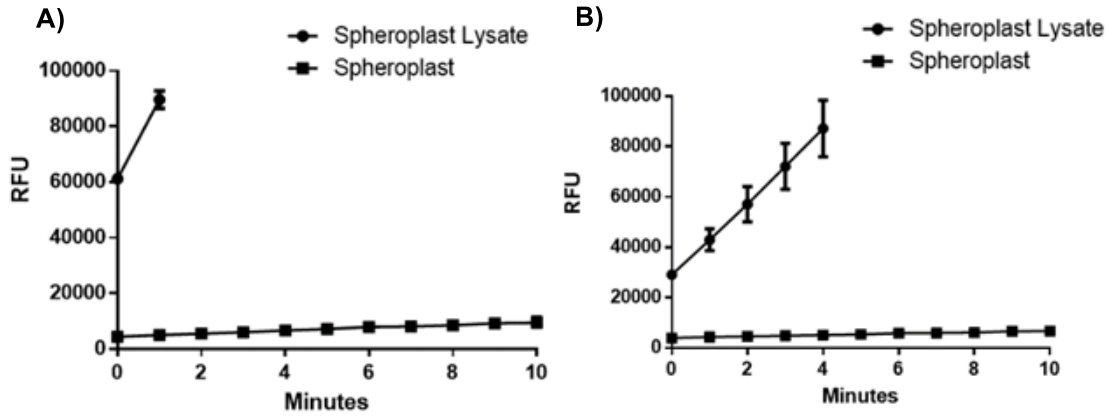

Figure 2.21. Spheroplast lysate shows rapid uncaging of alanine probe 22 (A) and leucine probe 23 (B)

Endpoint scans of cells incubated with either probe **22** or **23** both exhibited some level of retention in AmpG-containing cell lines. It is suspected that this difference in signal is the result of uptake of the uncaged fluorescent probe following the rapid extracellular amidase activity of lysed spheroplasts. This may explain the discrepancy in results between endpoint scans of probes **22** and **23** as compared with the methionine analog **21** (Figure 2.22).

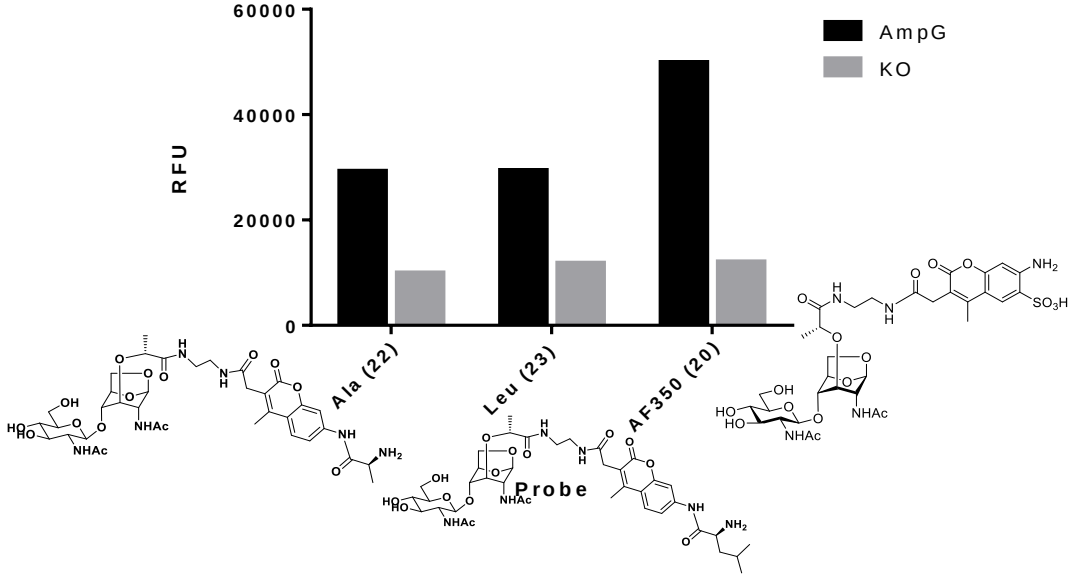

Figure 2.22. Fluorescence signal of alanine (22) and leucine (23) probe in spheroplast uptake assay following washing

Despite turnover of the probes in the cell lysate assays, as with the methionine probe **21**, there was no substantial difference in release signal observed during incubation between AmpG and ΔAmpG cell lines (Figure 2.23).

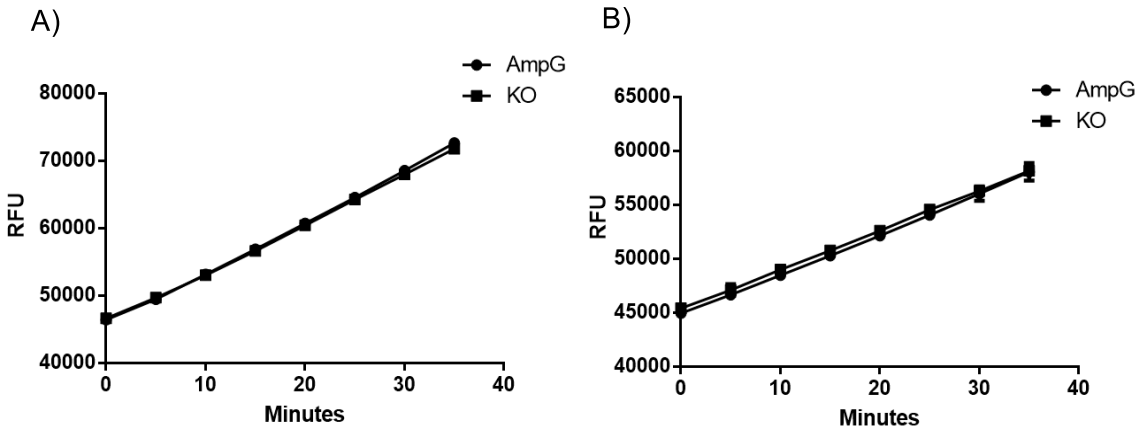

Figure 2.23. No difference in fluorescence uncaging observed between +AmpG and knockout line in spheroplasts for probes 22 (A) and 23 (B)

2.5. Conclusions and Future Work

Several probes have been designed and synthesized in an effort to develop an efficient and high throughput amenable screening assay toward identifying inhibitors of AmpG permease. These probes, while capable of being processed by the lysates of *E. coli* spheroplasts, have nonetheless shown to be ineffective in quantifying AmpG transporter activity in the manner intended. Despite the retention of fluorescent signal in AmpG transporter bearing cells, it has not been shown that AmpG permease is capable of internalizing these probes in their intact and chemically caged state. Furthermore, instability of the POM caging group of compound **18** introduced a significant level of background noise due to the high rate of spontaneous uncaging in aqueous conditions. All probes were synthesized using an identical stock of the core disaccharide substrate structure, including that of the successfully reproduced AF-350 based positive control **21**. Taken together these data would suggest an inability of the caged novel probes to be transported inside of spheroplasts and potentially a lower substrate tolerability than was previously hypothesized for the AmpG transporter.

A shift in quenching strategies to enable eliminating manual washing, resuspension, and centrifugation of spheroplasts could ultimately achieve the same goal. One alternative approach could be to use cell impermeable thioamide compounds to quench the extracellular signal of BODIPY-Fl (18) by photoinduced electron transfer (PET) quenching without simultaneously extinguishing all signal from within the solution due to an inner filter effect. Alternatively, mechanical improvements and setup

optimization in the washing, suspension, and draining capabilities of the high throughput screening platform may even be capable of using the original assay protocol to screen for inhibitors.

2.6. Experimental Section

2.6.1. General Chemical Methods

Unless stated otherwise, all reagents were purchased from commercial sources and were used without further purification. Anhydrous solvents used in reactions were purchased from commercial sources. Reactions were monitored by thin layer chromatography (TLC) on Silica Aluminum TLC plate, silica gel coated with fluorescent indicator F254. TLC spots were detected under UV light (254 λ /365 λ) and/or by charring with potassium permanganate or “Seebach” stain (2.5 g phosphomolybdic acid, 1 g Ce(SO4)2, 6 mL conc H2SO4, 94 ml H2O.). High pressure liquid chromatography (HPLC) was performed on an Agilent 1260 Infinity device equipped with a variable wavelength UV-Vis detector using ZORBAX 300SB C8 column (5.0 µm, 9.4 x 250 mm for analytical runs and semi-preparative scale purifications) and elution carried out using HPLC grade solvents. In concentrating reactions, solvents were evaporated under reduced pressure on a rotary evaporator between 40–60 ºC using either a PIAB vacuum system or Welch W Series high vacuum oil pump. NMR spectra were recorded on Bruker AVANCE III 400 or AVANCE II 600_QNP. Spectra are referenced according to the chemical shift of the deuterated solvent in which they were dissolved (^{1}H NMR: $CDCl_3$: 7.26 ppm, CD_3OD: 3.30 ppm; ^{13}C NMR: $CDCl_3$: 77.0 ppm; CD_3OD 49.0 ppm) and peak assignments were made on the basis of 2D-NMR (^{1}H COSY, HSQC, HMBC) experiments. High resolution mass spectra (HRMS) were recorded on a Bruker MaXis Impact spectrometers using positive or negative electrospray ionization (ESI).

2.6.2. Synthesis of Key Chemical Compounds

β-D-N-Acetylglucopyranosyl-1,6-anhydro-β-D-N-acetylmuranamide (**14**) To a solution of 17.9 mg (0.028 mmol) of compound **13** (ethyl (R)-2-(((1R,2S,3R,4R,5R)-4-acetamido-2-(((2S,3R,4R,5S,6R)-3-acetamido-4,5-dihydroxy-6-(hydroxymethyl)tetrahydro-2H-pyran-2-yl)oxy)-6,8-dioxabicyclo[3.2.1]octan-3-yl)oxy)propanoate in 566 µL of methanol was added 566 µl of 1.0M LiOH (0.057 mmol)

and stirred under an inert atmosphere at room temperature for 30 minutes. The crude mixture was then concentrated by rotary evaporation and purified using a CombiFlash™ chromatography device on normal phase silica to give compound **14** (11.4 mg, 85% yield). ^{1}H NMR (600 MHz, Deuterium Oxide) δ 5.25 (t, *J* = 1.6 Hz, 1H), 4.73 (s, 2H), 4.52 (dd, *J* = 7.4, 3.9 Hz, 2H), 4.11 – 4.04 (m, 2H), 3.92 (d, *J* = 1.7 Hz, 1H), 3.85 (d, *J* = 1.9 Hz, 1H), 3.77 (dd, *J* = 12.5, 2.1 Hz, 1H), 3.67 – 3.58 (m, 4H), 3.57 (d, *J* = 2.6 Hz, 2H), 3.43 (dd, *J* = 10.5, 8.4 Hz, 1H), 3.39 (t, *J* = 1.6 Hz, 1H), 3.37 – 3.27 (m, 2H), 3.21 (d, *J* = 0.7 Hz, 1H), 1.93 (dd, *J* = 7.3, 0.7 Hz, 6H), 1.21 (d, *J* = 6.9 Hz, 3H).^{13}C NMR (151 MHz, Deuterium Oxide) δ 175.15, 100.85, 99.72, 76.11, 75.91, 75.34, 73.71, 73.62, 73.23, 69.58, 69.48, 64.69, 60.34, 60.24, 55.41, 50.17, 22.16, 21.86, 18.11. Mass Spec: HR-ESI-MS calculated for $C_{19}H_{30}N_2O_{12}$ [M+H]+ 479.1889, found 479.1868

β-D-N-Acetylglucopyranosyl-1,6-anhydro-β-D-N-acetylmuranamide BODIPY-Fl (**15**) To a solution of 5.9 mg (0.018 mmol) of N-(2-aminoethyl)-3-(5,5-difluoro-7,9-dimethyl-5H-dipyrrolodiazaborinin-3-yl)propenamide dissolved in 720 µL of DMF (0.025 M) was added 10.6 mg of HBTU (0.028 mmol) and DIPEA (11.3 µl, 0.065 mmol) and stirred under an inert atmosphere at room temperature for two hours. The mixture was then concentrated by rotary evaporation and purified using a CombiFlash™ chromatography device on normal phase silica to give compound **15** (3.2 mg, 22% yield). ^{1}H NMR (600 MHz, Methanol-d_4) δ 7.45 (d, *J* = 253.4 Hz, 1H), 7.03 (dt, *J* = 171.0, 4.7, 4.0 Hz, 1H), 6.98 (s, 0H), 6.35 (d, *J* = 4.0 Hz, 1H), 6.24 (s, 1H), 4.61 (d, *J* = 5.5 Hz, 1H), 4.50 (d, *J* = 8.3 Hz, 1H), 4.25 – 4.20 (m, 1H), 4.12 (q, *J* = 6.7 Hz, 1H), 4.01 (d, *J* = 1.8 Hz, 1H), 3.91 (dd, *J* = 12.0, 2.1 Hz, 1H), 3.85 (d, *J* = 1.9 Hz, 1H), 3.81 – 3.66 (m, 3H), 3.52 (p, *J* = 1.6 Hz, 1H), 3.48 – 3.27 (m, 27H), 3.24 (t, *J* = 7.8 Hz, 2H), 2.64 (ddd, *J* = 9.0, 6.7, 1.2 Hz, 2H), 2.54 (s, 3H), 2.31 (s, 3H), 2.05 (d, *J* = 18.4 Hz, 6H), 1.38 (d, *J* = 6.8 Hz, 3H), 1.31 (s, 1H). ^{13}C NMR (151 MHz, Methanol-d_4) δ 174.62, 173.59, 173.40, 171.98, 159.81, 157.24, 144.34, 135.09, 133.50, 128.26, 124.38, 119.89, 116.28, 100.58, 100.51, 78.06, 76.81, 76.04, 73.97, 73.85, 73.26, 70.59, 64.44, 61.22, 55.70, 48.38, 38.61, 38.39, 34.65, 24.13, 22.01, 21.23, 17.45, 13.50, 9.78. Mass Spec: HR-ESI-MS calculated for $C_{35}H_{49}BF_2N_6O_{12}$ [M+H]+ 795.3560, found 795.3549

β-D-N-Acetylglucopyranosyl-1,6-anhydro-β-D-N-acetylmuranamide Pivaloxymethyl Ether Coumarin (18). Crude compound **17** (11 mg, 0.030 mmol) was dissolved in 912 µL of DMF (0.033 M) with 23.2 mg (0.043 mmol) of compound 14, 23.9 mg of HBTU (0.063 mmol) and 12.6 µl of DIPEA (0.072 mmol) and stirred for 2 hours

under an inert atmosphere at room temperature. The mixture was then concentrated by rotary evaporation and purified using a CombiFlash™ chromatography device on normal phase silica followed by HPLC purification to give compound **18** (2.0 mg, 0.002 mmol, 12.5% yield). 1H NMR (600 MHz, Methanol-d4) δ 7.83 (d, J = 8.6 Hz, 1H), 7.19 – 7.13 (m, 2H), 5.94 (d, J = 0.8 Hz, 2H), 4.59 (d, J = 5.6 Hz, 1H), 4.48 (d, J = 8.4 Hz, 1H), 4.21 (dd, J = 7.5, 0.9 Hz, 1H), 4.13 (q, J = 6.7 Hz, 1H), 3.88 (dd, J = 12.0, 2.0 Hz, 1H), 3.81 – 3.57 (m, 6H), 3.51 (p, J = 1.5 Hz, 1H), 3.47 – 3.35 (m, 4H), 3.33 – 3.25 (m, 56H), 2.04 (s, 3H), 1.98 (s, 3H), 1.36 (d, J = 6.7 Hz, 3H), 1.21 (s, 9H). 13C NMR (151 MHz, Methanol-d4) δ 179.02, 176.78, 174.76, 173.40, 171.86, 163.04, 161.76, 161.04, 156.21, 147.71, 131.41, 115.47, 114.12, 113.62, 102.36, 100.67, 100.51, 84.29, 78.04, 76.77, 76.00, 73.96 (d, J = 2.0 Hz), 73.33, 70.53, 64.41, 61.19, 55.68, 38.77, 38.52, 38.11, 31.69, 29.55 – 29.28 (m), 25.82, 22.35, 22.01, 21.19, 17.31. Mass Spec: HR-ESI-MS calculated for $C_{37}H_{50}N_4O_{17}$ [M+H]+ 823.3261, found 823.3233

β-D-N-Acetylglucopyranosyl-1,6-anhydro-β-D-N-acetylmuranamide AF350 (20) To a solution of 5.0 mg (0.012 mmol) of commercially available AF350 N-hydroxysuccinimidyl ester dissolved in 1.0 ml of DMF was added 9.1 mg of compound 19 (0.018 mmol) and 3.3 µl of DIPEA (0.019 mmol) and stirred at room temperature under an inert atmosphere for two hours. The crude reaction mixture was then concentrated by rotary evaporation and purified using a CombiFlash™ chromatography device on normal phase silica followed by HPLC purification to give compound **20** (5.6 mg, 57% yield). ^{1}H NMR (400 MHz, Methanol-d_4) δ 8.16 (s, 1H), 5.31 (d, J = 12.7 Hz, 1H), 4.49 (d, J = 8.2 Hz, 2H), 4.07 (dt, J = 21.1, 7.1 Hz, 2H), 3.96 – 3.87 (m, 2H), 3.81 – 3.68 (m, 2H), 3.64 (d, J = 17.0 Hz, 4H), 3.51 (s, 2H), 3.39 (dd, J = 14.3, 8.1 Hz, 3H), 2.46 (s, 3H), 2.05 (d, J = 7.9 Hz, 6H), 1.37 (d, J = 6.8 Hz, 3H).^{13}C NMR (151 MHz, Methanol-d_4) δ 173.53, 154.83, 150.93, 125.27, 114.86, 110.32, 101.64, 100.72, 100.48, 77.76, 76.68, 75.80, 74.33, 73.89, 73.32, 70.59, 64.38, 61.22, 55.76, 33.95, 22.02, 21.20, 17.22, 14.11, 7.80. Mass Spec: HR-ESI-MS calculated for $C_{33}H_{45}N_5O_{17}S$ [M-H]- 814.2441, found 814.2449

β-D-N-Acetylglucopyranosyl-1,6-anhydro-β-D-N-acetylmuranamide methionine aminomethylcoumarin (21) 10mg (0.009mmol) of (9H-fluoren-9-yl)methyl ((S)-1-((3-(2-((2-((R)-2-(((1R,2R,3R,4S,5R)-4-acetamido-2-(((2R,3R,4R,5S,6R)-3-acetamido-4,5-dihydroxy-6-(hydroxymethyl)tetrahydro-2H-pyran-2-yl)oxy)-6-oxabicyclo[3.2.1]octan-3-yl)oxy)propanamido)ethyl)amino)-2-oxoethyl)-4-methyl-2-oxo-

2H-chromen-7-yl)amino)-4-(methylthio)-1-oxobutan-2-yl)carbamate was stirred in a a 20% solution of piperidine in DMF for 10 minutes. The crude reaction mixture was concentrated by rotary evaporation and purified using a CombiFlash™ chromatography device on normal phase silica followed by HPLC purification to give compound **21** (1.1 mg, 15% yield). 1H NMR (600 MHz, Methanol-d4) δ 7.91 (s, 1H), 7.82 (d, J = 8.6 Hz, 1H), 7.51 (d, J = 8.7 Hz, 1H), 4.51 (d, J = 8.4 Hz, 1H), 4.23 (d, J = 7.5 Hz, 1H), 4.12 (q, J = 6.8 Hz, 2H), 3.91 (dd, J = 12.0, 2.0 Hz, 2H), 3.85 (d, J = 2.0 Hz, 2H), 3.80 – 3.74 (m, 3H), 3.70 (dd, J = 11.8, 5.8 Hz, 2H), 3.67 (d, J = 2.9 Hz, 3H), 3.50 (s, 2H), 3.46 (q, J = 4.3, 3.0 Hz, 4H), 2.49 (s, 5H), 2.07 – 2.02 (m, 8H), 1.36 (d, J = 6.7 Hz, 6H). 13C NMR (151 MHz, Methanol-d4) δ 174.71, 173.49, 171.39, 152.83, 150.23, 125.79, 118.32, 100.52, 78.02, 76.78, 76.01, 73.92, 73.69, 73.29, 70.55, 64.48, 61.19, 55.68, 39.10, 38.22, 33.93, 31.68, 29.35, 29.08, 22.05, 21.24, 17.52, 14.20. Mass Spec: HR-ESI-MS calculated for $C_{38}H_{54}N_6O_{15}S$ [M+H]+ 867.3458, found 867.3431

β-D-N-Acetylglucopyranosyl-1,6-anhydro-β-D-N-acetylmuranamide alanine aminomethylcoumarin (22) 8.8 mg (0.009mmol) of (9H-fluoren-9-yl)methyl ((S)-1-((3-(2-((2-((R)-2-(((1R,2S,3R,4R,5R)-4-acetamido-2-(((2S,3R,4R,5S,6R)-3-acetamido-4,5-dihydroxy-6-(hydroxymethyl)tetrahydro-2H-pyran-2-yl)oxy)-6,8-dioxabicyclo[3.2.1]octan-3-yl)oxy)propanamido)ethyl)amino)-2-oxoethyl)-4-methyl-2-oxo-2H-chromen-7-yl)amino)-1-oxopropan-2-yl)carbamate was stirred in a 20% solution of piperidine in DMF for 10 minutes. The crude reaction mixture was concentrated by rotary evaporation and purified using a CombiFlash™ chromatography device on normal phase silica followed by HPLC purification to give compound **22** (4.1 mg, 57% yield). ^{1}H NMR (600 MHz, Methanol-d_4) δ 7.88 (d, *J* = 2.1 Hz, 1H), 7.49 (dd, *J* = 8.7, 2.1 Hz, 1H), 4.62 (d, *J* = 5.6 Hz, 1H), 4.51 (d, *J* = 8.4 Hz, 1H), 4.27 – 4.21 (m, 1H), 4.11 (p, *J* = 7.0 Hz, 2H), 4.01 (d, *J* = 2.2 Hz, 1H), 3.91 (dd, *J* = 12.0, 2.0 Hz, 1H), 3.86 (d, *J* = 1.8 Hz, 1H), 3.81 – 3.74 (m, 2H), 3.73 – 3.62 (m, 3H), 3.50 (q, *J* = 1.6 Hz, 1H), 3.48 – 3.40 (m, 3H), 2.68 (s, 8H), 2.48 (s, 3H), 2.04 (d, *J* = 13.2 Hz, 6H), 1.64 (d, *J* = 7.1 Hz, 3H), 1.39 – 1.29 (m, 3H). ^{13}C NMR (151 MHz, Methanol-d_4) δ 174.73 (d, *J* = 11.7 Hz), 173.44, 171.88, 171.36, 168.22, 162.16, 152.84, 150.15, 140.76, 125.79, 118.36, 116.78, 115.46, 106.50, 100.55 (d, *J* = 5.5 Hz), 78.07, 76.81, 76.04, 73.94, 73.65, 73.29, 70.57, 64.46, 61.21, 55.67, 49.63, 39.10, 38.98, 38.23 (d, J = 18.5 Hz), 33.89, 22.02, 21.22, 17.52, 16.05, 14.17. Mass Spec: HR-ESI-MS calculated for $C_{36}H_{50}N_6O_{15}$ [M+H]+ 807.3424, found 807.3350

β-D-N-Acetylglucopyranosyl-1,6-anhydro-β-D-N-acetylmuranamide leucine aminomethylcoumarin (23) 9.0 mg (0.008mmol) of (9H-fluoren-9-yl)methyl ((S)-1-((3-(2-((2-((R)-2-(((1R,2S,3R,4R,5R)-4-acetamido-2-(((2S,3R,4R,5S,6R)-3-acetamido-4,5-dihydroxy-6-(hydroxymethyl)tetrahydro-2H-pyran-2-yl)oxy)-6,8-dioxabicyclo[3.2.1]octan-3-yl)oxy)propanamido)ethyl)amino)-2-oxoethyl)-4-methyl-2-oxo-2H-chromen-7-yl)amino)-4-methyl-1-oxopentan-2-yl)carbamate was stirred in a 20% solution of piperidine in DMF for 10 minutes. The crude reaction mixture was concentrated by rotary evaporation and purified using a CombiFlash^{TM} chromatography device on normal phase silica followed by HPLC purification to give compound **22** (3.3 mg, 49% yield). ^{1}H NMR (600 MHz, Deuterium Oxide) δ 7.70 (d, *J* = 8.7 Hz, 0H), 7.57 (d, *J* = 2.1 Hz, 0H), 7.32 (dd, *J* = 8.7, 2.1 Hz, 0H), 5.24 (s, 0H), 4.51 (dd, *J* = 21.2, 7.1 Hz, 1H), 4.06 (t, *J* = 7.7 Hz, 1H), 3.96 (q, *J* = 6.8 Hz, 0H), 3.78 (d, *J* = 2.0 Hz, 0H), 3.75 – 3.67 (m, 1H), 3.67 – 3.47 (m, 2H), 3.42 (dd, *J* = 10.5, 7.9 Hz, 0H), 3.36 – 3.25 (m, 2H), 3.25 – 3.17 (m, 0H), 3.06 (q, *J* = 7.3 Hz, 3H), 2.32 (s, 1H), 1.93 (s, 1H), 1.79 – 1.70 (m, 1H), 1.71 – 1.68 (m, 1H), 1.63 (dp, *J* = 13.5, 6.8 Hz, 0H), 1.15 (dt, *J* = 14.7, 7.1 Hz, 5H), 0.87 (dd, *J* = 6.6, 3.2 Hz, 2H). ^{13}C NMR (151 MHz, Deuterium Oxide) δ 175.74, 175.15, 173.25, 172.89, 169.35, 163.68, 152.52, 152.10, 139.59, 126.38, 117.35, 117.23, 107.97, 100.75, 99.68, 81.59, 76.93, 76.10, 75.86, 74.00, 73.59, 73.22, 69.54 (d, *J* = 18.5 Hz), 64.73, 60.46, 55.37, 52.54, 49.44, 46.55, 39.89, 39.29, 38.32, 34.17, 23.82, 22.27, 21.84, 21.52, 20.83, 18.29, 14.83, 8.12. Mass Spec: HR-ESI-MS calculated for $C_{39}H_{56}N_6O_{15}$ [M+H]+ 849.3894, found 849.3720

2.6.3. Cell Preparation & Spheroplasting

Experiments were carried out in duplicate using existing frozen stock of *E. coli* MG1655 and BW25113 strains leftover from the original research carried out by Perley Robertson and Yadav in the Vocadlo lab[68]. Deletion of *E.coli* AmpG from the chromosome of MG1655 and BW25113 in these cell stocks was followed by transformation with with pBAD-Pa-AmpG-V5His-Km expression vectors or pBAD-Pa-AmpG-V5His-Km Cell culturing, harvest, and spheroplasting were carried out according to previously published protocol[68]. Overnight cultures of MG1655 or BW25113 were prepared in lysogeny broth (LB) and grown overnight at 37 ◦C in the presence of 35 µg/mL of kanamycin. The following morning the cells were inoculated with a 50-fold dilution into 400 mL of LB and allowed to grow at 28 ◦C until the OD600 was observed to

reach 0.6-0.7. Expression of ampG was induced for an additional 4 hours at this point with the addition of 0.2% (w/v) L-arabinose. In the case of BW25113 cells, cephalexin (6 µg/mL) was added during the last hour of induction. The cells were centrifuged at 3000 rcf at 4◦C and the pellet resuspended in 100 mL of 0.8 M sucrose solution. The spheroplasting procedure was initiated within 24 hours of this time and the sucrose suspended cells were stored in the fridge at 6 ◦C. Spheroplast was initiated with the rapid and successive addition of 6 mL of 0.2 M Tris (pH 7.2), 4.8 mL of 1 mg/mL lysozyme, and 6 mL of 0.025 M EDTA. The cell solution was allowed to sit for a maximum of 15 minutes following the addition of these reagents and spheroplast formation and completion was monitored with DIC microscopy of intermittent sample aliquots during the process. Once judged complete, an ice chilled stop solution (87.5% 0.8 M sucrose, 9.5% deionized water, 2% 1 M $MgCl_2$, 1% 1 M Tris) was added followed by 280 mL of dilution solution (98% 0.8M sucrose, 1% 1 M $MgCl_2$, 1% 1 M Tris). The diluted spheroplast solution was immediately centrifuged at 2000 rcf at 4 ◦C for 25 minutes and the pellet subsequently washed with dilution solution before being resuspended at 4 g/mL in dilution solution. Spheroplasts were used within 48 hours of this procedure and stored in the fridge at 6 ◦C otherwise.

2.6.4. Spheroplast Uptake Assay

Experiments were carried out according to the previously published protocol by Perley-Robertson and Yadav[68]. 100 µL of *E.coli* MG1655 or BW25113 spheroplasts and the corresponding ΔampG strains were added to 1 mL Eppendorf tubes followed by the addition of 150 µL of dilution solution. The assay was initiated with the addition of 100 µL of 175 µM probe followed by inversion of the tubes several times to homogenize the solution. The final reaction concentrations were 50 µM probe and 0.12 g/mL spheroplasts. In the case of kinetic plate reader analysis, 150 µL aliquots of this solution were transferred to 96 well solid black flat bottom plates and immediately following mixing and submitted for analysis on a Synergy H1 Hybrid Multi-Mode Microplate Reader. In the case of endpoint scans following incubation and washing of cells, the Eppendorf tubes were incubated at room temperature using a digital heating block for 2 hours in darkness. Following this incubation, 1 ml of ice chilled dilution solution was added to each Eppendorf tube following by 2000 rcf centrifugation at 4 ◦C for 20 minutes. The supernatant is the removed with a syringe making effort to minimally perturb the

pellet and replaced with 1 mL of fresh ice chilled dilution solution. The pellet is then gently resuspended using a 1 mL micropipette without sucking up the pellet itself before further successive cycles of centrifugation, supernatant drainage and resuspension. After four cycles total, the cells are suspended in 200 µL of dilution solution and 150 µL aliquots are transferred to a 96 well solid black flatbottom plate for fluorescence endpoint scans on a Synergy H1 Hybrid Multi-Mode Microplate Reader.

2.6.5. Microscopy

Differential contrast interference imaging of bacteria for the purposes of the spheroplasting procedure and following the ampG transport assay were captured using Zeiss Axio Observer inverted microscope equipped with a Yokogawa CSU-10 confocal head. Imaging was carried out with a 62X oil objective lens. A Hammamatsu and 9100 EMCCD camera controlled through Volocity acquisition software. Fluorescence images were captured using Nikon A1R Ti-inverted microscope equipped with a 32-channel spectral detector, 60X oil objective lens and Hammamatsu 9100 EMCCD camera. Acquisition was operated using Nikon Elements 4.2 software. Excitation wavelengths of 350nm (compound 20), 380nm (compound 21-23), 410nm (compound 18) and 503nm (compound 15) were used during fluorescence microscopy.

Chapter 3. Development of a Practical Large-Scale Synthesis of Thiamet-G

3.1. Abstract

Herein is reported a large-scale synthesis of Thiamet G, a potent inhibitor of the glycoside hydrolase O-GlcNAcase and a compound of clinical research interest for its potential application in various illnesses including cardiovascular disease, tauopathies, and conditions associated with cardiac ischemia. This work represents a significant improvement in the scalability and efficiency of previously reported synthetic routes while also improving protocol safety, product purity, and overall yield. The volumes of solvent are significantly reduced, use of toxic reagents are reduced or entirely eliminated, and the need for chromatographic purification is eliminated whilst affording the final product in high purity. The utility of the methods described are illustrated by a single production run yielding 150 grams of Thiamet-G using glassware commonly found within academic chemistry laboratories.

3.2. Contributions

The original synthetic scheme for Thiamet-G was established in 2008[61]. The revised synthesis described herein was developed in a collaborative effort between Matthew Deen and Viktor Holicek.

3.3. Introduction

O-linked *N*-acetylglucosamine (O-GlcNAc) modification of serine and threonine protein residues is a dynamic and wide-spread post translational modification found on hundreds of proteins within all multicellular eukaryotes studied to date[90,91]. O-GlcNAc modification has been demonstrated to affect cell and organismal physiology, affecting many process including, for example, cellular homeostasis[92], transcription[93], development[94], and autophagy[28]. Studies focused on O-GlcNAcylation within various animal models has implicated this modification within a host of chronic diseases ranging from neurodegeneration[43] to cancer[31,40–42] and on to cardiovascular[34–36] disease[33–38]. Many of these physiological findings have been uncovered with the aid of small molecule

inhibitory tool compounds which have been used manipulate O-GlcNAcylation in cellular and *in vivo* models.

Among these inhibitors, Thiamet-G, a selective and potent inhibitor of O-GlcNAcase (OGA) (K_i = 2.1 nM), the sole enzyme responsible for removing O-GlcNAc[32], has proven to be a particularly valuable tool compound for the field. Thiamet-G was developed as a means to probe the dynamic relationship between O-GlcNAc and phosphorylation of the microtubule associated protein tau whose aggregates are a classical hallmark of Alzheimer's disease[61]. The design of the inhibitor was inspired by mechanistic studies of the OGA enzyme and was first reported in 2008[61]. Thiamet-G is a transition state analogue, which in part accounts for its far exceeding previously reported inhibitors in both selectivity and binding affinity[61]. Subsequently, Thiamet-G has found application in studying the impact of increased O-GlcNAc levels within a number of disease models. One of the disease areas in which it has had the most impact in is in neurodegeneration, where it has been used in many studies focused on Alzheimer's Disease (AD)[55], Parkinson's (PD)[95], Progressive Supranuclear Palsy (PSP)[96], and Huntington's Disease[97]. The ability of Thiamet-G to slow neurodegeneration in AD tauopathy mouse models has been reproducibly demonstrated[98] and the compound has since been exploited as a lead molecule that was optimized to produce an improved analog (MK-8719) with improved pharmacokinetic properties that has been taken into Phase 1 clinical trials for PSP, where it was shown to be generally well tolerated in patients[62]. Efforts such as this demonstrate the interest behind structurally optimizing and exploring derivatives of Thiamet-G and highlight its value as a synthetic precursor to clinically relevant pharmaceutical compounds. Similarly, the growing use of Thiamet-G in academic animal studies requires access to large and high quality compound since the modest brain exposure for this tool compound requires administration of relatively high doses[9,17,24–27]. Furthermore, commercially available Thiamet-G can be prohibitively expensive to purchase at scales needed for animal studies or even for sustained cellular experimentation. Taken together, the increased quantities of Thiamet-G needed to support these avenues of research highlight the need for a more accessible and straightforward synthetic route to production. Several key aspects of the original synthesis pose safety and practical concerns. We sought to exclude the used of toxic heavy metals, reduce the large solvent volumes that could necessitate large reactor vessels, reduce the need for excess reagents, and minimize the labour and cost

associated with intensive chromatographic purification of intermediates. These goals were pursued while focusing on ensuring production of high purity final product necessary for animal use. Here we described a convenient synthetic route, using conventional academic laboratory equipment, designed to overcome these challenges. This route can be applied both at small scale but we also illustrate its utility for large scale production by producing, within a single run, 150 g of Thiamet-G.

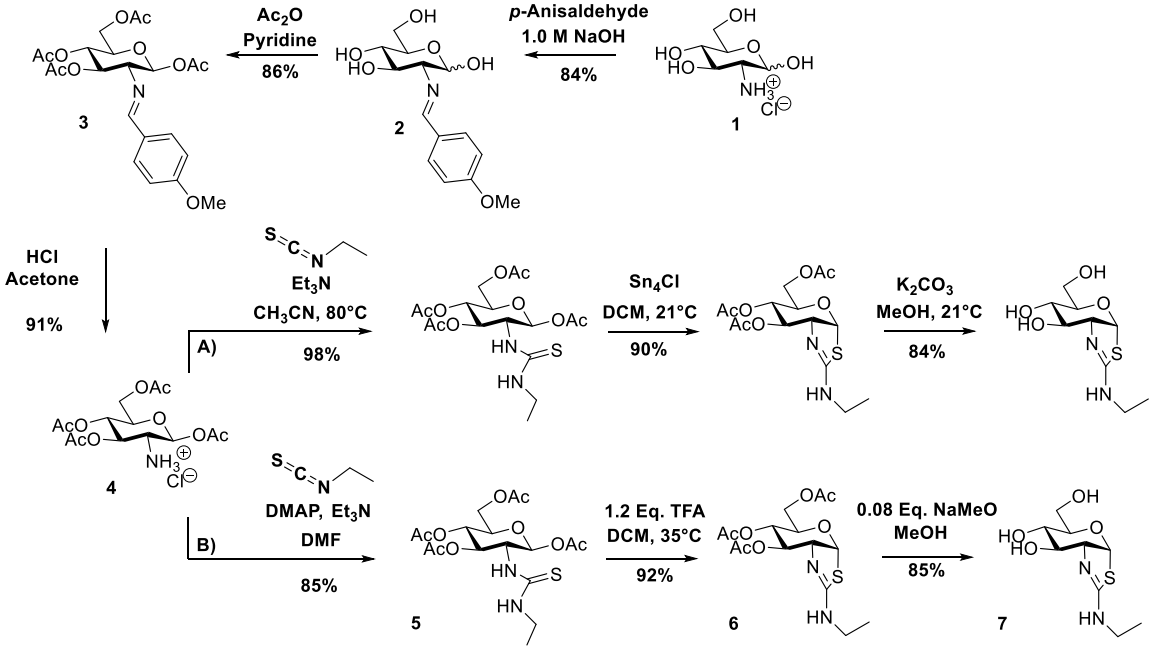

Scheme 3.1. Synthesis of Thiamet-G from Commercially Available GlcNAc•HCl
The synthesis of Thiamet-G begins with glucosamine hydrochloride salt (**1**) from which the 1,3,4,6-tetra-acetyl glucosamine hydrochloride intermediate (**4**) may be formed using previously established methods. The upper pathway (A) depicts the original synthetic route for the subsequent three steps, while the newly proposed optimized route (B) is illustrated below.

3.4. Results and Discussion

The in-house production of 150 g of Thiamet-G required a large quantity of the hydrochloride salt intermediate (**4**), which while commercially available (approximately $4,500 / kg), was an expensive starring material. Therefore, beginning with the more readily available glucosamine hydrochloride salt precursor (**1**) was a much more economical alternative ($60.00 / kg). The previously reported synthesis[103] for intermediate **4** was adapted to use generally available materials which allowed us to produce hundred gram quantities of this compound in 66% yield over three steps. Initial

efforts to scale up the previously reported formation of the thiourea intermediate (**5**) using ethyl isothiocyanate (EIT) at a multigram scale failed to reproduce the reported 98% yield[61] and resulted in incomplete turnover of the starting material based on TLC. In addition, both the volume of refluxing solvent and subsequent flash column silica gel chromatography of the product were prohibitive at large scale. We hypothesized that inclusion of a nucleophilic catalyst would serve to facilitate product formation. In performing single gram test reactions, we found that inclusion of pyridine significantly reduced reaction time and the need for reflux. Following this observation, and to further minimize the volumes of reagents needed, we replaced pyridine with 4-dimethylaminopyridine (DMAP) as a more potent nucleophilic catalyst. DMAP functioned equally well and also enabled simple removal of the reagent during aqueous workup of the crude material. Notably, the addition of nucleophilic catalysts such as pyridine and 4-dimethylaminopyridine (DMAP) have seen limited use in the synthesis of thioureas, however, optimizing the fractional equivalencies of either DMAP or pyridine as nucleophilic catalysts in acetonitrile allowed the reaction to proceed efficiently at room temperature and with reduced equivalents of ethyl isothiocyanate. In scaling up the reaction, the poor solubility of HCl salt **4** presented problems at multi-molar quantities. Several solvents were tested, of which DMF proved to be the best with respect to ensuring timely completion of the reaction yet also the most difficult to remove to enable concentrating the product. To this end, the concentration of starting material was increased to 1.0 M, enabling a 90% reduction in the reaction volume, which allowed its facile removal during workup. Using these measures yields were obtained that were similar to those achieved in the original synthetic report using acetonitrile (Table 3.1). More conveniently, however, in addition to accelerating the reaction, the product obtained directly from the workup was pure enough to carry on to the next step without purification.

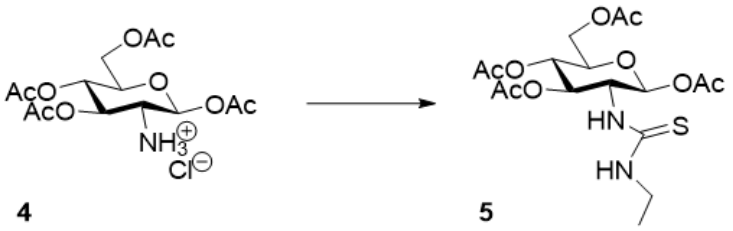

4 5

Condition	Catalyst	Cat. Equiv.	EIT Equiv.	Temp. (°C)	Solvent	Amine [M]	Time (h)	Yield (%)
Reported	-	-	3.0	80	ACN	0.06	-	96
1	-	-	3.0	25	DCM	0.1	96	49
2	-	-	3.0	25	Pyridine	0.1	48	88
3	-	-	3.0	25	ACN	0.1	72	65
4	Pyridine	0.20	1.2	25	ACN	0.1	48	74
5	DMAP	0.20	1.2	25	ACN	0.1	48	71
6	DMAP	0.02	1.2	50	ACN	0.1	24	42
7	Pyridine	0.20	1.2	25	DMF	0.1	24	78
8	DMAP	0.02	1.2	25	DMF	0.1	36	76
9	DMAP	0.02	1.2	25	DMF	1.0	36	85

Table 3.1. Reactions were carried out at 1.0 gram scale in the presence of 1.8 equivalents of triethylamine. Variation in nucleophilic catalyst, temperature, solvent, and reagent concentration were used to examine changes in both time to completion of the reaction and isolated yield.

Following installation of the thiourea, cyclization to produce aminothiazoline **5** was previously carried out in the presence of four equivalents of the Lewis acid catalyst Sn(IV)Cl_4. Under these conditions, kilogram quantities of Stannic Chloride would be required to produce 500 g of Thiamet-G, leading us to search for other less toxic and more effective alternatives. Trifluoroacetic acid has previously been shown as an effective cyclization reagent for the synthesis of thiazolines at room temperature[104]. Experimentation with this as a substitute catalyst enabled us to both reduce the amount of DCM used as solvent by 60% and the number of equivalents of the catalyst by 70% (Table 3.2) as compared to the reported synthetic route.

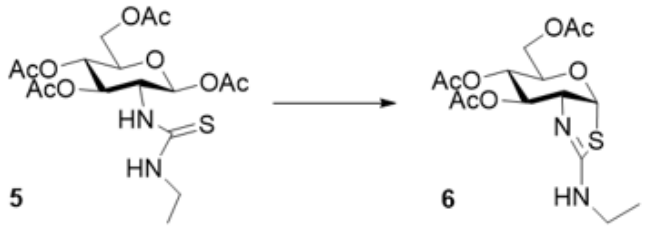

Condition	Catalyst	Cat. Eq.	Temp. (°C)	Solvent [M]	Time (h)	Yield (%)
Reported	$SnCl_4$	4.0	20	0.06	24	-
1	TFA	7.5	25	0.1	16	86
2	TFA	1.2	25	0.1	48	98
3	TFA	0.2	25	0.1	48	90
4	TFA	0.2	38	0.1	24	90
5	TFA	1.2	38	0.25	24	92

Table 3.2. Reactions were carried out at 1.0 gram scale. Variation in the catalyst, temperature, solvent, and reagent concentration were used to examine changes in yield and completion time.

The originally reported synthesis reported using 5% w/v K_2CO_3 in the final deprotection step. We elected to use catalytic quantities of sodium methoxide since we expected this would require a far smaller quantity of reagent with an improved reaction time because of the improved solubility of sodium methoxide in organic solvents as compared to potassium carbonate. Upon completion of the reaction, we added an equimolar quantity of sodium bisulfate as an inexpensive and readily measurable solid material that could be used to neutralize the base catalyst. Column chromatography of the crude material as reported in the original synthesis was prohibitive given the large scale and propensity for Thiamet-G to decompose upon prolonged exposure to acidic silica. In light of this, recrystallization techniques using organic solvents provided an alternative convenient means to obtain purified Thiamet-G. To the crude product, obtained after removing solvent in vacuo, was added a minimal volume of methanol and ethyl acetate (9:1 v/v) with heating to 55 °C to dissolve the material, after which the solution was gradually cooled to -20 °C and stored overnight. The resulting white precipitate was decanted over a Buchner funnel, the cake rinsed with chilled methanol and ethyl acetate (9:1 v/v),and dried under vacuum to obtain fine white crystals of aminothiazoline **6** in >99 % purity as judged by analysis using HPLC and NMR. The process was repeated with the filtrate three times to enable a cumulative yield of 85%.

3.5. Conclusion

We demonstrate a convenient and rapid series of transformations that can be performed at scale to synthesize Thiamet-G from inexpensive and readily available glucosamine hydrochloride salt **1** in 44% yield over six steps in greater than 99% purity. This route is performed without requiring column chromatography at any step and with a significant reduction in the need for solvents, reagents, and elimination of toxic metal catalysts. This optimized route, in conjunction with aqueous workup methods and a final recrystallization step make amenable the large-scale production of Thiamet-G using conventional academic laboratory equipment. We anticipate these methods will greatly facilitate the application of Thiamet-G as a tool compound for use in animal models of various diseases, which will help uncover the therapeutic potential of OGA inhibitors.

3.6. Experimental Section

3.6.1. General Chemical Methods

Unless stated otherwise, all reagents were purchased from commercial sources and were used without further purification. Anhydrous solvents used in reactions were purchased from commercial sources. Reactions were monitored by thin layer chromatography (TLC) on Silica Aluminum TLC plate, silica gel coated with fluorescent indicator F254. TLC spots were detected under UV light (254 λ /365 λ) and/or by charring with potassium permanganate or “Seebach” stain (2.5 g phosphomolybdic acid, 1 g $Ce(SO_4)^2$, 6 mL conc H_2SO_4, 94 mL H_2O.). High pressure liquid chromatography (HPLC) was performed on an Agilent 1260 Infinity device equipped with a variable wavelength UV-Vis detector using ZORBAX 300SB C8 column (5.0 µm, 9.4 x 250 mm for analytical runs and semi-preparative scale purifications) and elution carried out using HPLC grade solvents. In concentrating reactions, solvents were evaporated under reduced pressure on a rotary evaporator between 40–60 ºC using either a PIAB vacuum system or Welch W Series high vacuum oil pump. NMR spectra were recorded on Bruker AVANCE III 400 or AVANCE II 600_QNP. Spectra are referenced according to the chemical shift of the deuterated solvent in which they were dissolved (^{1}H NMR: $CDCl_3$: 7.26 ppm, CD_3OD: 3.30 ppm; ^{13}C NMR: $CDCl_3$: 77.0 ppm; CD_3OD 49.0 ppm) and peak assignments were made on the basis of 2D-NMR (^{1}H COSY, HSQC, HMBC)

experiments. High resolution mass spectra (HRMS) were recorded on a Bruker MaXis Impact spectrometers using positive or negative electrospray ionization (ESI).

3.6.2. Synthesis of Key Chemical Compounds

Synthesis of **2-deoxy-2-[[(4-methoxyphenyl)methylene]amino]-β-D-glucopyranose (2).** To a solution of glucosamine hydrochloride (**1**, 2.044 g, 9.5 mol) in NaOH solution (1 M, 9.48 L) at 0 °C was added p-anisaldehyde (1.15 L, 9.48 mol) dropwise over 30 minutes under mechanical stirring. The resulting mixture was stirred at 0 °C for 1 h and the precipitate was collected by Buchner funnel suction filtration, washed successively with cold water (9.5 L), cold ethanol (9.5 L) and diethyl ether (9.5 L), and then dried under vacuum to give the title compound (**2**) as a white solid (2.37 kg, 84% yield). ^{1}H NMR (400 MHz, DMSO-d_6) δ 8.12 (s, 1H), 7.73 – 7.66 (m, 2H), 7.03 – 6.96 (m, 2H), 6.54 (d, *J* = 6.7 Hz, 1H), 4.94 (d, *J* = 5.3 Hz, 1H), 4.83 (d, *J* = 5.6 Hz, 1H), 4.70 (dd, *J* = 7.7, 6.8 Hz, 1H), 4.57 (t, *J* = 5.8 Hz, 1H), 3.80 (s, 3H), 3.73 (ddd, *J* = 11.7, 5.6, 2.0 Hz, 1H), 3.54 – 3.37 (m, 2H), 3.28 – 3.09 (m, 2H), 2.79 (dd, *J* = 9.3, 7.7 Hz, 1H).

Synthesis of **1,3,4,6-tetra-O-acetyl-2-deoxy-2-[[(4-methoxyphenyl)-methylene]amino]-β-Dglucopyranose (3).** Imine **2** (700 g, 2.35 mol) and pyridine (3.0 L, 37.6 mol) were stirred for 5 m in an ice bath at 0 °C under N_2 atmosphere. Acetic anhydride (5.52 L, 58.4 mol) was then added slowly over the course of an hour with continuous stirring. The reaction mixture was maintained at 0 °C for 2 h and then at room temperature overnight. The reaction was quenched by transferring 1.0 L portions of the reaction into 4.0 L of ice water at 0 °C. The precipitate was collected by filtration, washed with cold water and dried under vacuum to give the title compound (**3**) as a white solid (943 g, 86 % yield). ^{1}H NMR (400 MHz, Chloroform-*d*) δ 8.18 (s, 1H), 7.72 – 7.61 (m, 2H), 6.98 – 6.88 (m, 2H), 5.96 (d, *J* = 8.3 Hz, 1H), 5.45 (t, *J* = 9.6 Hz, 1H), 5.16 (t, *J* = 9.8 Hz, 1H), 4.40 (dd, *J* = 12.4, 4.5 Hz, 1H), 4.15 (dd, *J* = 12.4, 2.1 Hz, 1H), 3.99 (ddd, *J* = 10.1, 4.5, 2.1 Hz, 1H), 3.86 (s, 3H), 3.47 (dd, *J* = 9.8, 8.3 Hz, 1H), 2.12 (s, 3H), 2.05 (d, *J* = 6.4 Hz, 6H), 1.90 (s, 3H).

Synthesis of **2-amino-2-deoxy-1,3,4,6-tetra-O-acetyl-β-D-glucopyranose (4).** A solution of O-acetylated imine **3** (885 g, 1.90 mol) in acetone (6.4 L) was treated with 5 M HCl (396 mL, 1.98 mol). The solution was stirred for 30 min before diethyl ether (3 L) was added, and the stirring was continued for a further 1 h. The precipitate was collected

via suction filtration, washed with 3 L of cold diethyl ether and dried under vacuum to give the title compound (**4**) as a white solid (721 g, 99 % yield). ^{1}H NMR (400 MHz, Methanol-d_4) δ 5.91 (d, J = 8.7 Hz, 1H), 5.39 (dd, J = 10.6, 9.1 Hz, 1H), 5.12 (dd, J = 10.2, 9.1 Hz, 1H), 4.33 (dd, J = 12.6, 4.6 Hz, 1H), 4.14 (dd, J = 12.6, 2.3 Hz, 1H), 4.05 (ddd, J = 10.1, 4.6, 2.3 Hz, 1H), 3.66 (dd, J = 10.5, 8.8 Hz, 1H), 2.22 (s, 3H), 2.17 – 2.01 (m, 9H).

Synthesis of **2-deoxy-2-ethylthioureido-1,3,4,6-tetra-O-acetyl-β-D-glucopyranose (5).** To a suspension of 1,3,4,6-tetra-acetyl glucosamine hydrochloride (**4**, 400 g, 1.04 mol) in anhydrous DMF (1.0 L) with 2.55 g DMAP (0.02 moles) and was treated dropwise over 30 minutes with triethylamine (256 mL, 1.84 moles). 110 mL (1.25 moles) of ethyl isothiocyanate was added gradually using a dropwise additional funnel over the course of 2.5 hours. The reaction was then stirred at room temperature for 2 days. Following reaction completion as judged by TLC (95% CH_2Cl_2 5% MeOH v/v) the mixture was diluted with 4 L of DCM and washed sequentially with a 4 L solution water and brine (50 % v/v), 4L of 0.01 M HCl, 4 L of saturated $NaHCO_3$, and finally 4 L of brine. The organic layer was then dried using sodium sulfate and co-concentrated with a toluene azeotrope yielding the product as a dark yellow viscous liquid (384 g, 85% yield). ^{1}H NMR (400 MHz, Methanol-d_4) δ 6.14 (t, J = 5.2 Hz, 1H), 5.75 (d, J = 8.5 Hz, 1H), 5.26 – 5.15 (m, 2H), 4.30 (dd, J = 12.5, 4.6 Hz, 1H), 4.16 (dd, J = 12.5, 2.3 Hz, 1H), 3.85 (ddd, J = 9.5, 4.3, 2.2 Hz, 1H), 2.16 (s, 3H), 2.12 (s, 3H), 2.09 (s, 3H), 2.07 (s, 3H), 1.22 (t, J = 7.2 Hz, 3H). ^{13}C NMR (151 MHz, Methanol-d_4) δ 171.66, 170.76 169.78, 169.60, 169.34, 92.96, 73.02, 72.84, 67.71, 63.11, 61.67, 21.07, 20.86, 20.77, 20.62, 14.81, 14.08. HR-ESI-MS calculated for $C_{17}H_{26}N_2O_9S$ [M+H]+ 435.14, found 435.1431

Synthesis of **3,4,6-tri-O-acetyl-1,2-dideoxy-2'-ethylamino-α-D-glucopyranoso-[2,1-d]-Δ2'- thiazoline (6).** 350 g of the dry thiourea **5** (0.805 mol) was dissolved in DCM (3.3 L) to which 74 mL of TFA (0.969 mol) was added. The reaction mixture was then heated to reflux and stirred until TLC (95% CH_2Cl_2 5% MeOH v/v) showed reaction completion (1-2 days). The resulting reaction mixture was filtered through celite and washed with saturated $NaHCO_3$. The organic layer was concentrated in-vacuo to give the cyclized aminothiazoline product **6** as a flaky light yellow solid (278 g, 92%). ^{1}H NMR (400 MHz, Methanol-d_4) δ 6.23 (d, J = 6.5 Hz, 1H), 5.43 (dd, J = 4.1, 2.7 Hz, 1H), 4.95 (ddd, J = 9.5, 2.7, 1.1 Hz, 1H), 4.36 (ddd, J = 6.5, 4.1, 1.1 Hz, 1H), 4.21 – 4.09 (m, 2H), 3.90 – 3.79 (m, 1H), 3.46 – 3.20 (m, 2H), 2.11 (s, 3H), 2.08 (s, 3H), 2.07 (s, 3H), 1.21 (t,

J = 7.2 Hz, 3H). ^{13}C NMR (151 MHz, Methanol- d_4) δ 170.72, 169.71, 169.52, 89.64, 72.65, 71.87, 69.11, 68.50, 63.24, 39.45, 21.05, 20.91, 20.83, 14.87, 1.04. HR-ESI-MS calculated for $C_{15}H_{22}N_2O_7S$ [M+H]+ 375.11, found 375.1258

Synthesis of **1,2-dideoxy-2'-ethylamino-α-D-glucopyranoso-[2,1-d]-Δ2'-thiazoline (7).** 278 g of tri-O-acetylated Thiamet-G **6** (0.74 mol) was dissolved into 2.97 L of anhydrous methanol (0.25 M solution) followed by addition of 185 mL of 0.2 M (37.1 mmol) solution of sodium methoxide. The mixture was then stirred at room temperature until judged to be complete by TLC (95% CH_2Cl_2 5% MeOH v/v). The base was neutralized using a 1.0 M aqueous solution to yield an equimolar addition of sodium bisulfate (4.45 g, 37.1 mmol) and the resulting mixture was subsequently filtered through a pad of celite before concentrating the resulting organic layer *in vacuo*. The product was isolated via recrystallization of the crude dried material as described below to yield Thiamet-G.

3.6.3. Recrystallization of Thiamet G

Crude Thiamet G was completely dissolved in a minimal volume of 9:1 MeOH EtOAc (approximately 10 mL / g) with the aid of heating (55 °C) and mixing within the rotary evaporator under reduced atmospheric pressure. Once dissolved, the solution was allowed to cool down to room temperature and then placed in a -20 °C freezer overnight to precipitate. The next day, the solution was decanted and collected for further recrystallization, while the precipitate was collected on a Buchner funnel, rinsed with a chilled solution of 9:1 MeOH EtOAc v/v, and then dried overnight under high vacuum to yield Thiamet G as a fine white crystalline powder. The consolidated product from three cycles of recrystallization provided 157 g in 85% isolated yield. Decomposition point 143 °C. Elemental analysis, Predicted: C 43.54% H 6.50% N 11.28%, Found: C 43.70% H 6.36% N 11.25%. ^{1}H NMR (600 MHz, Methanol-d_4) δ 6.29 (d, *J* = 6.3 Hz, 1H), 4.05 (t, *J* = 6.1 Hz, 1H), 3.93 (t, *J* = 5.6 Hz, 1H), 3.79 (dd, *J* = 11.7, 2.1 Hz, 1H), 3.70 – 3.58 (m, 2H), 3.48 (dd, *J* = 9.1, 5.3 Hz, 1H), 3.31 – 3.22 (m, 2H), 1.17 (t, *J* = 7.2 Hz, 3H). ^{13}C NMR (151 MHz, Methanol- d_4) δ 163.08 , 90.85 , 76.29 , 75.77 , 75.72 , 71.20 , 63.26 , 39.57 , 14.88. HR-ESI-MS calculated for $C_9H_{16}N_2O_4Sz$ [M+H]+ 249.08, found 249.0904.

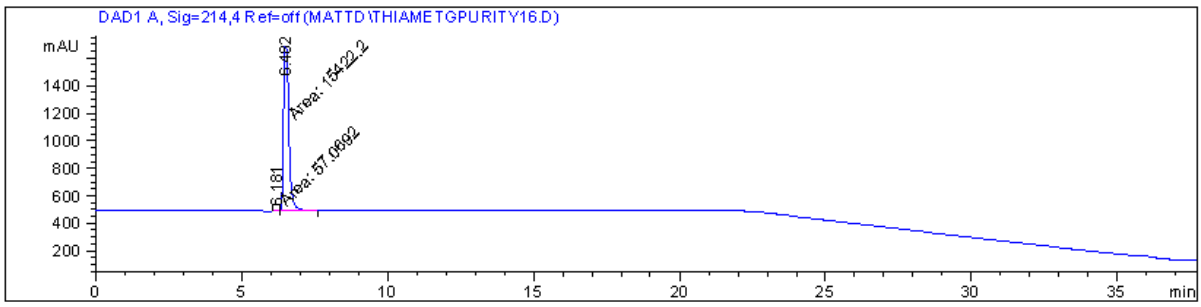

Signal 1: DAD1 A, Sig=214,4 Ref=off

Peak #	RetTime [min]	Type	Width [min]	Area [mAU*s]	Height [mAU]	Area %
1	6.181	MM	0.1117	57.06924	8.51587	0.3687
2	6.482	MM	0.2150	1.54222e4	1195.31360	99.6313
Totals :				1.54793e4	1203.82947	

Figure 3.1. HPLC chromatogram of recrystallized Thiamet-G

HPLC chromatogram of recrystallized Thiamet-G obtained using a Zorbax SB-300 C8 semi preparatory column and an elution profile of 70% A : 30% B for 15 minutes then starting a gradient to 10% A : 90% B over 15 minutes, where solvent A is 50 mM ammonium acetate buffer (pH = 6.8) and solvent B is an 80:20 mixture of HPLC grade MeOH and 50 mM ammonium acetate buffer (pH 6.8).

References

1. Romo, A. C. de. Tallow and the Time Capsule : Claude Bernard's Discovery of the Pancreatic Digestion of Fat Source. *Hist. Philos. Life Sci*. **11**, 253–274 (1989).

2. Jackson, C. M. Emil Fischer and the 'art of chemical experimentation'. *Hist. Sci.* **55**, 86–120 (2017).

3. Mergenthaler, P., Lindauer, U., Dienel, G. A. & Meisel, A. Sugar for the brain: The role of glucose in physiological and pathological brain function. *Trends Neurosci.* **36**, 587–597 (2013).

4. Akram, M. Mini-review on glycolysis and cancer. *J. Cancer Educ.* **28**, 454–457 (2013).

5. Guo, X. *et al.* Glycolysis in the control of blood glucose homeostasis. *Acta Pharm. Sin. B* **2**, 358–367 (2012).

6. Ge, T. *et al.* The Role of the Pentose Phosphate Pathway in Diabetes and Cancer. *Front. Endocrinol.* **11**, 1–11 (2020).

7. Lampugnani, E. R., Khan, G. A., Somssich, M. & Persson, S. Building a plant cell wall at a glance. *J. Cell Sci.* **131**, (2018).

8. Cabib, E. & Arroyo, J. How carbohydrates sculpt cells: Chemical control of morphogenesis in the yeast cell wall. *Nat. Rev. Microbiol.* **11**, 648–655 (2013).

9. Scientific, A. & Health, N. ABO Blood Type-Food Relationship : The Mechanism of Interaction between Food and Human Glycans. *Acta Sci. Nutr. Heal.* **3**, 3–22 (2019).

10. Green, C. The ABO, Lewis and related blood group antigens; a review of structure and biosynthesis. *FEMS Microbiol. Lett.* **47**, 321–330 (1989).

11. Zhu-Mauldin, X., Marsh, S. A., Zou, L., Marchase, R. B. & Chatham, J. C. Modification of STIM1 by O-linked N-Acetylglucosamine (O-GlcNAc) attenuates store-operated calcium entry in neonatal cardiomyocytes. *J. Biol. Chem.* **287**, 39094–39106 (2012).

12. Deribe, Y. L., Pawson, T. & Dikic, I. Post-translational modifications in signal integration. *Nat. Struct. Mol. Biol.* **17**, 666–672 (2010).

13. Moremen, K. W., Tiemeyer, M. & Nairn, A. V. Vertebrate protein glycosylation: diversity, synthesis and function. *Nat. Rev. Mol. Cell. Biol*. **13**, 448–462 (2014).

14. Wang, Y. C., Peterson, S. E. & Loring, J. F. Protein post-translational modifications and regulation of pluripotency in human stem cells. *Cell Res.* **24**,

143–160 (2014).

15. Apweiler, R., Hermjakob, H. & Sharon, N. On the frequency of protein glycosylation, as deduced from analysis of the SWISS-PROT database. *Biochim. Biophys.* **1473**, 4–8 (1999).

16. Reily, C., Stewart, T. J., Renfrow, M. B. & Novak, J. Glycosylation in health and disease. *Nat. Rev. Nephrol.* **15**, 346–366 (2019).

17. Bacik, J. P., Whitworth, G. E., Stubbs, K. A., Vocadlo, D. J. & Mark, B. L. Active site plasticity within the glycoside hydrolase NagZ underlies a dynamic mechanism of substrate distortion. *Chem. Biol.* **19**, 1471–1482 (2012).

18. Chakladar, S. *et al.* A mechanism-based inactivator of glycoside hydrolases involving formation of a transient non-classical carbocation. *Nat. Commun.* **5**, 1–8 (2014).

19. Lindquist, S. *et al.* AmpG, a signal transducer in chromosomal β-lactamase induction. *Mol. Microbiol.* **9**, 703–715 (1993).

20. Jacobs, C., Huang, L. J., Bartowsky, E., Normark, S. & Park, J. T. Bacterial cell wall recycling provides cytosolic muropeptides as effectors for β-lactamase induction. *EMBO J.* **13**, 4684–4694 (1994).

21. Korfmann, G. & Sanders, C. C. ampG is essential for high-level expression of AmpC β-lactamase in Enterobacter cloacae. *Antimicrob. Agents Chemother.* **33**, 1946–1951 (1989).

22. Davies, G. & Henrissat, B. Structures and mechanisms of glycosyl hydrolases. *Structure* **3**, 853–859 (1995).

23. Torres, C. R. & Hart, G. W. Topography and polypeptide distribution of terminal N-acetylglucosamine residues on the surfaces of intact lymphocytes. Evidence for O-linked GlcNAc. *J. Biol. Chem.* **259**, 3308–3317 (1984).

24. Whisenhunt, T. R. *et al.* Disrupting the enzyme complex regulating O-GlcNAcylation blocks signaling and development. *Glycobiology* **16**, 551–563 (2006).

25. Brimble, S., Wollaston-Hayden, E., Teo, C., Morris, A. & Wells, L. The Role of the O-GlcNAc Modification in Regulating Eukaryotic Gene Expression. *Curr. Signal Transduct. Ther.* **5**, 12–24 (2010).

26. Fisi, V., Miseta, A. & Nagy, T. The Role of Stress-Induced O-GlcNAc Protein Modification in the Regulation of Membrane Transport. *Oxid. Med. Cell. Longev.* **2017**, 1-15 (2017).

27. Marissa R. Martinez, Dias, T. B., Natov, P. S. & Natasha E. Zachara. Stress-

Induced O-GlcNAcylation, an Adaptive Process of Injured Cells. *Biochem Soc Trans* **8**, 237–249 (2017).

28. Zhu, Y. *et al.* Pharmacological Inhibition of O-GlcNAcase Enhances Autophagy in Brain through an mTOR-Independent Pathway. *ACS Chem. Neurosci.* **9**, 1366–1379 (2018).

29. Wang, Z. *et al.* Extensive crosstalk between O-GlcNAcylation and phosphorylation regulates cytokinesis. *Sci. Signal.* **3**, 1–22 (2010).

30. Wang, Z., Pandey, A. & Hart, G. W. Dynamic interplay between O-linked N-acetylglucosaminylation and glycogen synthase kinase-3-dependent phosphorylation. *Mol. Cell. Proteomics* **6**, 1365–1379 (2007).

31. Jaskiewicz, N. M. & Townson, D. H. Hyper-O-GlcNAcylation promotes epithelial-mesenchymal transition in endometrial cancer cells. *Oncotarget* **10**, 2899–2910 (2019).

32. Gao, Y., Wells, L., Comer, F. I., Parker, G. J. & Hart, G. W. Dynamic O-glycosylation of nuclear and cytosolic proteins: Cloning and characterization of a neutral, cytosolic β-N-acetylglucosaminidase from human brain. *J. Biol. Chem.* **276**, 9838–9845 (2001).

33. Baldini, S. F., Wavelet, C., Hainault, I., Guinez, C. & Lefebvre, T. The Nutrient-Dependent O-GlcNAc Modification Controls the Expression of Liver Fatty Acid Synthase. *J. Mol. Biol.* **428**, 3295–3304 (2016).

34. Heath, J. M. *et al.* Activation of AKT by O-linked N-Acetylglucosamine induces vascular calcification in diabetes mellitus. *Circ. Res.* **114**, 1094–1102 (2014).

35. Miguez, J. S. G. *et al.* O-Glycosylation with O-linked β-N-acetylglucosamine increases vascular contraction: Possible modulatory role on Interleukin-10 signaling pathway. *Life Sci.* **209**, 78–84 (2018).

36. Yao, D. *et al.* O-linked β-N-acetylglucosamine modification of A20 enhances the inhibition of NF-κB (nuclear factor-κB) activation and elicits vascular protection after acute endoluminal arterial injury. *Arterioscler. Thromb. Vasc. Biol.* **38**, 1309–1320 (2018).

37. Soulié, M. *et al.* O-GlcNAcase inhibition by Thiamet G opposes acute cardiac decompensation in rats with chronic heart failure. *Arch. Cardiovasc. Dis. Suppl.* **11**, 229 (2019).

38. Shen, Y. *et al.* Aging is associated with impaired activation of protein homeostasis-related pathways after cardiac arrest in mice. *J. Am. Heart Assoc.* **7**, 1–16 (2018).

39. Dubois-Deruy, E. *et al.* Interplay between troponin T phosphorylation and O-N-

acetylglucosaminylation in ischaemic heart failure. *Cardiovasc. Res.* **107**, 56–65 (2015).

40. Ding, N. *et al.* Thiamet-G-mediated inhibition of O-GlcNAcase sensitizes human leukemia cells to microtubule-stabilizing agent paclitaxel. *Biochem. Biophys. Res. Commun.* **453**, 392–397 (2014).

41. Olivier-Van Stichelen, S. *et al.* O-GlcNAcylation stabilizes β-catenin through direct competition with phosphorylation at threonine 41. *FASEB J.* **28**, 3325–3328 (2014).

42. Ishimura, E. *et al.* Augmented O-GlcNAcylation of AMP-activated kinase promotes the proliferation of LoVo cells, a colon cancer cell line. *Cancer Sci.* **108**, 2373–2382 (2017).

43. Yuzwa, S. A. *et al.* Pharmacological inhibition of O-GlcNAcase (OGA) prevents cognitive decline and amyloid plaque formation in bigenic tau/APP mutant mice. *Mol. Neurodegener.* **9**, 42 (2014).

44. Matsuyama, S. S. & Jarvik, L. F. Hypothesis: Microtubules, a key to Alzheimer disease. *Proc. Natl. Acad. Sci. U. S. A.* **86**, 8152–8156 (1989).

45. Cash, A. D. *et al.* Microtubule reduction in Alzheimer's disease and aging is independent of τ filament formation. *Am. J. Pathol.* **162**, 1623–1627 (2003).

46. Barbier, P. *et al.* Role of tau as a microtubule-associated protein: Structural and functional aspects. *Front. Aging Neurosci.* **10**, 1–14 (2019).

47. Weingarten, M. D., Lockwood, A. H., Hwo, S. Y. & Kirschner, M. W. A protein factor essential for microtubule assembly. *Proc. Natl. Acad. Sci. U. S. A.* **72**, 1858–1862 (1975).

48. Lindwall, G. & Cole, R. D. Phosphorylation affects the ability of tau protein to promote microtubule assembly. *J. Biol. Chem.* **259**, 5301–5305 (1984).

49. Kim, N., Chen, D., Zhou, X. Z. & Lee, T. H. Death-associated protein kinase 1 phosphorylation in neuronal cell death and neurodegenerative disease. *Int. J. Mol. Sci.* **20**, (2019).

50. Bourré, G. *et al.* Direct crosstalk between O-GlcNAcylation and phosphorylation of tau protein investigated by NMR spectroscopy. *Front. Endocrinol.* **9**, 1–13 (2018).

51. O'Donnell, N., Zachara, N. E., Hart, G. W. & Marth, J. D. Ogt-Dependent X-Chromosome-Linked Protein Glycosylation Is a Requisite Modification in Somatic Cell Function and Embryo Viability. *Mol. Cell. Biol.* **24**, 1680–1690 (2004).

52. Zhu, Y., Shan, X., Yuzwa, S. A. & Vocadlo, D. J. The emerging link between O-GlcNAc and Alzheimer disease. *J. Biol. Chem.* **289**, 34472–34481 (2014).

53. Di Domenico, F., Lanzillotta, C. & Tramutola, A. Therapeutic potential of rescuing protein O-GlcNAcylation in tau-related pathologies. *Expert Rev. Neurother.* **19**, 1–3 (2019).

54. Erin E. Congdon & Sigurdsson, E. M. Tau-targeting therapies for Alzheimer disease. *Nat. Rev. Neurol.* **14**, 399–415 (2018).

55. Zhu, Y., Shan, X., Yuzwa, S. A. & Vocadlo, D. J. The emerging link between O-GlcNAc and Alzheimer disease. *J. Biol. Chem.* **289**, 34472–34481 (2014).

56. Kim, C. *et al.* O-linked β-N-acetylglucosaminidase inhibitor attenuates β-amyloid plaque and rescues memory impairment. *Neurobiol. Aging* **34**, 275–285 (2013).

57. Hooper, C., Killick, R. & Lovestone, S. The GSK3 hypothesis of Alzheimer's disease. *J. Neurochem.* **104**, 1433–1439 (2008).

58. Del Tredici, K. & Braak, H. Sporadic Parkinson's disease: Development and distribution of α-synuclein pathology. *Neuropathol. Appl. Neurobiol.* **42**, 33–50 (2016).

59. Levine, P. M. *et al.* α-Synuclein O-GlcNAcylation alters aggregation and toxicity, revealing certain residues as potential inhibitors of Parkinson's disease. *Proc. Natl. Acad. Sci. U. S. A.* **116**, 1511–1519 (2019).

60. Macauley, M. S., Whitworth, G. E., Debowski, A. W., Chin, D. & Vocadlo, D. J. O-GlcNAcase uses substrate-assisted catalysis: Kinetic analysis and development of highly selective mechanism-inspired inhibitors. *J. Biol. Chem.* **280**, 25313–25322 (2005).

61. Yuzwa, S. A. *et al.* A potent mechanism-inspired O-GlcNAcase inhibitor that blocks phosphorylation of tau in vivo. *Nat. Chem. Biol.* **4**, 483–490 (2008).

62. Selnick, H. G. *et al.* Discovery of MK-8719, a Potent O-GlcNAcase Inhibitor as a Potential Treatment for Tauopathies. *J. Med. Chem.* (2019) doi:10.1021/acs.jmedchem.9b01090.

63. Chahboune, A., Decaffmeyer, M., Brasseur, R. & Joris, B. Membrane topology of the Escherichia coli AmpG permease required for recycling of cell wall anhydromuropeptides and AmpC β-lactamase induction. *Antimicrob. Agents Chemother.* **49**, 1145–1149 (2005).

64. Kong, K. F., Schneper, L. & Mathee, K. Beta-lactam antibiotics: From antibiosis to resistance and bacteriology. *Apmis* **118**, 1–36 (2010).

65. Uehara, T. *et al.* Recycling of the anhydro-N-acetylmuramic acid derived from cell wall murein involves a two-step conversion to N-acetylglucosamine-phosphate. *J. Bacteriol.* **187**, 3643–3649 (2005).

66. Bush, K. Past and Present Perspective on B-Lactamase Inhibitors. 1–20 (2018).

67. Zamorano, L. *et al.* AmpG inactivation restores susceptibility of pan-β-lactam-resistant Pseudomonas aeruginosa clinical strains. *Antimicrob. Agents Chemother.* **55**, 1990–1996 (2011).

68. Perley-Robertson, G. E. *et al.* A Fluorescent Transport Assay Enables Studying AmpG Permeases Involved in Peptidoglycan Recycling and Antibiotic Resistance. *ACS Chem. Biol.* **11**, 2626–2635 (2016).

69. Khan, H. A., Baig, F. K. & Mehboob, R. Nosocomial infections: Epidemiology, prevention, control and surveillance. *Asian Pac. J. Trop. Biomed.* **7**, 478–482 (2017).

70. Tooke, C. L. *et al.* β-Lactamases and β-Lactamase Inhibitors in the 21st Century. *J. Mol. Biol.* **431**, 3472–3500 (2019).

71. Deshpande, L. M., Jones, R. N., Fritsche, T. R. & Sader, H. S. Occurrence of plasmidic AmpC type β-lactamase-mediated resistance in Escherichia coli: report from the SENTRY Antimicrobial Surveillance Program (North America, 2004). *Int. J. Antimicrob. Agents* **28**, 578–581 (2006).

72. Stephen P. Hawser, Bouchillonb, S. K., Hobanb, D. J. & B, R. E. B. In vitro susceptibilities of aerobic and facultative anaerobic Gram-negative bacilli from patients with intra-abdominal infections worldwide from 2005–2007: results from the SMART study. *Int. J. Antimicrob. Agents* **34**, 585–588 (2009).

73. Manchanda, V. & Singh, N. P. Occurrence and detection of AmpC β-lactamases among Gram-negative clinical isolates using a modified tree-dimensional test at Guru Tegh Bahadur hospital, Delhi, India. *J. Antimicrob. Chemother.* **51**, 415–418 (2003).

74. Jacobs, C., Frère, J.-M. & Normark, S. Cytosolic Intermediates for Cell Wall Biosynthesis and Degradation Control Inducible. *Cell* **88**, 823–832 (1997).

75. Perley-Robertson, G. E. & Vocadlo, D. Development of tools and methods for studying glycan processing proteins in living systems. *ACS Chemical Biology* (2016).

76. Anhydro-muropeptides, C. W., Cheng, Q. & Park, J. T. Substrate Specificity of the AmpG Permease Required for Recycling of Peptidoglycan. **184**, 6434–6436 (2002).

77. Leroy, E., Bensel, N. & Reymond, J. L. A low background high-throughput screening (HTS) fluorescence assay for lipases and esterases using acyloxymethylethers of umbelliferone. *Bioorganic Med. Chem. Lett.* **13**, 2105–2108 (2003).

78. Paulsen H, Himpkamp P, P. T. Bausteine von Oligosacchariden, LXIX. Synthese von 1,6-Anhydromuramylpeptiden. *Liebigs Ann. Chem.* 664–674 (1986) doi:10.1002/jlac.198619860408.

79. Galle Malik, Anglique Ferry, Xavier Guinchard, Thierry Cresteil, A. & Crich, D. NO Bond as a Glycosidic-Bond Surrogate: Synthetic Studies Toward Polyhydroxylated N-Alkoxypiperidines. *Chem. Eur. Journal* **19**, 2168–2179 (2012).

80. Cunha, A. C., Pereira, L. O. R., De Souza, M. C. B. V. & Ferreira, V. F. Use of protecting groups in carbohydrate chemistry: An advanced organic synthesis experiment. *J. Chem. Educ.* **76**, 79–80 (1999).

81. Dang, C. H., Nguyen, C. H., Nguyen, T. D. & Im, C. Synthesis and characterization of N-acyl-tetra-O-acyl glucosamine derivatives. *RSC Adv.* **4**, 6239–6245 (2014).

82. Martinac, B. Rohde, P. Cranfield, C. Nomura, T. *In Bacterial Cell Surfaces*. (Humana Press, 2013).

83. Harris, J. L. *et al.* Rapid and general profiling of protease specificity by using combinatorial fluorogenic substrate libraries. *Proc. Natl. Acad. Sci. U. S. A.* **97**, 7754–7759 (2000).

84. Sergio C. Chai and Qi-Zhuang Ye. A cell-based assay that targets methionine aminopeptidase in a physiologically relevant environment. *Bioorg. Med. Chem. Lett.* **20**, 2129–2132 (2010).

85. Ze-Qiang Ma, Sheng-Xue Xie, Qing-Qing Huang, F.-J. N. & Ye, T. D. H. and Q.-Z. Structural analysis of inhibition of E. coli methionine aminopeptidase: implication of loop adaptability in selective inhibition of bacterial enzymes. *BMC Struct. Biol.* **7**, (2007).

86. Lopez-Campistrous, A. *et al.* Localization, annotation and comparison of the Escherichia coli K-12 proteome under two states of growth. *Mol. Cell. Proteomics* **4**, 1205–1209 (2005).

87. Ben-Bassat, A., Bauer, K., Chang, S. Y., Myambo, K. & Boosman, A. Processing of the initiation methionine from proteins: Properties of the Escherichia coli methionine aminopeptidase and its gene structure. *J. Bacteriol.* **169**, 751–757 (1987).

88. Kadner, R. J. Transport systems for L methionine in Escherichia coli. *J. Bacteriol.* **117**, 232–241 (1974).

89. Piperno, J. R. & Oxender, D. L. Amino acid transport systems in Escherichia coli K-12. *J. Biol. Chem.* **243**, 5914–5920 (1968).

90. Khidekel, N., Ficarro, S. B., Peters, E. C. & Hsieh-Wilson, L. C. Exploring the O-

GlcNAc proteome: Direct identification of O-GlcNAc-modified from the brain. *Proc. Natl. Acad. Sci. U. S. A.* **101**, 13132–13137 (2004).

91. Whelan, S. A. & Hart, G. W. Proteomic Approaches to Analyze the Dynamic Relationships between Nucleocytoplasmic Protein Glycosylation and Phosphorylation. *Circ. Res.* **93**, 1047–1058 (2003).

92. Zhang, Z. *et al.* O-GlcNAc homeostasis contributes to cell fate decisions during hematopoiesis. *J. Biol. Chem.* **294**, 1363–1379 (2019).

93. Mishra, S., Ande, S. R. & Salter, N. W. O-GlcNAc modification: Why so intimately associated with phosphorylation? *Cell Commun. Signal.* **9**, 2–5 (2011).

94. Zhou, L. T. *et al.* Disruption of O-GlcNAc homeostasis during mammalian oocyte meiotic maturation impacts fertilization. *Mol. Reprod. Dev.* **86**, 543–557 (2019).

95. Levine, P. M. *et al.* α-Synuclein O-GlcNAcylation alters aggregation and toxicity, revealing certain residues as potential inhibitors of Parkinson's disease. *Proc. Natl. Acad. Sci. U. S. A.* **116**, 1511–1519 (2019).

96. Spillantini, M. G. & Goedert, M. Tau pathology and neurodegeneration. *Lancet Neurol.* **12**, 609–622 (2013).

97. Grima, J. C. *et al.* Mutant Huntingtin Disrupts the Nuclear Pore Complex. *Neuron* **94**, 93-107.e6 (2017).

98. Volbracht, C., Rostgaard, N. & Jul, P. Chronic O-B-N-Acetylglucosaminylase Inhibition With Thiamet-G Prevents Tau Pathology and Hyperactivity in Rtg4510 Mice. *Alzheimer's Dement.* **10**, P923 (2014).

99. McGreal, S. R. *et al.* Modulation of O-GlcNAc levels in the liver impacts acetaminophen-induced liver injury by affecting protein adduct formation and glutathione synthesis. *Toxicol. Sci.* **162**, 599–610 (2018).

100. Andrés-Bergós, J. *et al.* The increase in O-linked N-acetylglucosamine protein modification stimulates chondrogenic differentiation both in vitro and in vivo. *J. Biol. Chem.* **287**, 33615–33628 (2012).

101. Pinho, T. S., Correia, S. C., Perry, G., Ambrósio, A. F. & Moreira, P. I. Diminished O-GlcNAcylation in Alzheimer's disease is strongly correlated with mitochondrial anomalies. *Biochim. Biophys. Acta - Mol. Basis Dis.* **1865**, 2048–2059 (2019).

102. He, Y., Ma, X., Li, D. & Hao, J. Thiamet G mediates neuroprotection in experimental stroke by modulating microglia/macrophage polarization and inhibiting NF-κB p65 signaling. *J. Cereb. Blood Flow Metab.* **37**, 2938–2951 (2017).

103. Wu, B., Yang, X. & Yan, M. Synthesis and Structure-Activity Relationship Study of

Antimicrobial Auranofin against ESKAPE Pathogens. *J. Med. Chem.* **62**, 7751–7768 (2019).

104. Barrett, G. C. and A. R. K. Trifluoroacetic Acid as a Cyclisation Reagent for the Synthesis of Thiazol5(4H)-ones and 2-Thiazolines. *J. Chem. Soc. C* 1117–1119 (1969).

Appendix - NMR Spectra

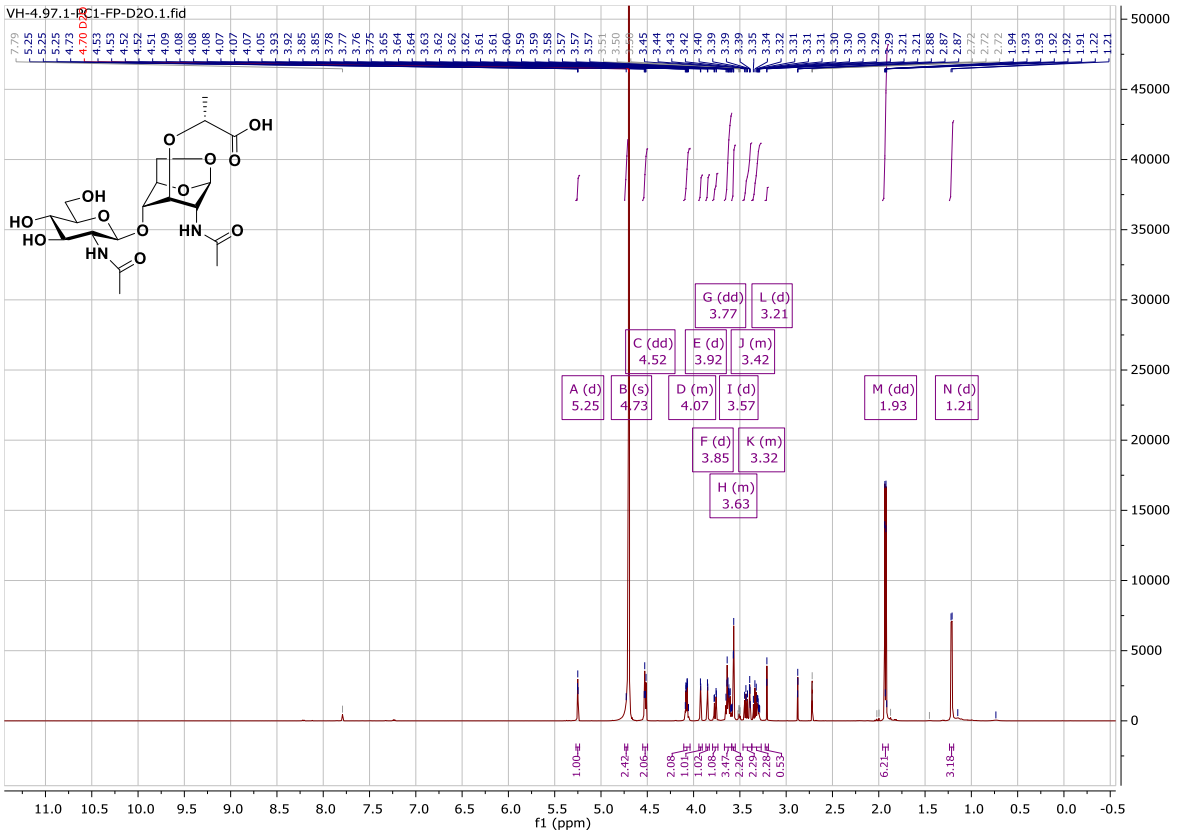
VH-4.97.1-PC1-FP-D2O.1.fid
G (dd) 3.77
L (d) 3.21
C (dd) 4.52
E (d) 3.92
J (m) 3.42
A (d) 5.25
B (s) 4.73
D (m) 4.07
I (d) 3.57
M (dd) 1.93
N (d) 1.21
F (d) 3.85
K (m) 3.32
H (m) 3.63
f1 (ppm)

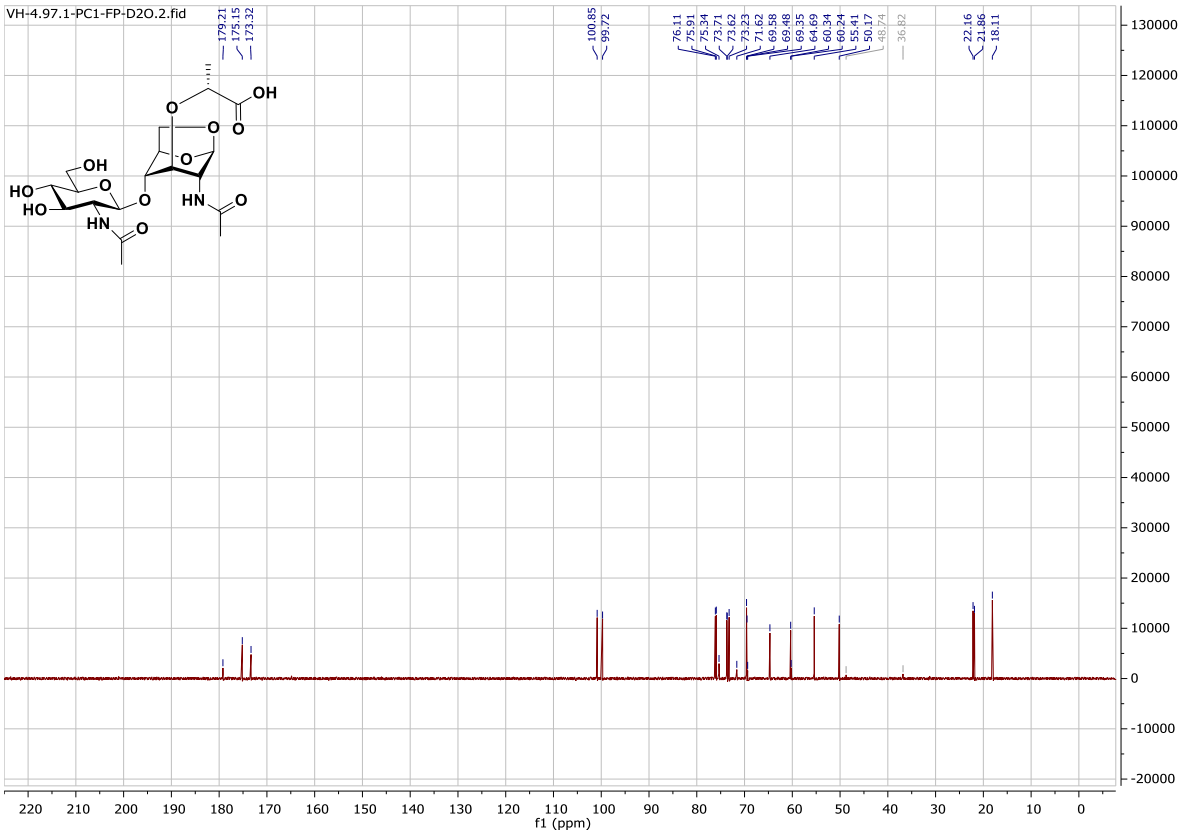
VH-4.97.1-PC1-FP-D2O.2.fid
f1 (ppm)

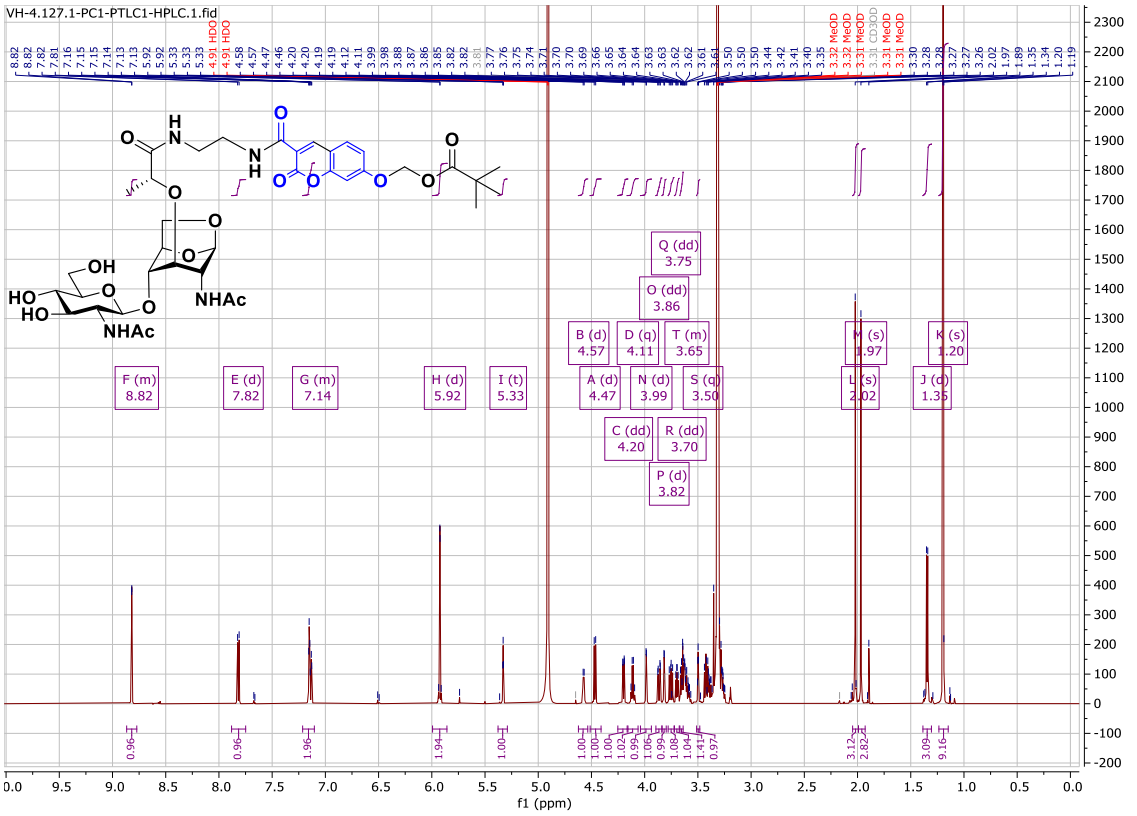
VH-4.127.1-PC1-PTLC1-HPLC.1.fid
Q (dd) 3.75
O (dd) 3.86
B (d) 4.57
D (q) 4.11
T (m) 3.65
M (s) 1.97
K (s) 1.20
F (m) 8.82
E (d) 7.82
G (m) 7.14
H (d) 5.92
I (t) 5.33
A (d) 4.47
N (d) 3.99
S (q) 3.50
L (s) 2.02
J (d) 1.35
C (dd) 4.20
R (dd) 3.70
P (d) 3.82
f1 (ppm)

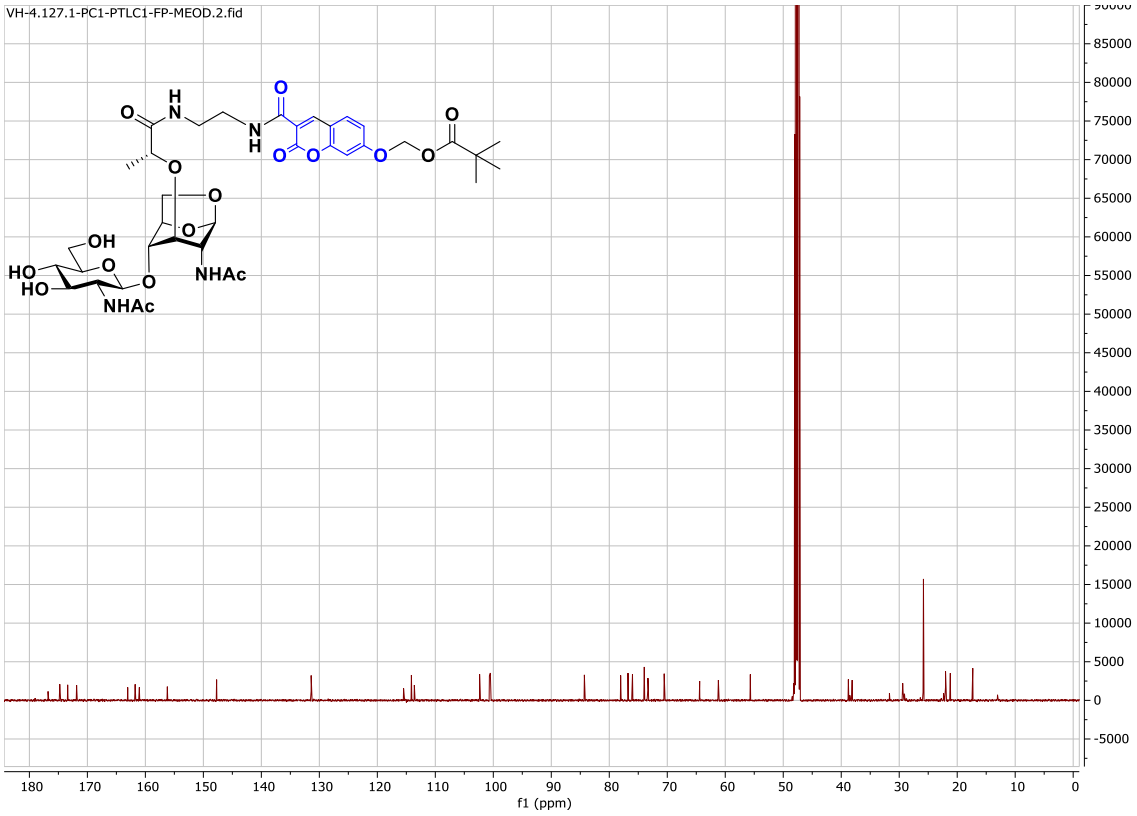
VH-4.127.1-PC1-PTLC1-FP-MEOD.2.fid
f1 (ppm)

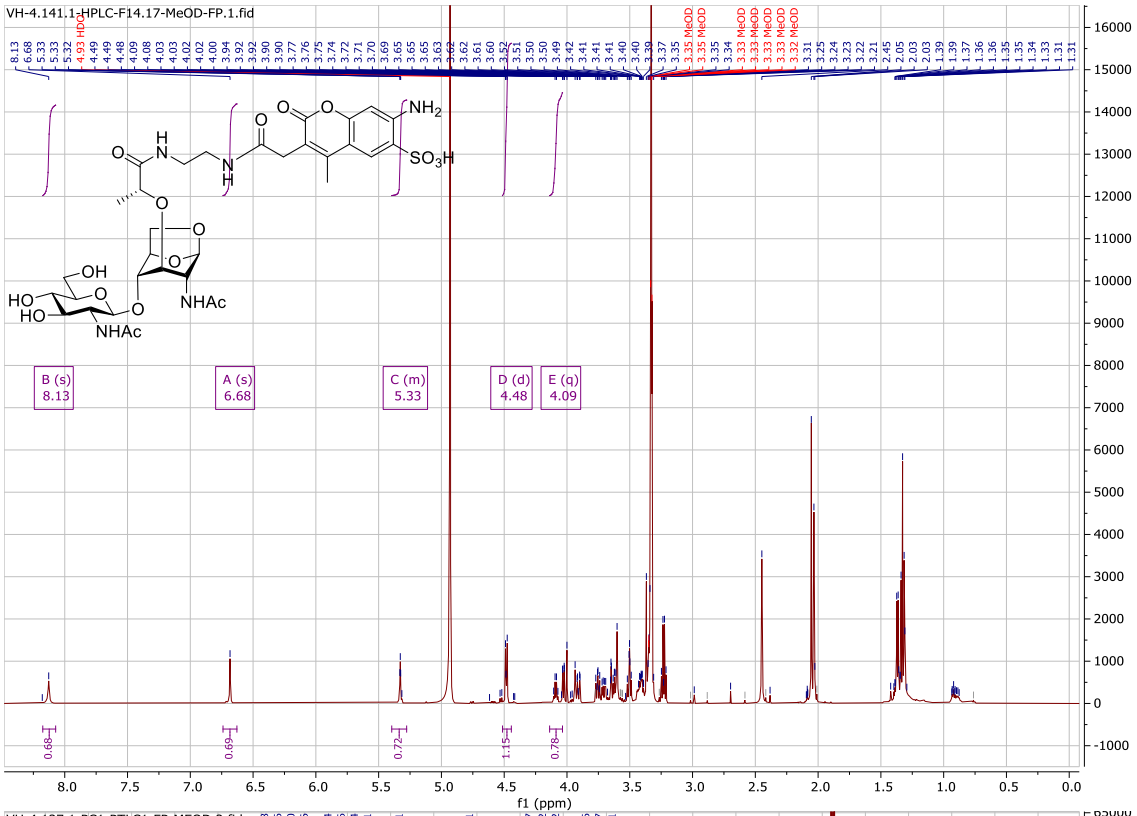
VH-4.141.1-HPLC-F14.17-MeOD-FP.1.fid
B (s)
8.13
A (s)
6.68
C (m)
5.33
D (d)
4.48
E (q)
4.09
0.68
0.69
0.72
1.15
0.78
f1 (ppm)

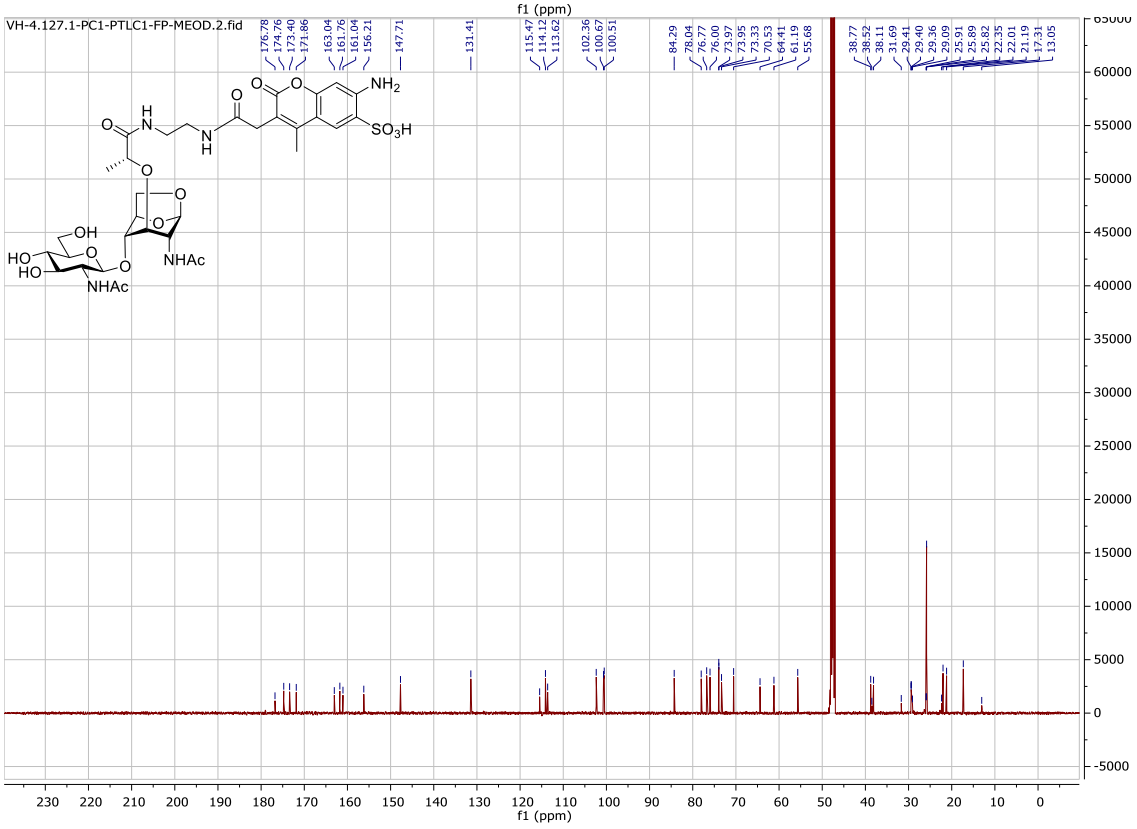
VH-4.127.1-PC1-PTLC1-FP-MEOD.2.fid
f1 (ppm)

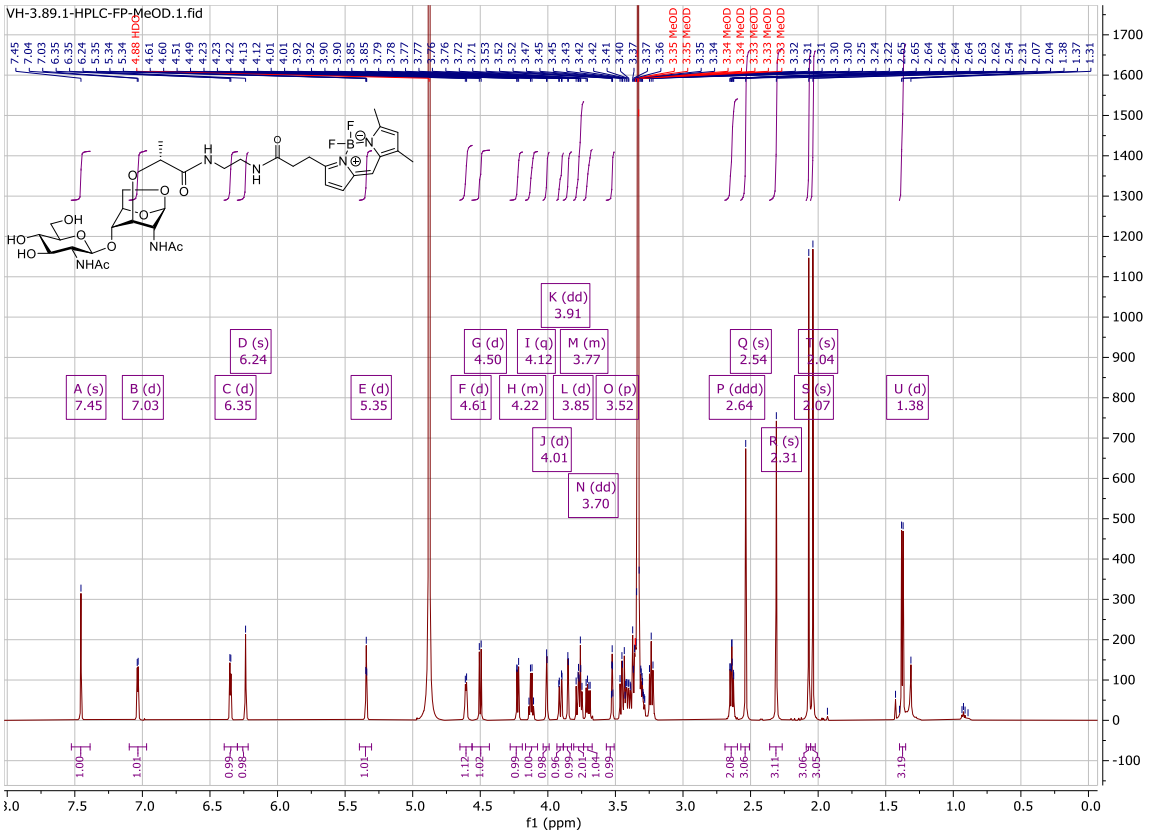
VH-3.89.1-HPLC-FP-MeOD.1.fid
A (s) 7.45
B (d) 7.03
C (d) 6.35
D (s) 6.24
E (d) 5.35
F (d) 4.61
G (d) 4.50
H (m) 4.22
I (q) 4.12
J (d) 4.01
K (dd) 3.91
L (d) 3.85
M (m) 3.77
N (dd) 3.70
O (p) 3.52
P (ddd) 2.64
Q (s) 2.54
R (s) 2.31
S (s) 2.07
T (s) 2.04
U (d) 1.38
f1 (ppm)

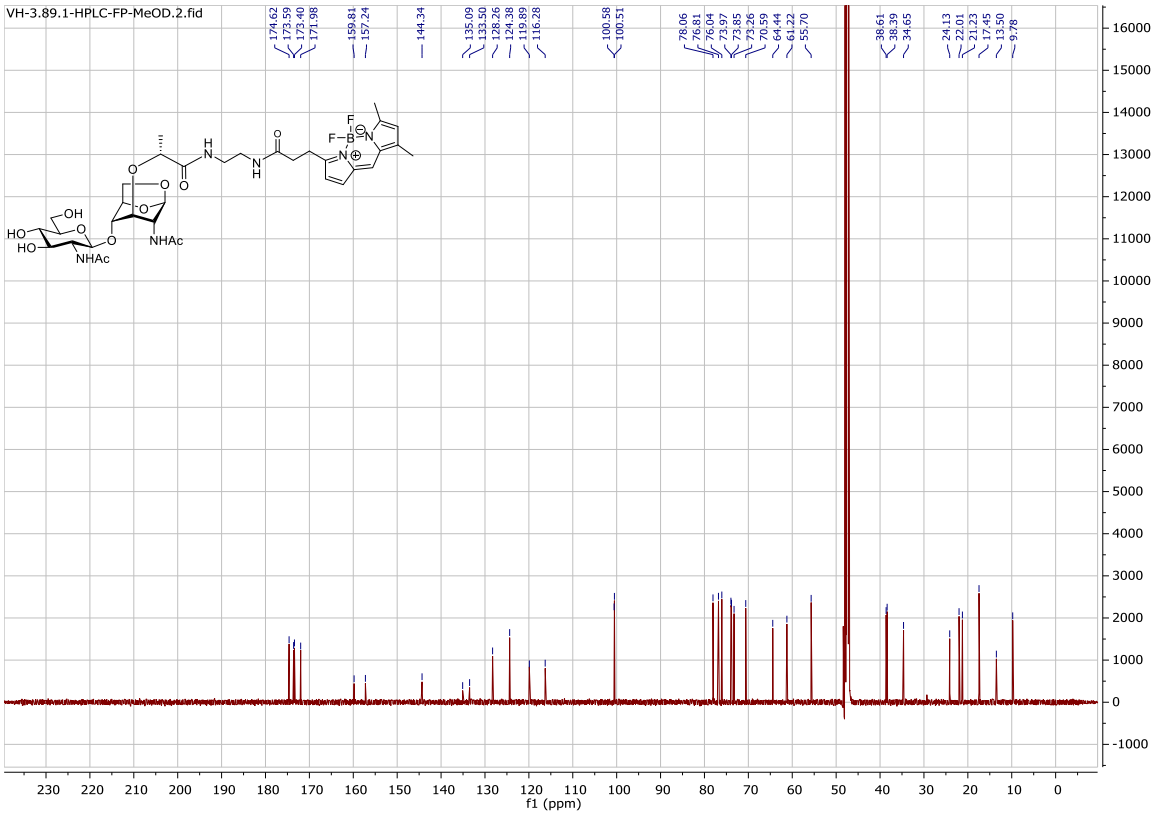
VH-3.89.1-HPLC-FP-MeOD.2.fid
f1 (ppm)

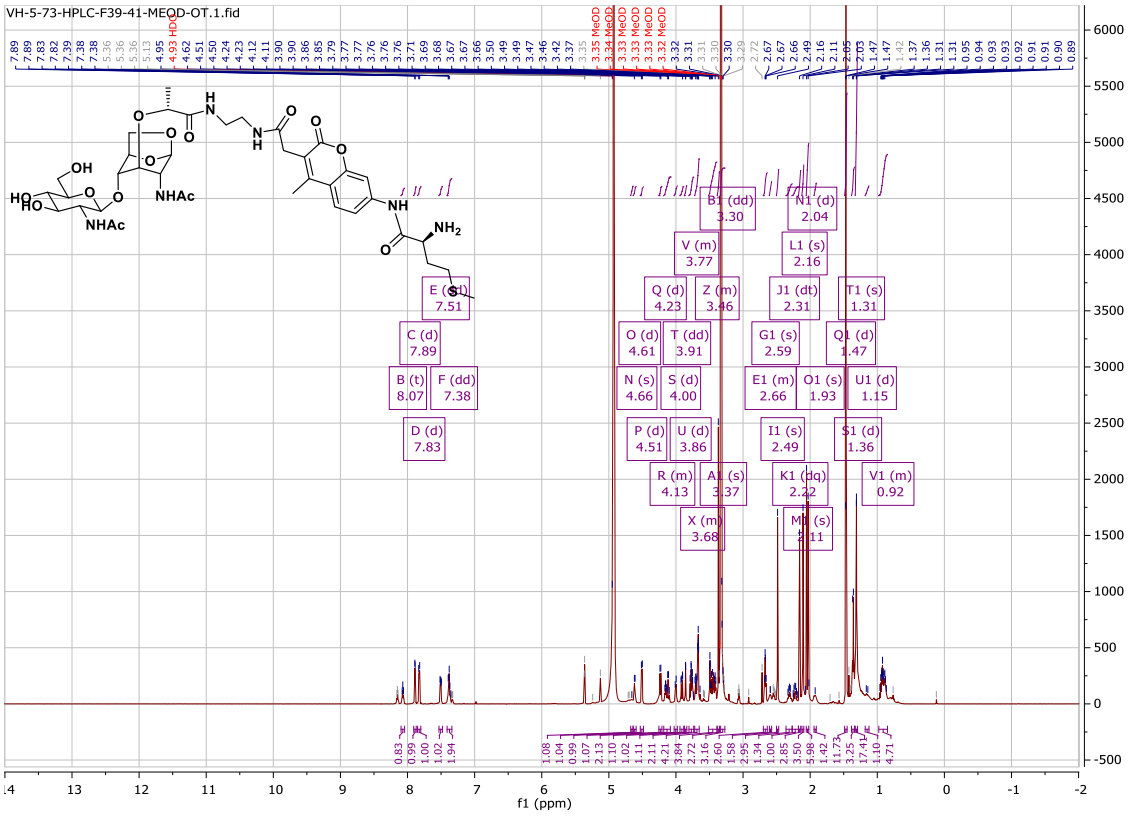
VH-5-73-HPLC-F39-41-MEOD-OT.1.fid
f1 (ppm)

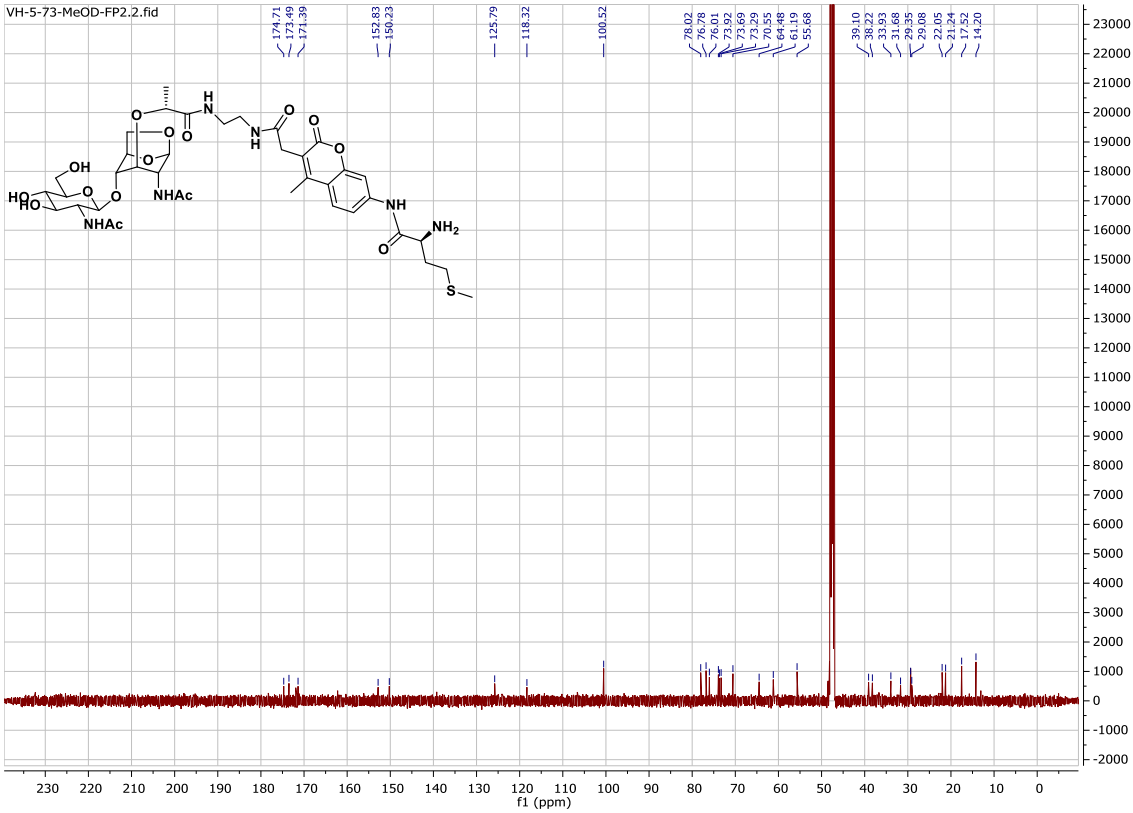
VH-5-73-MeOD-FP2.2.fid
f1 (ppm)

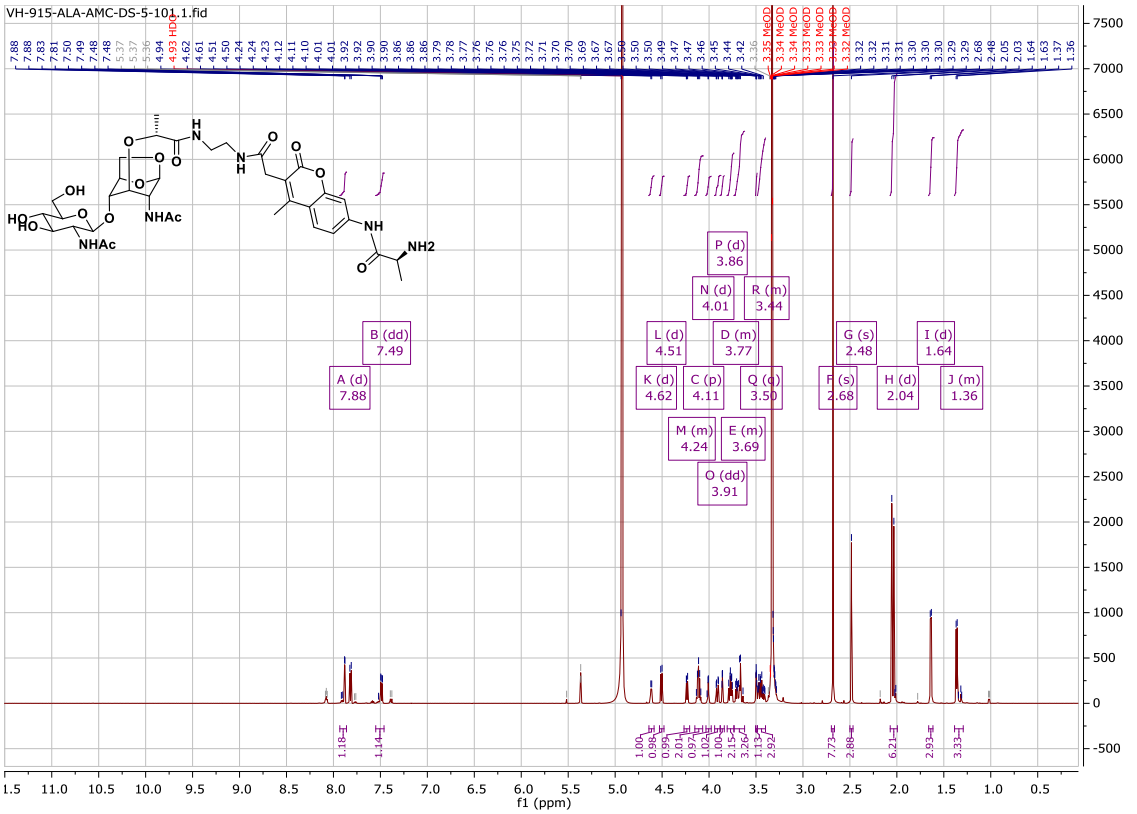
VH-915-ALA-AMC-DS-5-101.1.fid
P (d) 3.86
N (d) 4.01
R (m) 3.44
B (dd) 7.49
L (d) 4.51
D (m) 3.77
G (s) 2.48
I (d) 1.64
A (d) 7.88
K (d) 4.62
C (p) 4.11
Q (d) 3.50
F (s) 2.68
H (d) 2.04
J (m) 1.36
M (m) 4.24
E (m) 3.69
O (dd) 3.91
f1 (ppm)

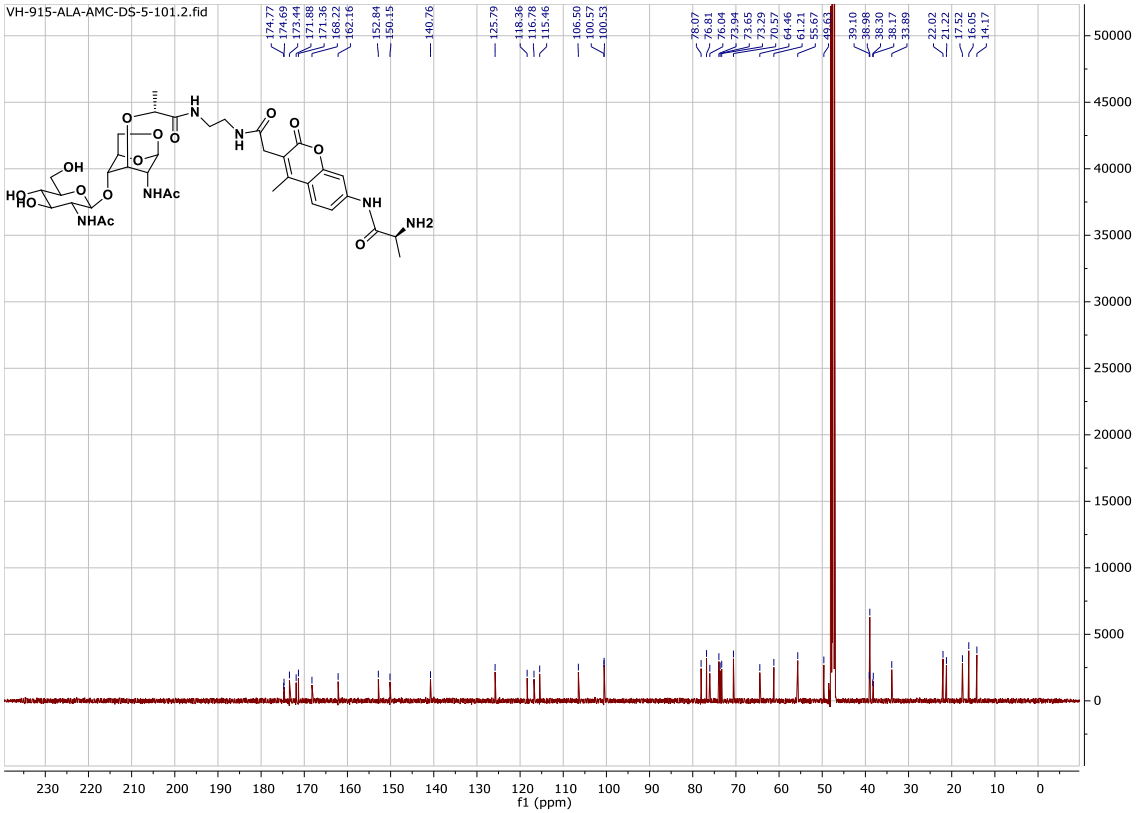
VH-915-ALA-AMC-DS-5-101.2.fid
f1 (ppm)

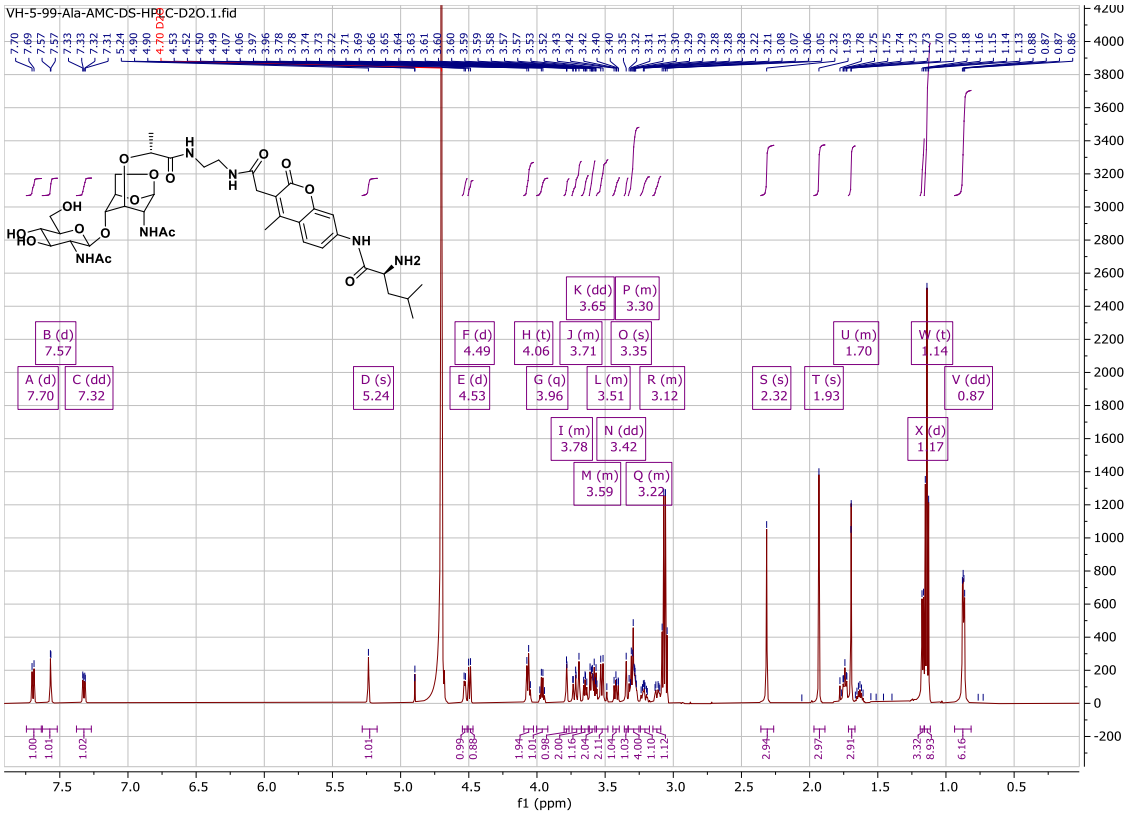
VH-5-99-Ala-AMC-DS-HPLC-D2O.1.fid
A (d) 7.70
B (d) 7.57
C (dd) 7.32
D (s) 5.24
E (d) 4.53
F (d) 4.49
G (q) 3.96
H (t) 4.06
I (m) 3.78
J (m) 3.71
K (dd) 3.65
L (m) 3.51
M (m) 3.59
N (dd) 3.42
O (s) 3.35
P (m) 3.30
Q (m) 3.22
R (m) 3.12
S (s) 2.32
T (s) 1.93
U (m) 1.70
V (dd) 0.87
W (t) 1.14
X (d) 1.17
f1 (ppm)

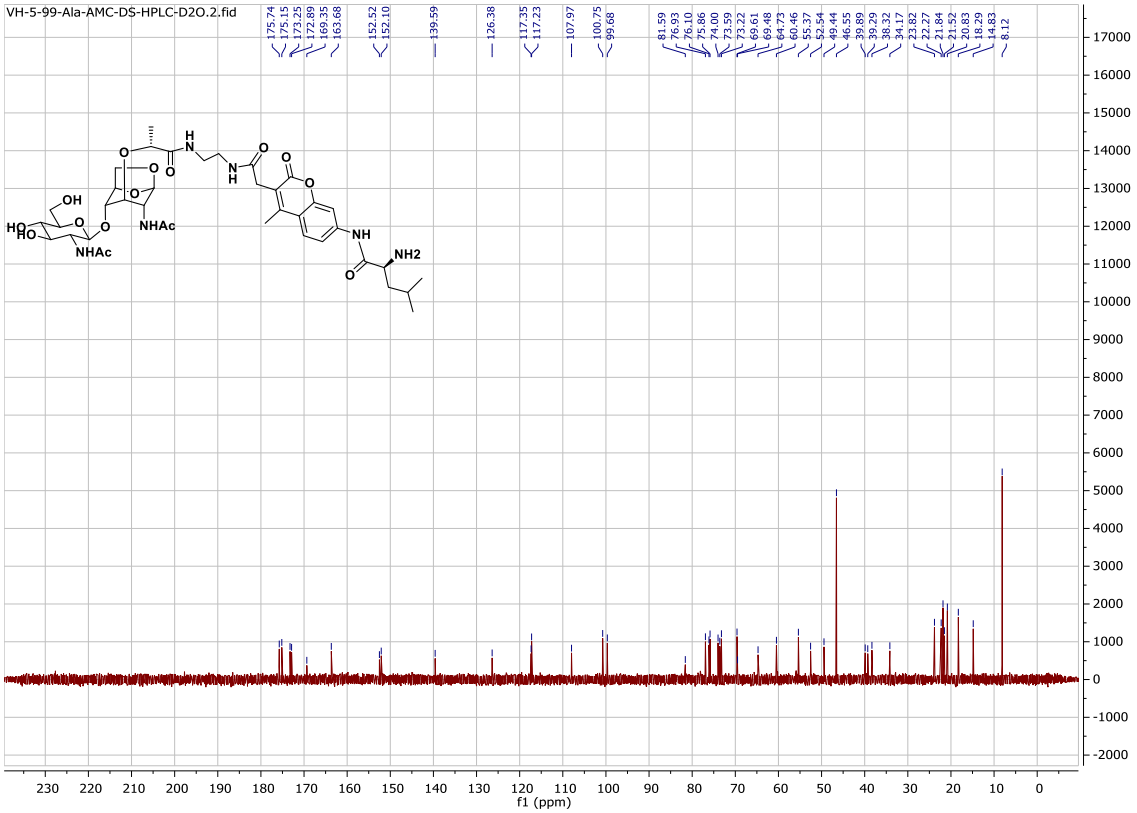
VH-5-99-Ala-AMC-DS-HPLC-D2O.2.fid
f1 (ppm)

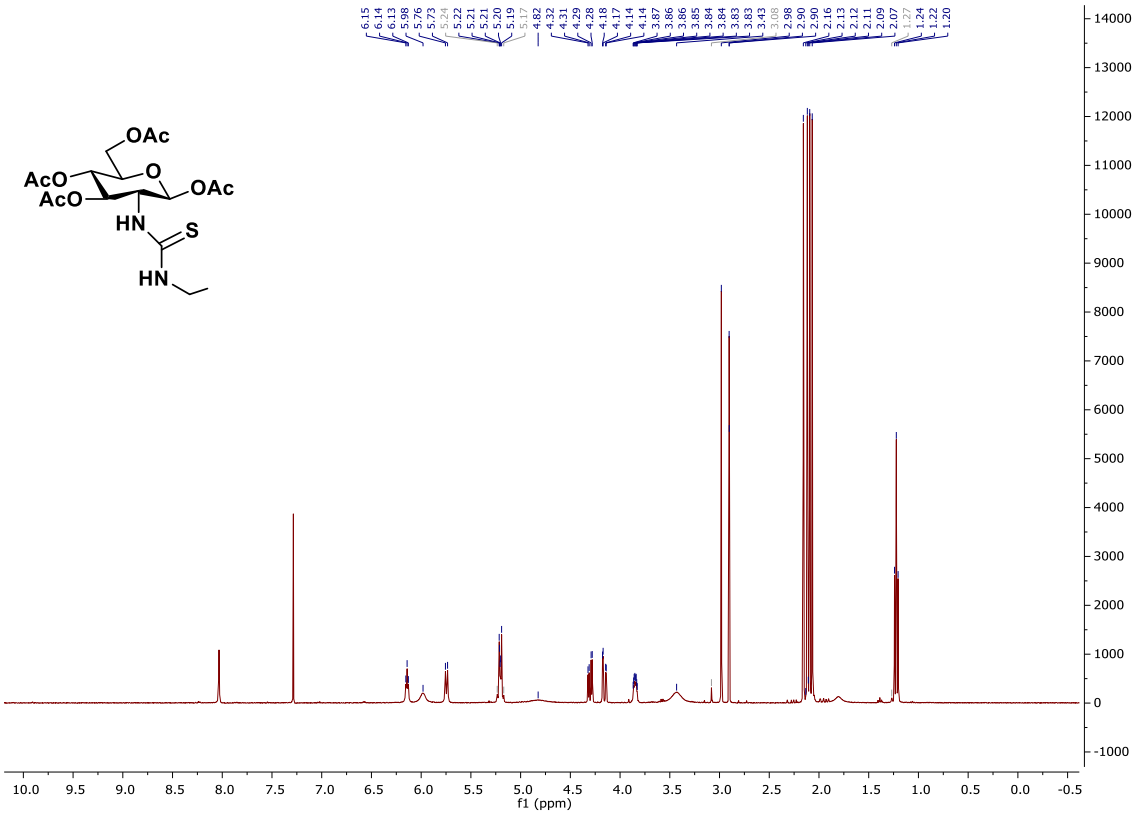
OAc
AcO
O
OAc
AcO
HN
S
HN
f1 (ppm)

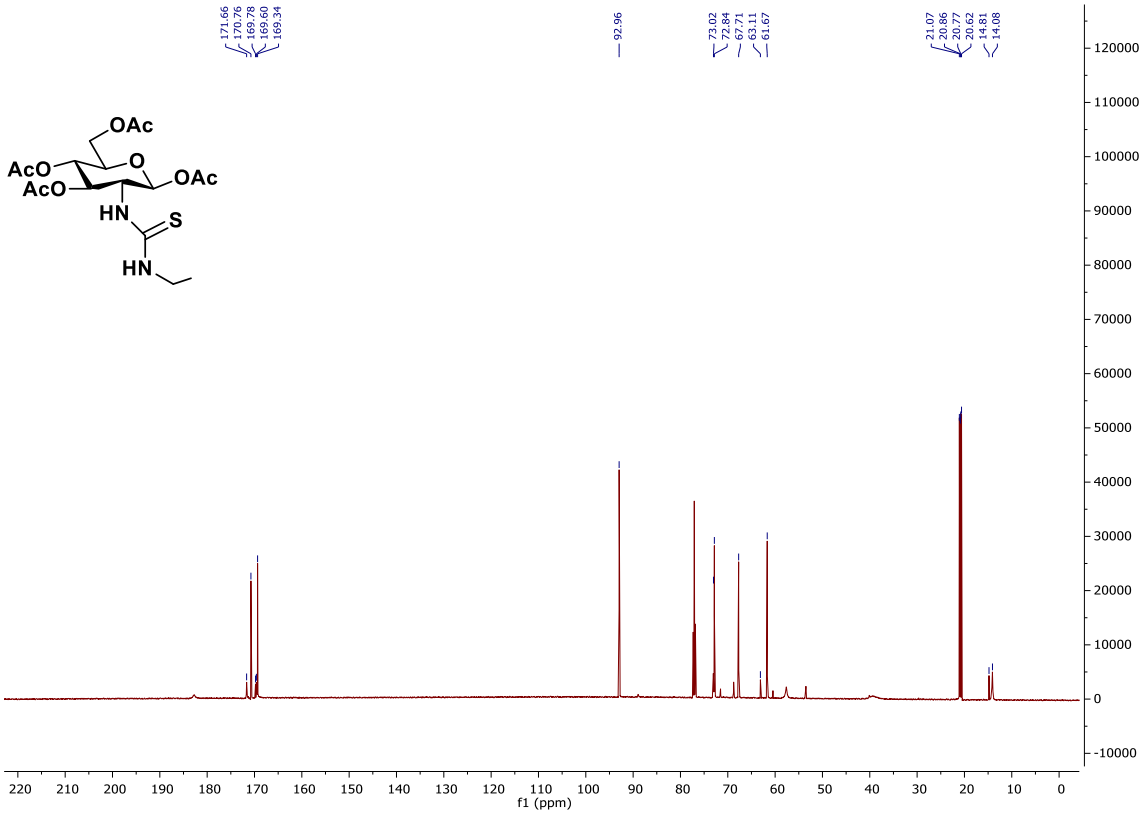
OAc
AcO
O
OAc
AcO
HN
S
HN
f1 (ppm)

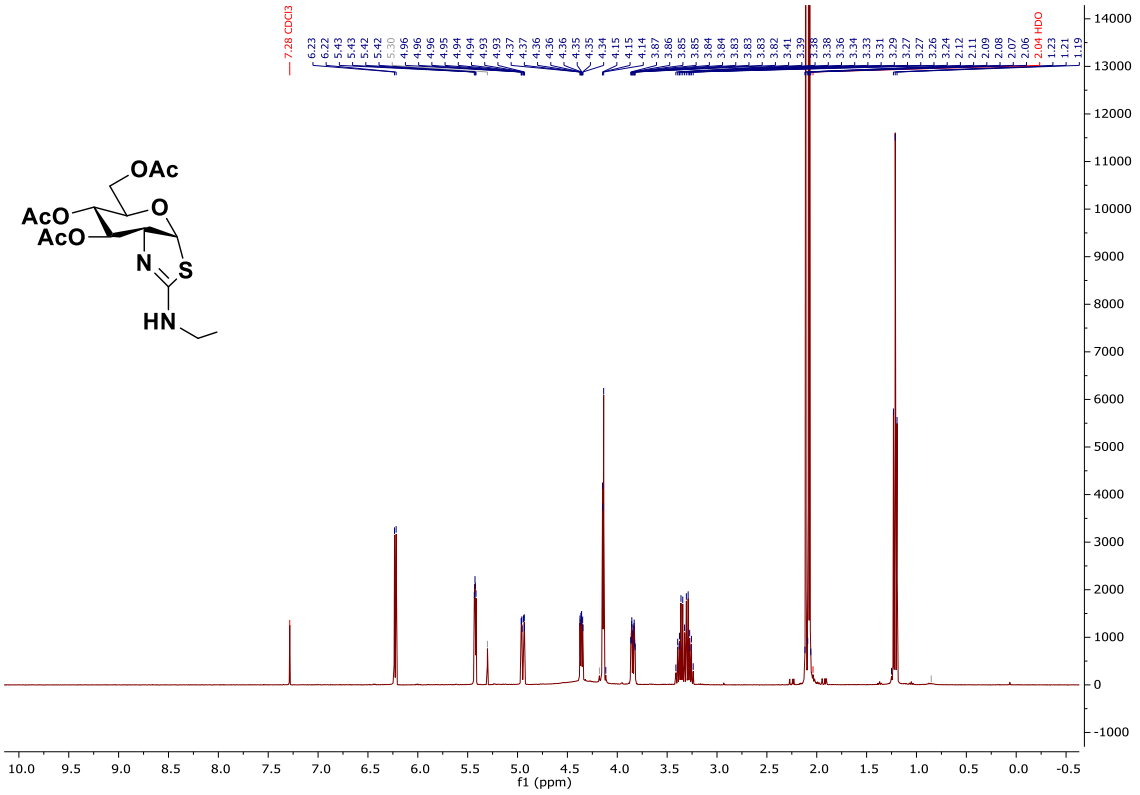
OAc
AcO
AcO
O
N
S
HN
7.28 CDCl3
2.04 HDO
f1 (ppm)

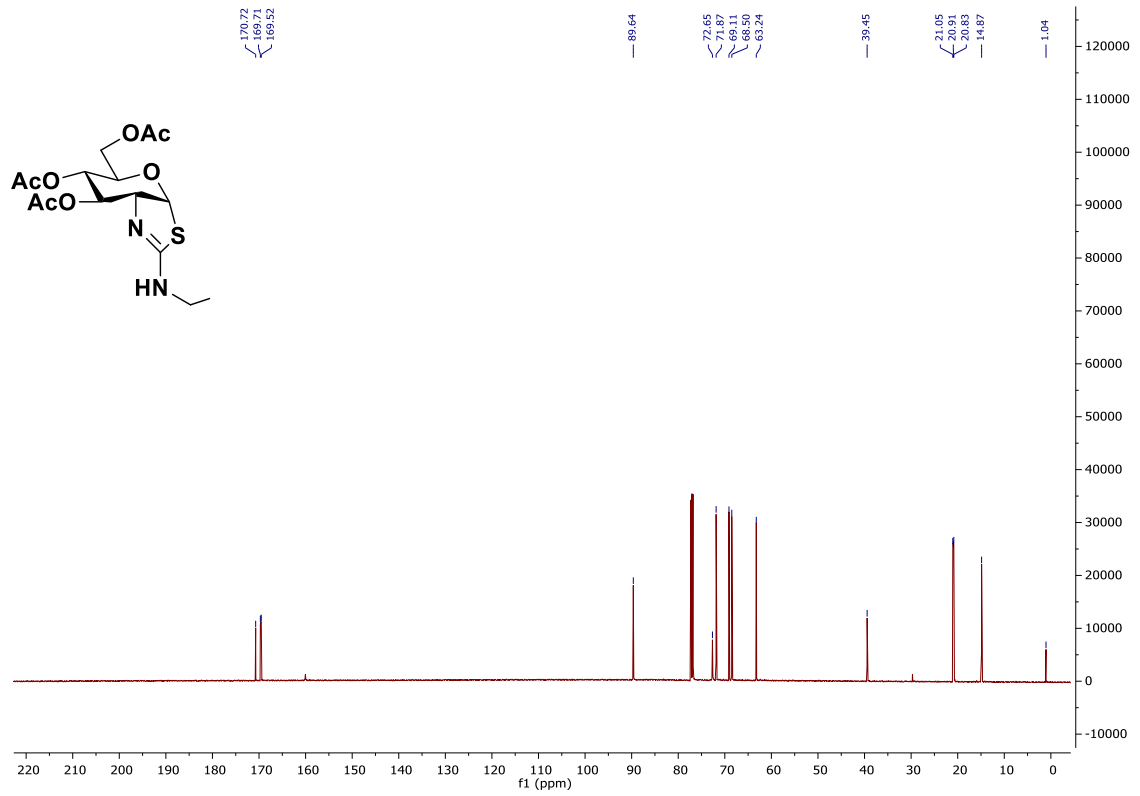
OAc
AcO
AcO
O
N
S
HN
170.72
169.71
169.52
89.64
72.65
71.87
69.11
68.50
63.24
39.45
21.05
20.91
20.83
14.87
1.04
f1 (ppm)

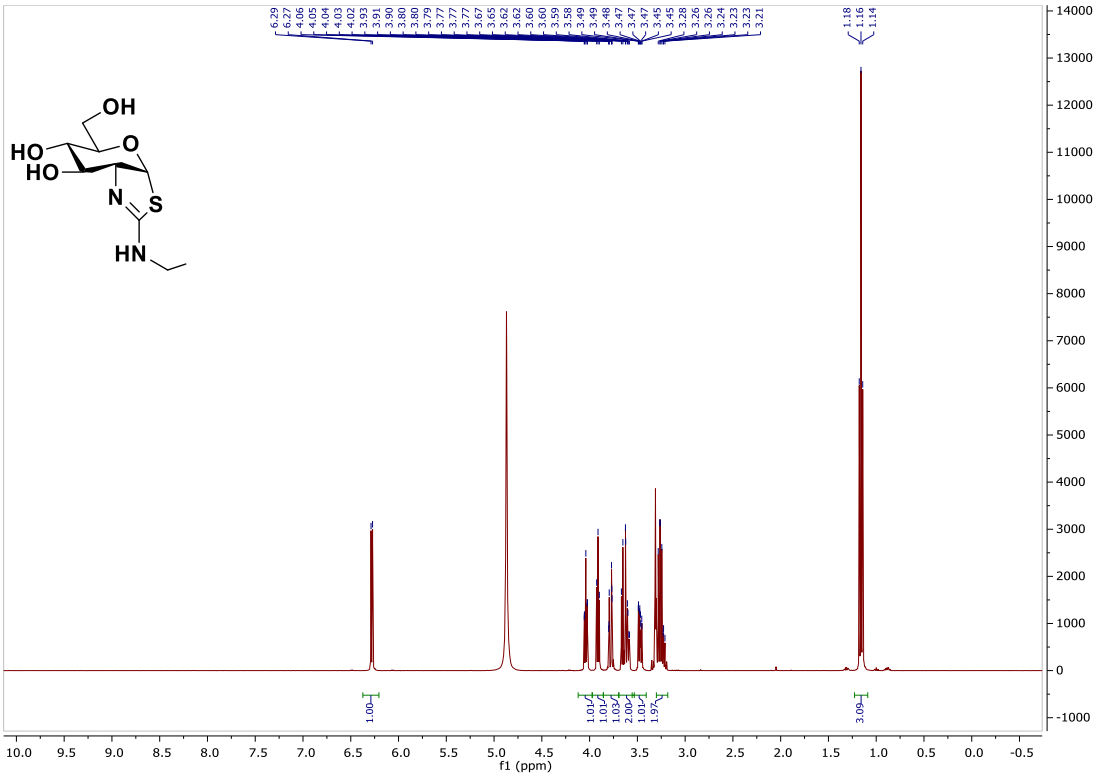
OH
HO
HO
O
N
S
HN
f1 (ppm)

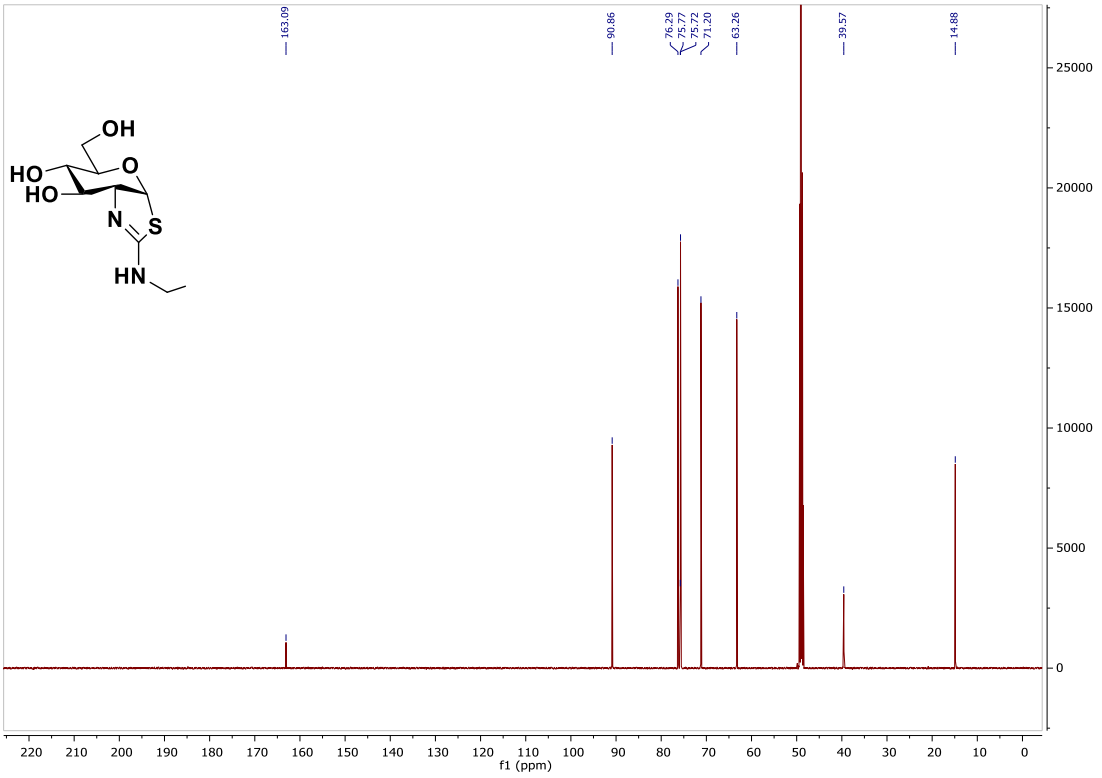
OH
HO
HO
O
N
S
HN
163.09
90.86
76.29
75.77
75.72
71.20
63.26
39.57
14.88
f1 (ppm)